AD-A043 013   NATIONAL AERONAUTICAL ESTABLISHMENT OTTAWA (ONTARIO)   F/G 20/4
ANALYSIS OF WALL INTERFERENCE EFFECTS ON ONERA CALIBRATION MODE--ETC(U)
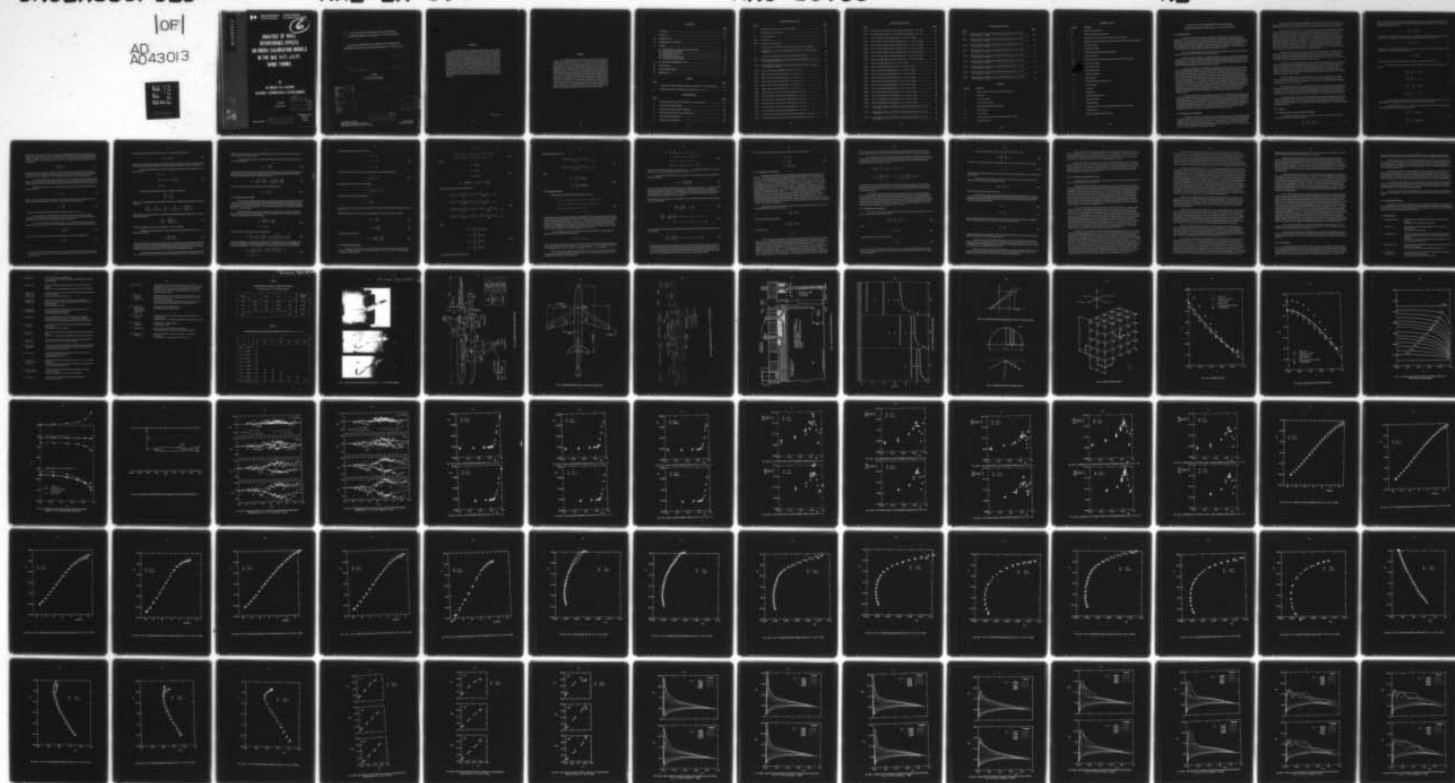MAR 77   M MOKRY, R D GALWAY

UNCLASSIFIED   NAE-LR-594   NRC-15953   NL

National Research Council Canada

Conseil national de recherches Canada

⑥

ANALYSIS OF WALL INTERFERENCE EFFECTS ON ONERA CALIBRATION MODELS IN THE NAE 5-FT. x 5-FT. WIND TUNNEL
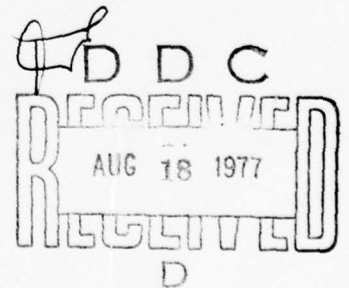
BY

M. MOKRY, R.D. GALWAY

NATIONAL AERONAUTICAL ESTABLISHMENT

OTTAWA

MARCH 1977

NRC NO. 15953

AERONAUTICAL REPORT

LR-594

ANALYSIS OF WALL INTERFERENCE EFFECTS ON ONERA

CALIBRATION MODELS IN THE NAE 5-FT. × 5-FT. WIND TUNNEL

(ANALYSE DES CORRECTIONS DE PAROIS POUR LES MAQUETTES

D'ÉTALONNAGE ONERA DANS LA SOUFFLERIE DE 5 PI × 5 PI DE L'E.A.N.)

Mars 77

NAE-LR-594

83 p.

by/par

M. Mokry   R.D. Galway

NRC

15953

DDC
RECEIVED
AUG 18 1977
D

L.H. Ohman, Head/Chef
High Speed Aerodynamics Laboratory/
Laboratoire d'aérodynamique à hautes vitesses

240 300

F.R. Thurston
Director/Directeur

SUMMARY

The measurements on three geometrically similar aircraft models by ONERA are used to analyse lift interference effects in the solid and perforated wall test sections of the NAE 5-ft. × 5-ft. test facility. The prediction of the angle of attack correction for both test sections is based on the representation of the model by lifting lines and the solution of the subsonic wall interference problem by the finite difference method. The value of the porosity factor ascribed to the test section with perforated walls is checked by comparing the measured wall pressure distributions with the theoretical ones, predicted by the present method. The lift interference effects on models M1 and M3, having wing span to wind tunnel width ratios of 0.188 and 0.311 respectively, were found to be within the limits of experimental errors. For the M5 model, having a wing span to wind tunnel width ratio of 0.644, the solid and perforated test section measurements, corrected using a uniform angle of attack correction, show good agreement up to lift coefficients of about 0.5.

(français verso)

RÉSUMÉ

Les mesures effectuées sur trois maquettes d'avions homothétiques ONERA sont utilisées pour l'analyse de la correction de portance dans les veines à parois pleines et perforées de la soufflerie de 5 pi X 5 pi de l'E.A.N. Le calcul de la correction d'incidence pour les deux veines est fondé sur la représentation de la maquette par des segments portants et sur la solution du problème de correction des parois en veine subsonique par la méthode des différences finies. On vérifie la valeur du paramètre de porosité attribué à la veine à parois perforées en comparant les distributions mesurées de la pression sur les parois aux distributions théoriques, que la présente méthode permet de calculer. La correction de portance pour les maquettes M1 et M3, dont les rapports entre envergure d'aile et largeur de la soufflerie sont respectivement de 0.188 et 0.311, était à l'intérieur des marges d'erreur expérimentales. Pour la maquette M5, dont le rapport entre envergure d'aile et largeur de la soufflerie est de 0.644, les mesures effectuées pour les veines pleines et perforées, auxquelles on a appliqué une correction d'incidence uniforme, ont assez bien concordé jusqu'à des coefficients de portance d'environ 0.5.

CONTENTS

TABLES

ILLUSTRATIONS

ILLUSTRATIONS (Cont'd)

ILLUSTRATIONS (Cont'd)

ILLUSTRATIONS (Cont'd)

SYMBOLS

Symbol	Definition
A	cross-sectional area of the wind tunnel, Equation (11)
b	model span
B	wind tunnel width
c	local chord of the wing
$\bar{c}$	aerodynamic mean chord of the wing
C_D	drag coefficient
C_L	lift coefficient
C_M	pitching moment coefficient (about aerodynamic centre)
C_p	pressure coefficient

Symbol	Definition
C_p^*	critical pressure coefficient
D	maximum diameter of the fuselage
f	disturbance velocity potential of flow past a model in free air
g	disturbance velocity potential due to wall constraint (wall interference potential)
H	wind tunnel height
M	stream Mach number
n	normal, pointing outward from the flow field
P	porosity parameter
Re	Reynolds number, based on the aerodynamic mean chord of the wing
$S(x, y, z)$	surface of the model
S	model reference area
	factor, Equation (4)
x, y, z	Cartesian co-ordinates
α	angle of attack
β	Prandtl-Glauert factor, Equation (41)
γ	vortex strength
Γ	circulation
δ_o	upwash factor
δ_1	streamline curvature factor
δ_p	wall pressure factor
τ	sweepback angle
ϕ	disturbance velocity potential of the wind tunnel flow past a model
ω	relaxation factor
$\sim$	denotes compressible flow quantities

ANALYSIS OF WALL INTERFERENCE EFFECTS ON ONERA
CALIBRATION MODELS IN THE NAE 5-FT. × 5-FT. WIND TUNNEL

1.0 INTRODUCTION

The experimental part of the present investigation was performed in the NAE 5-ft. × 5-ft. wind tunnel in the winter of 1974-75 as a part of the international program, initiated by ONERA, Reference 1. The main purpose was to compare test results on a series of geometrically similar models from various European and North American wind tunnels in an effort to improve the existing knowledge of scale effect and wind tunnel interference. The second objective of NAE was to assist Dilworth, Secord, Meagher & Associates (DSMA) in fulfilling the contractual commitment to provide training for one of their clients in testing in a high performance blowdown wind tunnel.

Reviews of results and analyses of the test data from wind tunnel facilities where the ONERA models were tested prior to NAE can be found in References 1-7.

Of the four aircraft models manufactured by ONERA only three, the M1, M3, and M5 models entered the NAE test facility, see Figure 1. ONERA's equivalent axisymmetric bodies were not included in the program, since investigation of lift interference rather than blockage was of prime concern. The model blockage ratios, based on the maximum section in a plane normal to the wind tunnel axis (about 50% greater than the fuselage cross-section) are given in Table 1.

The problem of subsonic lift interference on three-dimensional models in wind tunnels with perforated walls has been dealt with in a number of theoretical papers in the last couple of years. An approximation method based on the Fourier transform technique developed in Reference 8 for solving the two-dimensional problem, was reported in Reference 9. Since the solution is constructed in the form of series of velocity potentials, which correct the preceding ones for three-dimensional effects, it leads to extensive algebra and is difficult to use. However, some evaluated examples and useful tables can be found in Reference 10. The method of References 11 and 12, based on images in conjunction with Fourier transforms, is exact and easier to use, but can only be applied if either vertical or horizontal walls are solid. In References 13 and 14, while still depending on Fourier transforms, the wall interference potential is constructed in terms of infinite series, whose coefficients are found by satisfying the boundary conditions at a suitable number of points selected on the wind tunnel boundary. The idea of satisfying the boundary conditions at a discrete set of points is also the basis of the panel (lattice) methods. Their application to the wall interference in perforated wind tunnels is described in References 15-17.

The present report offers an alternative solution based on the finite difference method, which seems almost ideally suited to tunnels of rectangular cross-section. In connection with the wind tunnel interference problem, the conceptual simplicity of finite differencing was first appreciated by Rushton and Laing, Reference 18. Solutions obtained by them were based on dynamic relaxation, converting the steady flow problem to an unsteady one with a near-critical damping. In the present approach the resultant system of difference equations is solved by the generalized Newton's method (successive over-relaxation) described in Reference 19. The results of computation are used to examine trends in experimental data and to correct the measurements for wall interference effects.

2.0 EXPERIMENTAL PROGRAM

The main dimensions of the ONERA models and the upstream portions of the stings are given in Figure 2 and Table 1. The wing has an aspect ratio of 7.31, a taper ratio of 0.3 and the leading edge sweepback of 30°. The wing profile is symmetrical, 10.5% thick, which on the basis of pressure distributions may be classified as a peaky type, Reference 1. The same profile is used for the empennage. The M5 model is equipped with wing surface pressure orifices at three locations; two on the port wing and one on the starboard wing as illustrated in Figure 3.

The loads were measured with three different six-component balances, mounted inside the fuselages of the models: M1 — the original ONERA $\phi = 20$ mm, No. 4 balance, M3 — the 1-inch Task Mk XIVB balance on loan from NASA Ames, and M5 — the 2-inch NAE Task Mk XVIIIA balance.

The description of the NAE 5-ft. × 5-ft. wind tunnel and its operating parameters are given in Reference 20, but it may be in place to summarize the basic characteristics of the two 5-ft. × 5-ft. test sections, in which the ONERA models were tested. The scheme of the wind tunnel is given in Figure 4. The downstream portion of the flexible nozzle is used as the solid wall test section in the subsonic speed range up to about M = 0.85, at which the choking phenomena set in. The transonic test section, which can be operated up to and beyond M = 1, is inserted in tandem between the flexible nozzle and the diffuser. The walls are perforated by ½-inch diameter holes on 1.04 inch centres in staggered rows, giving an open area ratio of 20.5%. The flow through the walls into the surrounding plenum is controlled by ejector flaps at the inlet of the diffuser. Using two 80 inch long rails with static pressure orifices, details of which are given in Figure 5 and Reference 21, it is possible to measure the static pressure along the centre lines of the top and bottom walls.

The majority of the tests were conducted with five of the original seven settling chamber turbulence screens, two screens having failed during the course of tunnel operation prior to the tests. However, towards the end of testing the last model (M5), a third screen failure occurred and the remainder of the M5 test data was obtained with only four turbulence screens. Based on consultations with ONERA, all tests were performed in the free transition mode.

A graphical display of Reynolds numbers based on the aerodynamic mean chord of the wing and the Mach numbers covered during the tests is given in Figure 6. For testing in the solid wall test section the upper limit M = 0.86 applied, with the exception of model M1, for which M = 0.92 was reached. For greater economy, the variation of the Reynolds number was achieved by varying stagnation pressure during a wind tunnel run, the highest value being given by the stress limits of the balance or sting. In all tests performed the stagnation pressure was between a minimum of 18 psia and a maximum of 78 psia (at M = 0.25).

The balance measurements were conducted using a continuous pitching motion at about $5°$/sec., covering the range of angle of attack $-6°$ to $+10°$. The pressure measurements on the M5 model and the static pressure rails were obtained in a "step and pause" program, covering the range of incidence from $-3°$ to $+3°$, by $2°$ steps.

The results are presented in coefficient form in diagrams. The reference area S, on which the force and moment coefficients are based, is defined as the area of the wing planform, extended to the model axis. The pitching moment is further non-dimensionalized with respect to the aerodynamic mean chord $\bar{c}$. The position of the force and moment reference point (aerodynamic centre) is derived from the location of the quarter-chord point on the aerodynamic mean chord as shown in Figure 2.

The drag coefficient is corrected to a base pressure equal to free stream static pressure, this latter being obtained by correcting a reference static pressure measurement in accordance with empty test section calibration results. For the perforated wall test section the reference static pressure was the plenum chamber pressure, and for the solid wall test section a wall static pressure measured upstream of the model location.

3.0 THEORY

3.1 General Statement of the Lift Interference Problem

For steady incompressible flow over a model in a wind tunnel, the disturbance velocity potential is governed by the Laplace equation

$$\frac{\partial^2 \phi}{\partial x^2} + \frac{\partial^2 \phi}{\partial y^2} + \frac{\partial^2 \phi}{\partial z^2} = 0 \tag{1}$$

where x is the axis of a wind tunnel having a rectangular cross-section of width B and height H. Assuming the free stream velocity to be of unit magnitude and oriented in the direction of the positive x-axis, the model tangency condition is

$$\frac{\partial \phi}{\partial n} = \frac{1}{|\nabla S|} \frac{\partial S}{\partial x} \tag{2}$$

where $S(x, y, z) = 0$ describes the surface of the model and n is the normal, pointing outward from the flow field. The boundary condition for perforated wind tunnel walls is assumed to be

$$P \frac{\partial \phi}{\partial x} + \frac{\partial \phi}{\partial n} = 0 \tag{3}$$

where $0 \leqslant P < \infty$ is the porosity parameter. In analogy to the treatment of two-dimensional interference in Reference 21, we shall often utilize the factor

$$t = \frac{2}{\pi} \text{ atan } P \tag{4}$$

which is more suitable in graphical displays since it varies on the finite interval $0 \leqslant t < 1$.

Writing Equation (3) as separate boundary conditions for the four wind tunnel walls, we obtain

$$P \frac{\partial \phi}{\partial x} - \frac{\partial \phi}{\partial z} = 0 \text{ , bottom}$$

$$P \frac{\partial \phi}{\partial x} + \frac{\partial \phi}{\partial z} = 0 \text{ , top}$$

$$\tag{5}$$

$$P \frac{\partial \phi}{\partial x} - \frac{\partial \phi}{\partial y} = 0 \text{ , right}$$

$$P \frac{\partial \phi}{\partial x} + \frac{\partial \phi}{\partial y} = 0 \text{ , left}$$

In order to be able to treat walls which have variable porosity or perforated test sections of finite length, we shall assume that $P = P(x, y, z)$ is a function defined on the walls.

According to Reference 18, we use the following boundary conditions on the upstream and downstream control surfaces, normal to the x-axis:

$$\frac{\partial \phi}{\partial x} = 0 \text{ , upstream}$$

$$\tag{6}$$

$$\frac{\partial \phi}{\partial x} = 0 \text{ , downstream}$$

Conditions (6), which specify that the x-components of disturbance velocity vanish, appear as a very natural choice, especially when the control surfaces are sufficiently far from the model. However, an explanatory remark is needed. In the case of solid walls, P = 0, Equations (1), (2), (5) and (6) describe a Neumann problem. From Equation (2) it follows for the integral of the normal derivative over the body surface

$$\int_S \frac{\partial \phi}{\partial n} \, dS = 0 \tag{7}$$

and hence by Equations (6) the compatibility conditions for the Neumann problem are not violated. This means that in the computation we can approach the solid wall conditions by simply diminishing the *porosity factor* P → 0 without the need to modify the upstream or downstream conditions.

In cases where Equation (7) does not hold, such as the computation of wake blockage effects, Equations (6) contradict the compatibility conditions for a Neumann problem, and other, more suitable forms of upstream or downstream boundary conditions should be used, see for example, Reference 11.

Following common practice, we shall find the approximate solution of the wall interference problem by setting

$$\phi = f + g \tag{8}$$

where f is the far field potential of flow past the model in free air and g is the interference potential, which is assumed to be harmonic in the entire wind tunnel interior. Subsequently

$$\Delta \alpha = \frac{\partial g}{\partial z} \tag{9}$$

calculated at the position of the model represents the angle of attack correction.

It is important to note that in the process of the construction of the wall interference potential g, the field Equations (1) and (8) and the wind tunnel boundary conditions, Equations (5) and (6) are used, but not the model boundary condition*, Equation (2).

In view of the fact that the far field potential f is in the first approximation proportional to the lift force on the model, it is convenient to normalize $\Delta \alpha$ accordingly to form the upwash factor

$$\delta_o = \frac{A}{SC_L} \frac{\partial g}{\partial z} \tag{10}$$

where C_L is the lift coefficient, S is the model reference area (on which C_L is based), and

$$A = BH \tag{11}$$

_____

* The loss of the inner (model) boundary condition is a typical feature of outer solutions in perturbation theory. However, there is no other rigorous justification available yet for the above wall interference concept.

is the cross-sectional area of the wind tunnel. Once δ_o is evaluated, $\Delta\alpha$ is given by

$$\Delta\alpha = C_L \frac{S}{A} \delta_o \tag{12}$$

Since $\Delta\alpha$ is proportional to S/A it follows from Table 1 that for the same C_L and δ_o, the angle of attack correction on the M3 and M1 models is only 23.4% and 8.6% respectively of that on the M5 model.

The corresponding corrections to the lift, drag, and pitching moment coefficients are, to the first order of δ_o

$$\Delta C_L = 0$$

$$\Delta C_D = C_L \ \Delta\alpha = C_L^2 \frac{S}{A} \delta_o \tag{13}$$

$$\Delta C_M = 0$$

Over the linear portion of the lift curve, see Figure 7, the slope is

$$\frac{\partial C_L}{\partial \alpha} = \frac{C_L}{\alpha - \alpha_o}$$

where α_o is the zero lift angle. For the difference between the corrected and measured lift curve slopes it follows

$$\Delta \frac{\partial C_L}{\partial \alpha} = \frac{C_L}{\alpha - \alpha_o + \Delta\alpha} - \frac{C_L}{\alpha - \alpha_o} \cong - \frac{C_L}{(\alpha - \alpha_o)^2} \Delta\alpha = - \left(\frac{\partial C_L}{\partial \alpha}\right)^2 \frac{\Delta\alpha}{C_L}$$

Substituting for $\Delta\alpha$ from Equation (12) we finally obtain the approximate formula for the correction to the lift curve slope

$$\Delta \frac{\partial C_L}{\partial \alpha} = - \left(\frac{\partial C_L}{\partial \alpha}\right)^2 \frac{S}{A} \delta_o \tag{14}$$

Here and in Equations (12) and (13) the angle α is, of course, in radians.

Similarly to the upwash factor, one often introduces the streamline curvature factor, see References 22 and 23,

$$\delta_1 = \frac{HA}{C_L S} \frac{\partial^2 g}{\partial x \, \partial z} \tag{15}$$

which is the measure of the streamwise variation of $\Delta\alpha$. The variation of $\Delta\alpha$ along the wing chord may be interpreted in terms of wall induced distortion of the camber of a thin wing, and used to derive residual corrections to C_L and C_M. Since the residual corrections evaluated in such a way usually fall well below the level of experimental errors, we shall assume that Equations (13) hold.

Also, if the flow environment of the model in the wind tunnel should resemble that in free air, δ_1 has to be kept close to zero. The extent of the spanwise variation of $\Delta\alpha$, which for a wing of

moderate to high aspect ratio is in this regard perhaps even more important, can be best examined by direct evaluation of δ_0 along the span.

To compare the measured wall pressure distributions with the results of present theory, we use the linearized formula

$$C_p = -2 \frac{\partial \phi}{\partial x} \tag{16}$$

which holds with sufficient accuracy at large distances from the model. In order to be consistent with the evaluation of the angle of attack correction, which is also derived from a first derivative of the disturbance potential, we introduce the wall pressure factor

$$\delta_p = \frac{A}{SC_L} \left(-2 \frac{\partial \phi}{\partial x} \right) = -2 \frac{A}{SC_L} \left(\frac{\partial f}{\partial x} + \frac{\partial g}{\partial x} \right) \tag{17}$$

Once δ_p is evaluated, the pressure coefficient follows from the formula

$$C_p = C_L \frac{S}{A} \delta_p \tag{18}$$

3.2 Representation of the Model

The far field associated with the lift for a swept wing of moderate to large aspect ratio can in a simple way be represented by a lifting line placed along the quarter chord line of the wing. The load distribution is assumed to be elliptic, and no account is taken of separate lift contributions from other parts of the model, notably the tail surfaces. The model is further assumed to have spanwise symmetry about the x-z plane (zero yaw).

With these simplifications we may represent the model by discrete horseshoe vortices lying on lines inclined to the y-axis at sweep angles τ as indicated in Figure 8. The wing semi-span b/2 is divided into N equal intervals, at whose centres

$$y_k = \frac{b}{2} \left(\frac{N-k}{N} + \frac{1}{2N} \right) \tag{19}$$

$$x_k = y_k \tan \tau$$

are placed horseshoe vortices described by the potentials

$$f_k = \frac{\gamma_k}{4\pi} \frac{z}{(y - y_k)^2 + z^2} \left[1 + \frac{x - x_k}{\sqrt{(x - x_k)^2 + (y - y_k)^2 + z^2}} \right] \tag{20}$$

The vortex strength γ_k is set equal to the area under the load distribution curve, corresponding to the k-th interval, see Figure 8. For elliptic load distribution γ_k is obtained (apart from a multiplicative constant) as a difference of two circular segments constructed at the end points of the k-th interval:

$$\gamma_k = \frac{1}{2\pi} \left\{ \text{arcos} \frac{N-k}{N} - \frac{N-k}{N} \sqrt{1 - \left(\frac{N-k}{N} \right)^2} \right\} - \sum_{j=1}^{k-1} \gamma_j \tag{21}$$

$$k = 1, 2, \ldots, N$$

Utilizing the spanwise symmetry of the model

$$x_{-k} = x_k$$

$$y_{-k} = {}^-y_k \tag{22}$$

$$\gamma_{-k} = \gamma_k$$

we obtain the free air potential f of the entire model by summing all contributions:

$$f = \sum_{k=1}^{N} (f_k + f_{-k}) \tag{23}$$

Using Equation (21) we evaluate the circulation

$$\Gamma = \sum_{k=1}^{N} (\gamma_k + \gamma_{-k}) = \frac{1}{2}$$

Since by the Joukowski theorem generally

$$\Gamma = \frac{1}{2} SC_L$$

we find that the above representation of potential f by Equations (20) and (21) corresponds to the case $SC_L = 1$.

Referring to Equations (10) and (15), the corresponding interference factors are computed as

$$\delta_o = A \frac{\partial g}{\partial z} \tag{24}$$

$$\delta_1 = HA \frac{\partial^2 g}{\partial x \partial z} \tag{25}$$

Similarly, from Equation (17)

$$\delta_p = -2A \left(\frac{\partial f}{\partial x} + \frac{\partial g}{\partial x} \right) \tag{26}$$

3.3 Finite Difference Equations

The equations of Section 3.1 are approximated by second-order accurate finite difference equations. The grid is organized as shown on the example $k = 2$, $m = 4$ in Figure 9. The finite difference analogue of Equation (1) is

$$r_x \, g_{i-(m+1)(k+1)} + r_y \, g_{i-(m+1)} + r_z \, g_{i-1} + g_i +$$

$$r_z \, g_{i+1} + r_y \, g_{i+(m+1)} + r_x \, g_{i+(m+1)(k+1)} = 0 \qquad (27)$$

where

$$r_x = r/(\Delta x)^2$$

$$r_y = r/(\Delta y)^2$$

$$(28)$$

$$r_z = r/(\Delta z)^2$$

$$r = -\frac{1}{2}\left[1/(\Delta x)^2 + 1/(\Delta y)^2 + 1/(\Delta z)^2\right]^{-1}$$

The finite difference forms of Equations (5) are

$$P\,\frac{g_{i+(m+1)(k+1)} - g_{i-(m+1)(k+1)}}{2\Delta x} - \frac{g_{i+1} - g_{i-1}}{2\Delta z} = -F_B$$

$$P\,\frac{g_{i+(m+1)(k+1)} - g_{i-(m+1)(k+1)}}{2\Delta x} + \frac{g_{i+1} - g_{i-1}}{2\Delta z} = -F_T$$

$$(29)$$

$$P\,\frac{g_{i+(m+1)(k+1)} - g_{i-(m+1)(k+1)}}{2\Delta x} - \frac{g_{i+(m+1)} - g_{i-(m+1)}}{2\Delta y} = -F_R$$

$$P\,\frac{g_{i+(m+1)(k+1)} - g_{i-(m+1)(k+1)}}{2\Delta x} + \frac{g_{i+(m+1)} - g_{i-(m+1)}}{2\Delta y} = -F_L$$

where

$$F_B = P\,\frac{\partial f}{\partial x} - \frac{\partial f}{\partial z}\,,\ \text{bottom}$$

$$F_T = P\,\frac{\partial f}{\partial x} + \frac{\partial f}{\partial z}\,,\ \text{top}$$

$$(30)$$

$$F_R = P\,\frac{\partial f}{\partial x} - \frac{\partial f}{\partial y}\,,\ \text{right}$$

$$F_L = P\,\frac{\partial f}{\partial x} + \frac{\partial f}{\partial y}\,,\ \text{left}$$

are evaluated from Equations (20)-(23).

Similarly, Equations (6) yield

$$\frac{g_{i + (m + 1)(k + 1)} - g_{i - (m + 1)(k + 1)}}{2\triangle x} = -F_U$$

$$\frac{g_{i + (m + 1)(k + 1)} - g_{i - (m + 1)(k + 1)}}{2\triangle x} = -F_D$$

(31)

where

$$F_U = \frac{\partial f}{\partial x} \text{ , upstream}$$

(32)

$$F_D = \frac{\partial f}{\partial x} \text{ , downstream}$$

3.4 Relaxation Procedure

The equation for each mesh point can be written as follows

$$a_{i - (m + 1)(k + 1)} \, g_{i - (m + 1)(k + 1)} + a_{i - (m + 1)} \, g_{i - (m + 1)} +$$

$$a_{i - 1} \, g_{i - 1} + g_i + a_{i + 1} \, g_{i + 1} + a_{i + (m + 1)} \, g_{i + (m + 1)} +$$

$$a_{i + (m + 1)(k + 1)} \, g_{i + (m + 1)(k + 1)} = b_i$$

$$i = 1, \ldots, n$$

(33)

For interior points, Equation (33) is identical with Equation (27). For boundary points, however, the exterior points have to be eliminated using the corresponding boundary conditions. Thus, for example, on the bottom left edge, the terms $g_{i - 1}$ and $g_{i + (m + 1)}$ in Equation (27) are eliminated using the first and the last of Equations (29). Similar steps are taken for all 6 sides, 12 edges and 8 corners. Basic assumption for this approach is, of course, that the solution exists up to the layer of the eliminated (virtual) points. Using the concept of images, it can be shown that this is certainly true if the smallest distance of the model from the boundary is bigger than max $(\triangle x, \triangle y, \triangle z)$.

For the disturbance potential f represented by Equations (20)-(23), a complete spanwise symmetry of the wind tunnel flow is obtained if

$$P(x, y, z) = P(x, -y, z)$$

In this case a significant reduction in the number of equations is achieved by cutting off the right half of the wind tunnel by the reflection plane x, z, as shown in Figure 9. The finite difference equation to be considered for points in the x, y plane is Equation (27) where $g_{i + (m + 1)}$ substitutes $g_{i - (m + 1)}$.

The system of linear algebraic Equations (33) is solved by the generalized Newton's method (successive over-relaxation) described in detail in Reference 19. Denoting by the superscript + the updated value we obtain the iteration formula

$$
\begin{aligned}
g_i^+ = g_i - \omega \Big[& a_{i-(m+1)(k+1)} \, g_{j-(m+1)(k+1)}^+ + \\
& a_{i-(m+1)} \, g_{i-(m+1)}^+ + a_{i-1} \, g_{i-1}^+ + g_i + \\
& a_{i+1} \, g_{i+1} + a_{i+(m+1)} \, g_{i+(m+1)} + \\
& a_{i+(m+1)(k+1)} \, g_{i+(m+1)(k+1)} - b_i \Big]
\end{aligned}
\tag{34}
$$

which is applied to all mesh points in the sequence $i = 1, 2, \ldots, n$ as indicated in Figure 9. The relaxation factor ω is found by experimentation in the range $0 < \omega < 2$.

Using Equations (27), (29) and (31) it is easy to show that the matrix of the system (33) is diagonally dominant if

$$
\Delta x \leqslant \min \left(\frac{\Delta z}{P}, \frac{\Delta y}{P} \right)
\tag{35}
$$

In this case a fast convergence of the iteration scheme is obtained for the values $\omega > 1$ (over-relaxation). If the above inequality does not hold, convergence for moderate values P may still be obtained, especially when taking a suitable $\omega < 1$ (under-relaxation), but in general, the success of the method becomes less certain. The method fails if $P \to \infty$, that is when approaching the open jet conditions*, since the reduction of spacing $\Delta x \to 0$ is not feasible.

The derivatives needed to evaluate the interference factors, Equations (24) and (25) are approximated by the central formulae

$$
\frac{\partial g}{\partial z} \cong \frac{1}{2\Delta z} \left[g_{i+1} - g_{i-1} \right]
\tag{36}
$$

$$
\frac{\partial^2 g}{\partial x \, \partial z} \cong \frac{1}{4\Delta x \, \Delta z} \Big[g_{i+1+(m+1)(k+1)} - g_{i-1+(m+1)(k+1)} - g_{i+1-(m+1)(k+1)} + g_{i-1-(m+1)(k+1)} \Big]
\tag{37}
$$

The pressure factor, Equation (26), is obtained by evaluating $\partial f/\partial x$ from Equations (20)-(23) and by approximating

$$
\frac{\partial g}{\partial x} \cong \frac{1}{2\Delta x} \left[g_{i+(m+1)(k+1)} - g_{i-(m+1)(k+1)} \right]
\tag{38}
$$

___

* Similar symptoms can also be detected in the circular wind tunnel theory, Reference 8, where the lift interference potential becomes discontinuous on an interval of porosities containing the point $P = \infty$. The physical reason for this behaviour is that the pressure dependent boundary of an open jet deflects far downstream in the presence of the lift force on the model. The confinement of the open jet by a cylindrical or prismatic boundary is hence not physically reasonable.

The wind tunnel parameters entering Equations (24)-(26) are (symmetrical case)

$$H = m \, \Delta z$$

$$B = 2k \, \Delta y \qquad\qquad (39)$$

$$A = 2km \, \Delta y \, \Delta z$$

3.5 Calculation for the M5 Model

Calculations were performed for the configuration corresponding to the M5 model in the NAE 5-ft. $\times$ 5-ft. wind tunnel. In the computational space, the parameters of the wind tunnel were $B = H = 1$. The model was represented as described in Section 3.2, taking $N = 10$, $\tau = 26.73°$ and $b = 0.644$. The left half of the wind tunnel was specified by $-4 \leqslant x \leqslant 4$, $0 \leqslant y \leqslant 0.5$, $-0.5 \leqslant z \leqslant 0.5$, choosing $\Delta x = \Delta y = \Delta z = 0.1$, which resulted in $n = 5346$ equations. In accordance with the length of the perforated test section, it was assumed that $P \geqslant 0$ for $|x| \leqslant 1.2$ and $P = 0$ for $1.2 < |x| \leqslant 4$. The computations were performed for the values of the factor t, Equation (4), increased by steps of 0.1. The initial guess was $g_i = 0$, $i = 1, \ldots, n$. The convergence was checked every 10th iteration and the computation terminated when the absolute value of the difference between the right and left sides of Equation (33) was less than 0.001 for all $i = 1, \ldots, n$. The relaxation factor was selected as $\omega = 1.5$ and reduced successively by 0.2 until convergence was obtained. Table 2 indicates the resultant relaxation factors and the number of iterations needed to achieve the required accuracy. It may be observed that divergence problems arise in accordance with the criterion (35) once $P > 1$. For porosity factors higher than those listed in Table 2 the convergent solution may be obtained by reducing Δx at the cost of an increased number of equations, but, as mentioned before, the method is not expected to work near the open jet conditions, $t \rightarrow 1$.

Figures 10(a)-(b) show the resultant upwash and the streamline curvature factors, calculated from Equations (24) and (25) at the wing tip

$$y = \frac{b}{2} = 0.322$$

the centre of elliptic load distribution

$$y = \frac{b}{2} \frac{4}{3\pi} \cong 0.137$$

and the wing root

$$y = 0$$

For the evaluation of the angle of attack correction from Equation (12), the most representative value of δ_o is that associated with the centre of the load distribution. The spread of values δ_o between the tip and the root of the wing characterizes the non-uniformity of the wind tunnel flow over the model (wall induced wing twist). It is seen that for the solid wall test section, $t = 0$, the 70% difference in δ_o between the tip and the root of the wing is quite extreme, but the situation improves greatly as t increases up to about $t = 0.7$. The streamline curvature factor δ_1, exhibits a similar improvement as porosity increases. However, for uniformity of the wind tunnel flow it is necessary that δ_o = constant and $\delta_1 = 0$ all over the wing. Unfortunately, from Figures 10(a)-(b) it appears that these conditions cannot be met simultaneously. As a result, the flow over the model in a wind tunnel

of the present type is always to some extent non-uniform, and it should be no surprise that in some cases the representation of the lift interference by a single angle of attack correction is not adequate.

It is interesting to compare the present results with some known exact solutions. In the case of solid walls, we may use the infinite series solutions by Theodorsen for a rectangular test section and a model represented by a horseshoe vortex of infinitesimal span, located on the wind tunnel axis. From Reference 22 it follows, for $B = H$, that

$$\delta_o = \frac{\pi}{24} + \pi \sum_{n=1}^{\infty} \frac{n}{e^{2\pi n} + 1} \cong 0.137, \quad t = 0$$

$$\delta_1 = \frac{1}{2\pi} \sum_{n=1}^{\infty} \left[\frac{0.5 - (-1)^n}{n^3} + (-1)^n \sum_{m=1}^{\infty} \frac{m^2 - 2n^2}{(m^2 + n^2)^{5/2}} \right] \cong 0.236, \quad t = 0$$

From Figure 10(a) it is seen that Theodorsen's value is very close to our solution for δ_o at the load distribution centre of a finite span wing. For δ_1 in Figure 10(b) Theodorsen's result is closer to our wing tip solution. However, no conclusion can be drawn from this since, clearly, we are comparing two different flow cases.

For comparison with the perforated wall computations, we may use the Fourier integral solutions of Reference 8, obtained for an infinitely long circular test section and a model represented by a horseshoe vortex of infinitesimal span, located on the wind tunnel axis. From Figures 10(a)-(b) it is seen that the circular test section theory approximates our numerical result for a square test section adequately, except perhaps for higher porosity, where the effect of the finite length of the perforated test section becomes important. Reference 15 shows that even the spanwise variation of δ_o can be extracted from the circular test section theory reasonably well.

3.6 Compressibility Transformation

To account for the first order effect of compressibility at subsonic Mach numbers, we assume the governing equation in the linearized form

$$\beta^2 \frac{\partial^2 \phi}{\partial \tilde{x}^2} + \frac{\partial^2 \phi}{\partial y^2} + \frac{\partial^2 \phi}{\partial z^2} = 0 \tag{40}$$

where

$$\beta = \sqrt{1 - M^2} \tag{41}$$

The Goethert-Prandtl-Glauert transformation

$$x = \frac{\tilde{x}}{\beta} \tag{42}$$

where y, z, and ϕ are kept invariant, see Reference 24 reduces Equation (40) to Equation (1). Here, and in what follows, the symbols with a tilde denote the compressible flow variables which are subject to the transformation.

Assuming the boundary condition for a perforated wall in the form

$$\widetilde{P} \; \frac{\partial \phi}{\partial \widetilde{x}} \; + \; \frac{\partial \phi}{\partial n} \; = \; 0 \qquad (43)$$

where $\widetilde{P}$ is the porosity parameter in compressible flow, we arrive at Equations (3)-(5) by taking

$$P \; = \; \frac{\widetilde{P}}{\beta} \qquad (44)$$

The upstream and downstream boundary conditions (6) are retrieved immediately in the compressibility transformation.

The length of the porous part of the wind tunnel transforms according to Equation (42). Similarly, for the transformed sweep angle we obtain

$$\tan \tau \; = \; \frac{1}{\beta} \; \tan \widetilde{\tau} \qquad (45)$$

where $\widetilde{\tau}$ is the actual sweep angle of the wing.

In this way the compressible flow problem is reduced to the incompressible one we have solved above. Since the disturbance potential ϕ is invariant under the transformation, we obtain from Equations (10) and (15) the relationships between the interference factors in compressible and the transformed (incompressible) flows

$$\widetilde{\delta}_o \; = \; \delta_o \qquad (46)$$

$$\widetilde{\delta}_1 \; = \; \frac{\delta_1}{\beta} \qquad (47)$$

Because of the identity (46) we shall retain the symbol δ_o for the upwash factor in the compressible flow. Referring to Equations (17) and (42) we obtain the pressure factor

$$\widetilde{\delta}_P \; = \; \frac{\delta_P}{\beta} \qquad (48)$$

which expresses the well known relation between the pressure coefficients in compressible and incompressible flows under the Goethert-Prandtl-Glauert law.

Using the values in Figure 10(a) and Equations (4), (41), and (44), the upwash factor for a circular test section is plotted in Figure 11 as a function of M, for various values of $\widetilde{P}$. In connection with Equation (12) the graph may be useful for estimation of the angle of attack correction on models of moderate span in a perforated square test section.

However, in order to calculate the lift interference on a model of a large wing span to tunnel width ratio, for which the circular wind tunnel theory is less appropriate, we have to carry out the compressibility transformation and numerical calculations as described above.

Figure 12 presents the results of computation for the M5 model in the NAE 5-ft. $\times$ 5-ft. test facility having solid walls, $\widetilde{P} = 0$, and perforated walls, $\widetilde{P} = 1.2$. The latter value of the porosity factor, associated with the 20.5% porous walls in the ranges $0.25 \leqslant M \leqslant 0.85$ and $4 \times 10^6 \leqslant Re \leqslant 5 \times 10^6$, was found by evaluating the pressure distributions measured along the wind tunnel walls and by comparing the force coefficients measured in the solid and perforated test sections.

Based on the difference between the upwash factors at the tip and the root of the wing we may conclude that the porous wall test section establishes a much more uniform flow over the model than the solid wall test section does. The curves for the centre of the load distribution are quite well approximated by the curves in Figure 11 obtained from the circular test section theory. The angle of attack correction is positive for $\widetilde{P} = 0$ and negative for $\widetilde{P} = 1.2$, a fact which will be verified by the experimental data discussed in Section 4.0.

4.0 ANALYSIS OF EXPERIMENTAL DATA

The results given here represent only a small portion of the entire experimental data obtained from the ONERA model tests, Reference 25.

Figures 15(a)-(f) contain plots of drag coefficients at zero lift versus stream Mach number. The agreement between the data obtained in the solid and perforated test sections on models M5 and M3, having blockage ratios 0.79% and 0.18% respectively, leads to the conclusion that blockage effects on ONERA models in the Mach number range $0 \leqslant M \leqslant 0.85$ are insignificant. Interestingly, some discrepancies appear at low Mach numbers for the M1 model where, judged by the blockage ratio of 0.07%, they are least expected. However, it should be noted that, for a sting mounted model, the blockage ratio of the model is not the only factor determining the blockage. In the case of the M1 model it is the long sting, having the blockage ratio of 0.09%, and the sting support system which account for most of the blockage interference on the relatively small model, see Figure 1. However, since we have not succeeded in explaining the drag discrepancies quantitatively, the M1 model data is not considered for model to model comparisons.

In contrast to the drag vs. Mach number data, the plots of lift curve slope vs. Mach number in Figures 16(a)-(f), even though displaying larger scatter, do show wall interference effects which increase with the size of the model. The slopes $\partial C_L / \partial \alpha$ were evaluated from the measured discrete values of C_L and α, an example of which is given in Figure 18, using linear regression in the interval $-5° \leqslant \alpha \leqslant 1°$. By capturing about 10 data points inside such a wide interval, it was possible to keep the standard error relatively small — about the size of symbols in Figures 16(a)-(f) — which is essential for detecting small interference effects. On the other hand, we are aware that the result obtained by averaging over the above interval may not exactly represent the true value of the slope at $C_L = 0$. In fact, observing Figure 18(a), it appears that the tangent to the C_L vs. α curve tends to vary rapidly in the vicinity of $C_L = 0$. The data given in Reference 25 shows that this phenomenon seems to be characteristic. Nevertheless, the expected trends of $\partial C_L / \partial \alpha$ with a large dip near $M = 0.92$ are still retained, as may be verified by comparing with graphs in References 5 and 6.

Figures 16(a)-(f) compare the data from the solid and perforated test sections, for the same model and the same Reynolds number. In the case of the M5 model, Figures 16(a)-(b), it is seen that solid walls yield distinctly higher values of $\partial C_L / \partial \alpha$ than perforated walls. For models M3 and M1, Figures 16(c)-(f), the effect of wind tunnel interference is inconclusive, masked by experimental errors. This is particularly disappointing in the case of the M3 model where, based on the ratio S/A in Table 1, the difference between the solid and perforated wall data should still account for 23.4% of that on the M5 model. The value 8.3%, associated with S/A for the M1 model, indicates that from a practical point of view the measurement should be free from lift interference. Unlike the blockage interference, we may assume that the sting and the sting support system do not contribute to the lift interference, since at low angles of attack they do not generate a significant lift force. Unfortunately, no valid comparisons between the measurements on model M5 and model M1 could be carried out because of the large difference in Reynolds numbers, see Figure 6. We shall, therefore, base our analysis on comparisons of measurements on the same models in solid and perforated test sections.

Figures 17(a)-(b) show the lift curve slopes for the M5 model corrected according to Equation (14) and the calculated upwash factors in Figure 12, corresponding to the centre of load distribution. The vertical line segments are traces of the symbols as they moved from the uncorrected to the corrected positions. It is seen that the negative corrections for solid walls and the positive corrections for perforated walls bring the data into fairly good agreement. In Figures 17(c)-(d) a similar procedure was carried out for the M3 model. In view of the smallness of the corrections, the effect on the M3 model is much less pronounced. The corrected left curve slopes for model M1 are not included, since at the scale used they would look identical to the uncorrected slopes in Figures 16(e)-(f).

To further substantiate the choice $\widetilde{P} = 1.2$ for the perforated wall test section and check on the validity of Equation (43), we compare the measured wall pressure distributions with those calculated from Equation (18). Figure 13 illustrates the wall-model M5 configuration and Figures 14(a)-(b) the wall pressure distributions for two typical Mach numbers and four levels of angle of attack. Besides the investigated case $\widetilde{P} = 1.2$, the calculations are also performed for $\widetilde{P} = 0$ to indicate the extremum of C_p which may theoretically be reached at the walls. It is seen that the wall pressures measured along the perforated walls roughly correspond to those computed for $\widetilde{P} = 1.2$, but in general, the measurement is far less rewarding than the earlier one reported in Reference 21 in connection with two-dimensional testing. The relatively large scatter of the wall pressure data is believed to be due to local flow non-uniformities originated by the perforations. Since in three dimensions the model pressure disturbances decay much faster with distance from the model than they do in two dimensions, they are attenuated to lower levels at the distant wind tunnel walls, and appear to be relatively more perturbed by the perforations. On the other hand, the low level of model pressure disturbances in the vicinity of the walls indicates that the wall induced effect on a three-dimensional model is correspondingly small, and that there is no real need to determine the porosity factor with great accuracy.

Figures 14(a)-(b) suggest the presence of small blockage effects in the zero lift case (the measured points indicate $C_p \neq 0$) and the presence of asymmetry at higher C_L (the magnitude of C_P is greater on the bottom wall than on the top wall). The latter observation is in agreement with earlier findings of Reference 21 that Equation (43) only approximates the true behaviour of a perforated wall. Because of the large experimental scatter, however, the present wall pressures could not be analyzed in greater detail.

Figures 19(a)-(f) show a typical selection of lift vs. corrected angle of attack data for the M5 model. The angle of attack correction, evaluated from Equation (12) and Figure 12, is displayed as a horizontal line segment attached to each symbol. The correspondence between the corrected data from solid and perforated test sections is seen to be very good up to about $C_L = 0.5$. As C_L increases, the inadequacy of a uniform angle of attack correction, particularly for the solid wall case, is readily apparent from Equation (12) and Figure 12. However, based on the magnitude of the spanwise variation of the upwash factor, we expect that the perforated test section gives a more reliable result even at higher C_L, whereas in the solid wall test section significant spanwise twist is induced.

Figures 20 and 21(a)-(g) give a similar selection of drag polars. The uncorrected data in Figure 20 indicates an appreciable difference between the measurements in the solid and perforated test sections, which in Figure 21(a) is reduced by applying the correction to the drag coefficient according to Equation (13). The line segments attached to the symbols again indicate the magnitude of the corrections. From Figures 21(b)-(g), showing only the corrected data, it is evident that it may again be difficult to establish agreement between the measurements if $C_L > 0.5$.

An interesting demonstration of the discrepancies between the data from the solid and perforated test sections at $C_L > 0.5$ is found in the graphs of the pitching moment versus the lift coefficient in Figures 22(a)-(d). In the context of the present theory, neither C_M nor C_L are subject to wall corrections, see Equation (13). It is observed that the good agreement between the solid and perforated test section data at M = 0.254 disappears at M = 0.505 and 0.705 to reappear at M = 0.840. Discrepancies of somewhat smaller magnitude, but not diminishing with the S/A ratio, can also be observed on the pitching moment coefficients for models M3 and M1, see Reference 25. This seems to exclude the possibility of explaining the differences between the solid and perforated test section data entirely in terms of wall interference effects. Since the pitching moment is more sensitive to local

changes in pressure distributions than the lift force, it is not unlikely that the observed effect is partly due to the difference in the flow quality of the two test sections.

Interesting observations can also be made by inspecting the lift coefficients of the three instrumented wing sections of the M5 model, shown in Figure 3. The section lift coefficients C_{L1}, C_{L2}, and C_{L3}, obtained by integrating the pressures at sections S1, S2, and S3 respectively, are plotted against the model lift coefficient C_L at M = 0.504, 0.705, and 0.840 in Figures 23(a)-(c). If $\Delta\alpha$ were uniform over the wing span then, in the absence of other wind tunnel wall effects, the lift coefficients from the solid and perforated test sections would form a single line for each model section. It is seen, however, that for $C_L > 0.5$ this is not always true and that the discrepancy first occurs at the most outboard stations.

To study this phenomenon we present in Figures 24-26 the detailed pressure distributions at the wing sections S1, S2, and S3. The pressure curves at M = 0.504, Figures 24(a)-(c), indicate that by increasing the model lift coefficient C_L the supercritical flow, $C_p < C_p^*$, occurs first in the tip region of the wing (section S1) and then gradually spreads to the root (sections S2 and S3). The supersonic zone, located near the leading edge of the wing, is terminated by a shock wave and a large isentropic recompression, which is characteristic of a peaky type profile. As far as the comparison between the data from the solid and perforated test sections is concerned, we may note that at M = 0.504 the flow is essentially attached and that both sets of pressure curves display a great deal of similarity. As a result, the section lift coefficients C_{L1}, C_{L2}, and C_{L3} form single lines when plotted against the model lift coefficient C_L in Figure 23(a).

At M = 0.705, Figures 25(a)-(c), there is a marked departure from the similarity between the pressure curves at the section S1, when the model lift coefficient C_L is above 0.5. The solid wall data exhibits a decrease in the maximum suction pressure, a flattening of the pressure curve over the upper surface, and the divergence of the trailing edge pressure, which are typical of rear separation. The symptoms of rear separation can also be found on the S1 pressure curves associated with the perforated test section. It is rather unfortunate that the measurements in the solid and perforated test sections were not carried out at the same model lift coefficients, so that it could have been demonstrated more clearly that the rear separation in the perforated test section occurs at a higher value of C_L. Nevertheless, the resultant difference between C_{L1} from the solid and perforated test sections is sufficiently apparent from Figure 23(b). The flow tends to stay attached at the wing sections S2 and S3 and hence the section lift coefficients C_{L2} and C_{L3} in Figure 23(b) do not display dependence on the type of the wind tunnel test section. Based upon an examination of Figure 12, the above effect may partly be attributed to a large spanwise variation of the upwash factor in the solid wall test section, giving an excessive angle of attack correction in the tip region of the wing, but also, as mentioned earlier, to the difference in the flow quality of the solid and perforated test sections. Once large regions of separated flow on the model exist, the correlation of the test data from different test sections is uncertain.

At M = 0.840, Figures 26(a)-(c), the flow is supercritical at all angles of attack. The rear separation is observed at sections S1 and S2, and as a result both C_{L1} and C_{L2} in Figure 23(c) depend on the type of the wind tunnel test section once $C_L > 0.5$.

In the absence of surface flow visualization we did not attempt to analyse the pressure distributions in greater detail. The complexity of the flow over the wing of the ONERA aircraft model is best documented in Reference 26, where both pressure measurements and flow visualization results are discussed.

5.0 CONCLUSIONS

1.	The measurements in the NAE 5-ft. $\times$ 5-ft. test facility on the ONERA calibration models M5 and M3, having blockage ratios of 0.79% and 0.18% respectively, did not show significant blockage effects for Mach numbers below 0.85. The discrepancy between the drag coefficients from the solid and perforated test sections for the M1 model, having a blockage ratio of 0.07%, is not fully explained. Presumably, there exists a certain optimum size of the model for achieving the most reliable wind

tunnel measurement. Based on the analysis of the ONERA models, it is suggested that the model should have a wing span to wind tunnel width ratio of about 0.5 and a blockage ratio of about 0.5%.

2.   The lift interference effects on models M1 and M3, having wing span to wind tunnel width ratios of 0.188 and 0.311 respectively, were found to be within the limits of experimental errors. For the M5 model, having a wing span to wind tunnel width ratio of 0.644, the solid and perforated test section measurements, corrected using a uniform angle of attack correction, show good agreement up to lift coefficients of about 0.5.

3.   For the M5 model at lift coefficients higher than 0.5, the correlation of the test data from the solid and perforated test sections is less satisfactory if a uniform angle of attack correction is applied. Based on computations by the present finite difference method, the test section with 20.5% perforated walls is expected to produce a more uniform distribution of the angle of attack correction along the wing span, and hence to yield more reliable test data than the test section with solid walls.

4.   The wall pressure measurements can be used to check on the value of the porosity parameter ascribed to the perforated walls, with the aid of the present finite difference method. The discrete disturbances from the perforations prove to be a much greater obstacle in utilising the wall pressure measurements than is the case in two-dimensional testing.

5.   The correlation of test results from different wind tunnel test sections, and the evaluation of wind tunnel wall interference, become uncertain if large regions of flow separation are formed on the model.

6.0 ACKNOWLEDGEMENTS

7.0 REFERENCES

1.   Poisson-Quinton, Ph.   *Information in a Round-Table Discussion on ONERA Calibration Models.*
AGARD-CP-83-71, April 1971, pp. B7-B12.

2.   Vaucheret, X.   *Comparaison de souffleries transsoniques à l'aide de maquettes étalons ONERA.*
Laws Paper No. 77, April 1972.

3.   Lorenz-Meyer, W.   *Vergleichsmessungen an drei geometrisch ähnlichen Eichmodellen eines Transportflugzeugtyps im transsonischen Windkanal der AVA Göttingen.*
AVA 72 a 29, Deutsche Forschungs- und Versuchsanstalt für Luft- und Raumfahrt, October 1972.

4.   Gudmundson, S.E.   *Comparative Tests with ONERA Airplane Calibration Models in FFA Transonic Wind Tunnels.*
Euromech 40 Colloquium, Stockholm, September 1973.

5.   Vaucheret, X.   *Corrections de parois en écoulement tridimensionnel transsonique dans des veines à parois ventilées.*
     Vayssaire, J.-Ch.   AGARD-CP-174, Paper No. 16, October 1975.

6. Vaucheret, X.   *Corrections de parois en transsonique.*
                             12ème Colloque d'aérodynamique appliquée ENSMA/CEAT, Poitiers,
                             November 1975.

7. Binion, T.W.   *Tests of the ONERA Calibration Models in Three Transonic Wind
                             Tunnels.*
                             TR-76-33, Arnold Engineering Development Center, November 1976.

8. Baldwin, B.S.   *Wall Interference in Wind Tunnels with Slotted and Porous Boundaries*
    Turner, J.B.   *at Subsonic Speeds.*
    Knechtel, E.D.   NACA Tech. Note 3176, May 1954.

9. Wright, R.H.   *Approximation of the Spanwise Distribution of Wind-Tunnel-*
    Schilling, B.L.   *Boundary Interference on Lift of Wings in Rectangular Perforated-*
                             Wall Test Section.
                             NASA TR R-285, May 1968.

10. Schilling, B.L.   *Calculated Wind-Tunnel-Boundary Lift-Interference Factors for*
    Wright, R.H.   *Rectangular Perforated Test Sections.*
                             NASA TN D-5635, January 1970.

11. Kraft, E.M.   *Upwash Interference on a Symmetrical Wing in a Rectangular*
                             Ventilated Wall Wind Tunnel: Pt. I — Development of Theory.
                             TR-72-187, Arnold Engineering Development Center, March 1973.

12. Kraft, E.M.   *A General Solution for Lift Interference in Rectangular Ventilated*
    Lo, C.-F.   *Wind Tunnels.*
                             AIAA Paper No. 73 — 209, 1973.

13. Lo, C.-F.   *Boundary Interference in a Rectangular Wind Tunnel with Perforated*
    Oliver, R.H.   *Walls.*
                             TR-70-67, Arnold Engineering Development Center, February 1970.

14. Lo, C.-F.   *Subsonic Lift Interference in a Wind Tunnel with Perforated Walls.*
    Oliver, R.H.   Journal of Aircraft, Vol. 7, 1970, pp. 281-283.

15. Keller, J.D.   *A Numerical Method of Calculating the Boundary-Induced Interference*
    Wright, R.H.   *in Slotted or Perforated Wind Tunnels of Rectangular Cross-Section.*
                             NASA TR-R-379, November 1971.

16. Joppa, R.G.   *A Method of Calculating Wind Tunnel Interference Factors for*
                             Tunnels of Arbitrary Cross-Section.
                             NASA CR-845, July 1967.

17. Borovik, Y.   *Wind Tunnel Boundary Interference Corrections: Pt. I — Theoretical*
    Wasserstrom, E.   *Calculations.*
    Rom, J.   LR 0-124, Aeronautical Research Center, Technion — Israel Institute
                             of Technology, September 1972.

18. Rushton, K.R.   *A Digital Solution of the Laplace Equation Using the Dynamic*
    Laing, Lucy M.   *Relaxation Method.*
                             Aeronautical Quarterly, Vol. 19, 1968, pp. 375-387.

19. Greenspan, D.   *Discrete Numerical Methods in Physics and Engineering.*
                             Academic Press, 1974.

20. Brown, D.   *Information for Users of the National Research Council's 5-ft. × 5-ft. Blowdown Wind Tunnel at the National Aeronautical Establishment.* Second Edition, National Aeronautical Establishment, Laboratory Technical Report LTR-HA-6, National Research Council Canada, Ottawa, September 1972.

21. Mokry, M.
    Peake, D.J.
    Bowker, A.J.   *Wall Interference on Two-Dimensional Supercritical Airfoils, Using Wall Pressure Measurements to Determine the Porosity Factors for Tunnel Floor and Ceiling.* National Aeronautical Establishment, Aeronautical Report LR-575, National Research Council Canada, Ottawa, February 1974.

22. Garner, H.C.
    Rogers, E.W.E.
    Acum, W.E.A.
    Maskell, E.C.   *Subsonic Wind Tunnel Wall Corrections.* AGARDograph 109, October 1966.

23. Pindzola, M.
    Lo, C.-F.   *Boundary Interference at Subsonic Speeds in Wind Tunnels with Ventilated Walls.* AEDC-TR-69-47, Arnold Engineering Development Center, May 1969.

24. Ashley, H.
    Landahl, M.   *Aerodynamics of Wing and Bodies.* Addison-Wesley, 1965.

25. Galway, R.D.   *Wind Tunnel Tests of ONERA Aircraft Models.* National Research Council Canada, Ottawa, to be published.

26. Monnerie, B.
    Charpin, F.   *Essais de tremblement ("buffeting") d'une aile en flèche en transsonique.* L'Aéronautique et l'Astronautique, No. 50, 1975-1.

TABLE 1

PARAMETERS OF ONERA CALIBRATION MODELS

IN THE NAE 5-FT. × 5-FT. WIND TUNNEL

Model	b	b/B	S/A	D	Blockage Ratio
M5	38.66"	0.644	0.0569	4.89"	0.789%
M3	18.67"	0.311	0.0133	2.36"	0.184%
M1	11.29"	0.188	0.0048	1.43"	0.068%
sting				2.00"	0.087%

TABLE 2

NUMBER OF ITERATIONS FOR THE EXAMPLE IN SECTION 2.5, $\triangle x = \triangle y = \triangle z$

t	P	ω						
		1.5	1.3	1.1	0.9	0.7	0.5	0.3
0.0	0.000	40						
0.1	0.158	40						
0.2	0.325	40						
0.3	0.510	30						
0.4	0.727	30						
0.5	1.000	30						
0.6	1.376	div	div	50				
0.7	1.963	div	div	div	70			
0.8	3.078	div	div	div	div	div	110	
0.9	6.314	div	div	div	div	div	div	120

M5

M3

MI
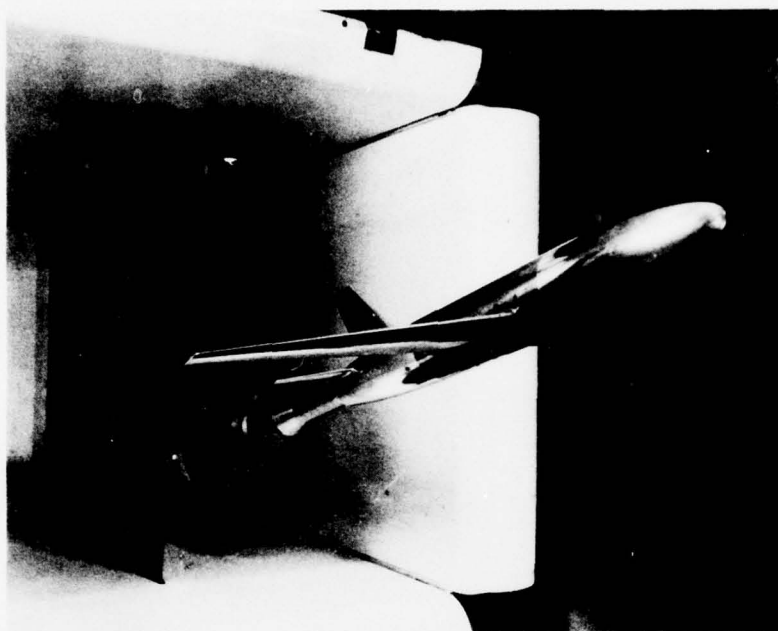
FIG. 1: ONERA MODELS MOUNTED IN THE NAE 5-FT. × 5-FT. WIND TUNNEL
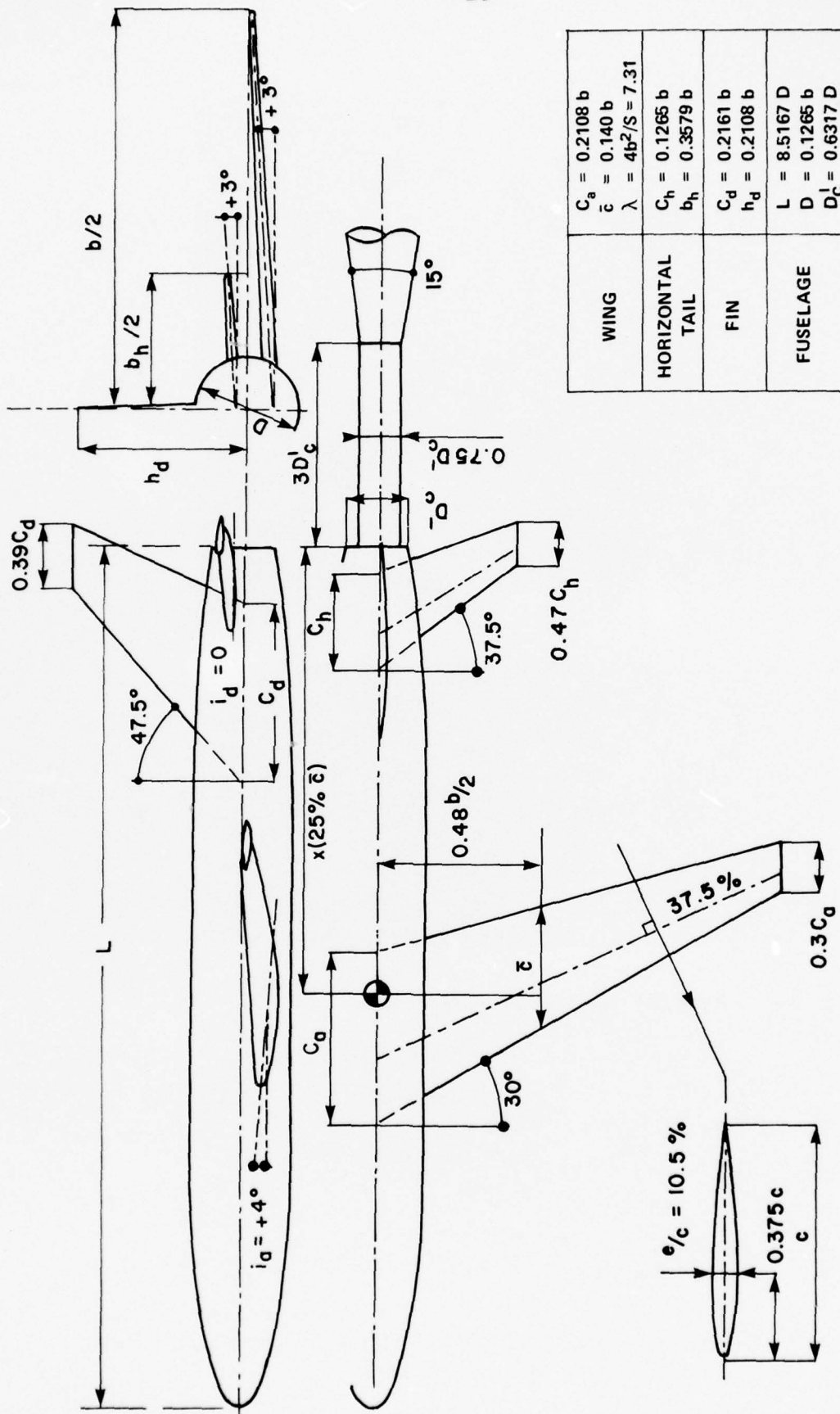
WING	C_a = 0.2108 b $\bar{c}$ = 0.140 b λ = $4b^2/S$ = 7.31
HORIZONTAL TAIL	C_h = 0.1265 b b_h = 0.3579 b
FIN	C_d = 0.2161 b h_d = 0.2108 b
FUSELAGE	L = 8.5167 D D = 0.1265 b D_c' = 0.6317 D

FIG. 2: GEOMETRY OF MODELS AND STINGS
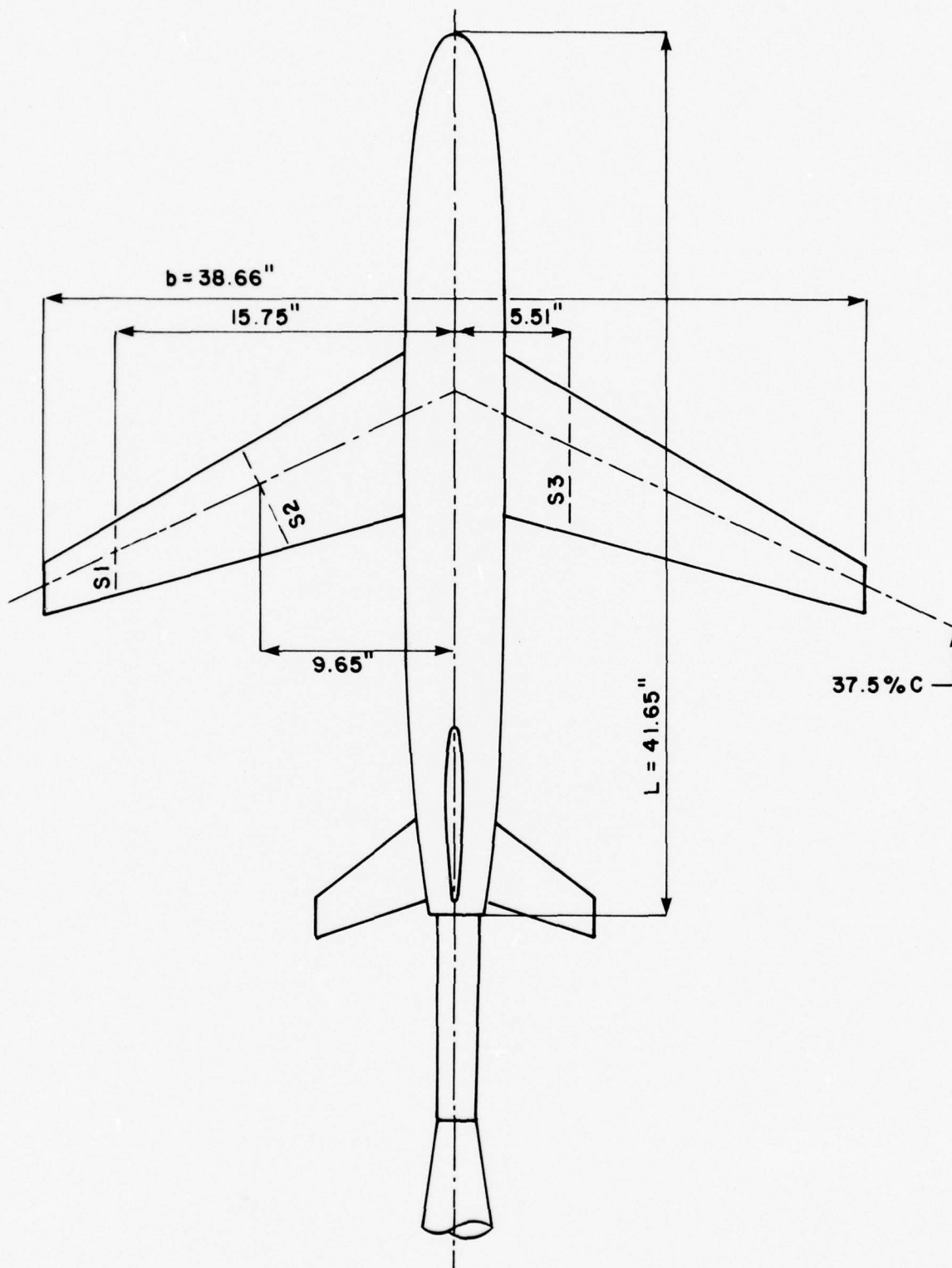
FIG. 3: WING PRESSURE ORIFICE LOCATIONS, MODEL M5

AIR STORAGE VESSELS (3)   FLEXIBLE COUPLING   SETTLING CHAMBER   FLEXIBLE NOZZLE   VARIABLE DIFFUSER   CONSTANT   EXHAUST
AND SHUT-OFF VALVE   AND CONTROL VALVE   AND   (FLEXIBLE PLATE WALLS)   AND   DIFFUSER   SILENCER
    FIXED CONTRACTION   MODEL SUPPORT
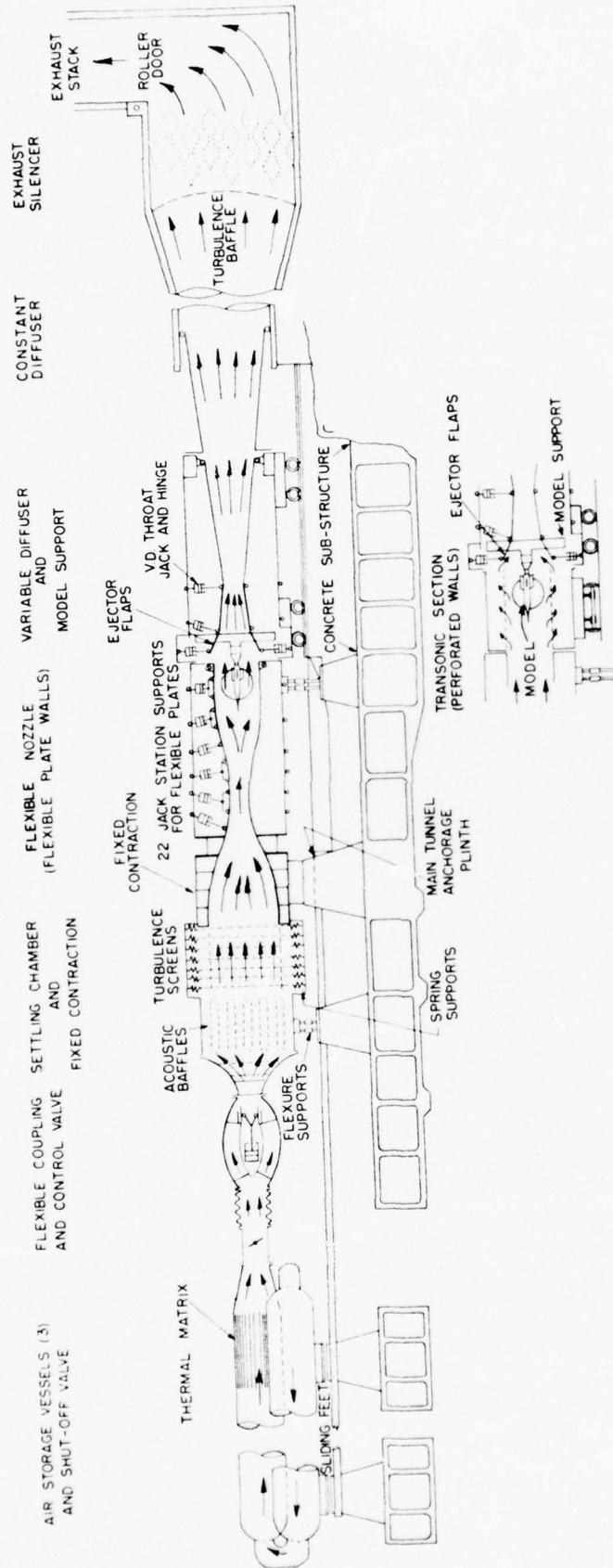
FIG. 4: SCHEMATIC OF THE NAE 5-FT. × 5-FT. TEST FACILITY

TUNNEL WALL

TUBES END FLUSH WITH HOLE

ELLIPTICAL PROFILE

$\frac{1}{2}$

$\frac{1}{2}$

2

6 : 1

$\frac{1}{8}$

0.031 D. 40 HOLES

$\frac{5}{8}$

2 BUNDLES OF 20 TUBES EACH

ALL TUBES 0.032 O.D. x 0.0062 WALL BONDED IN PLACE AND CAVITIES FILLED WITH EPOXY CEMENT ALTERNATE TUBES ON OPPOSITE SIDES OF RAIL

RAILS INSTALLED WITH 4 RETAINING NUTS

ALL DIMENSIONS ARE IN INCHES
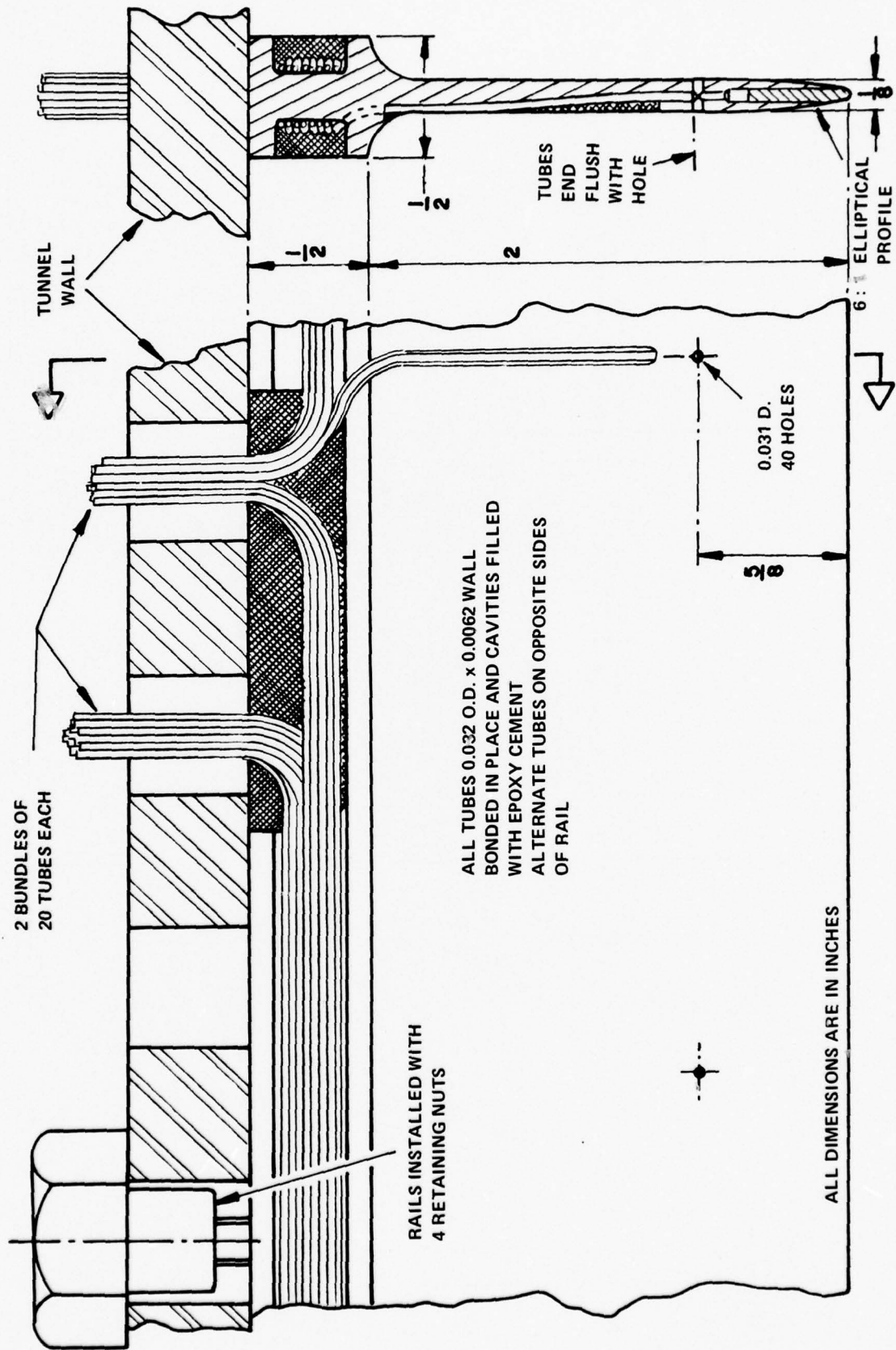
FIG. 5: DETAILS OF STATIC PRESSURE RAILS
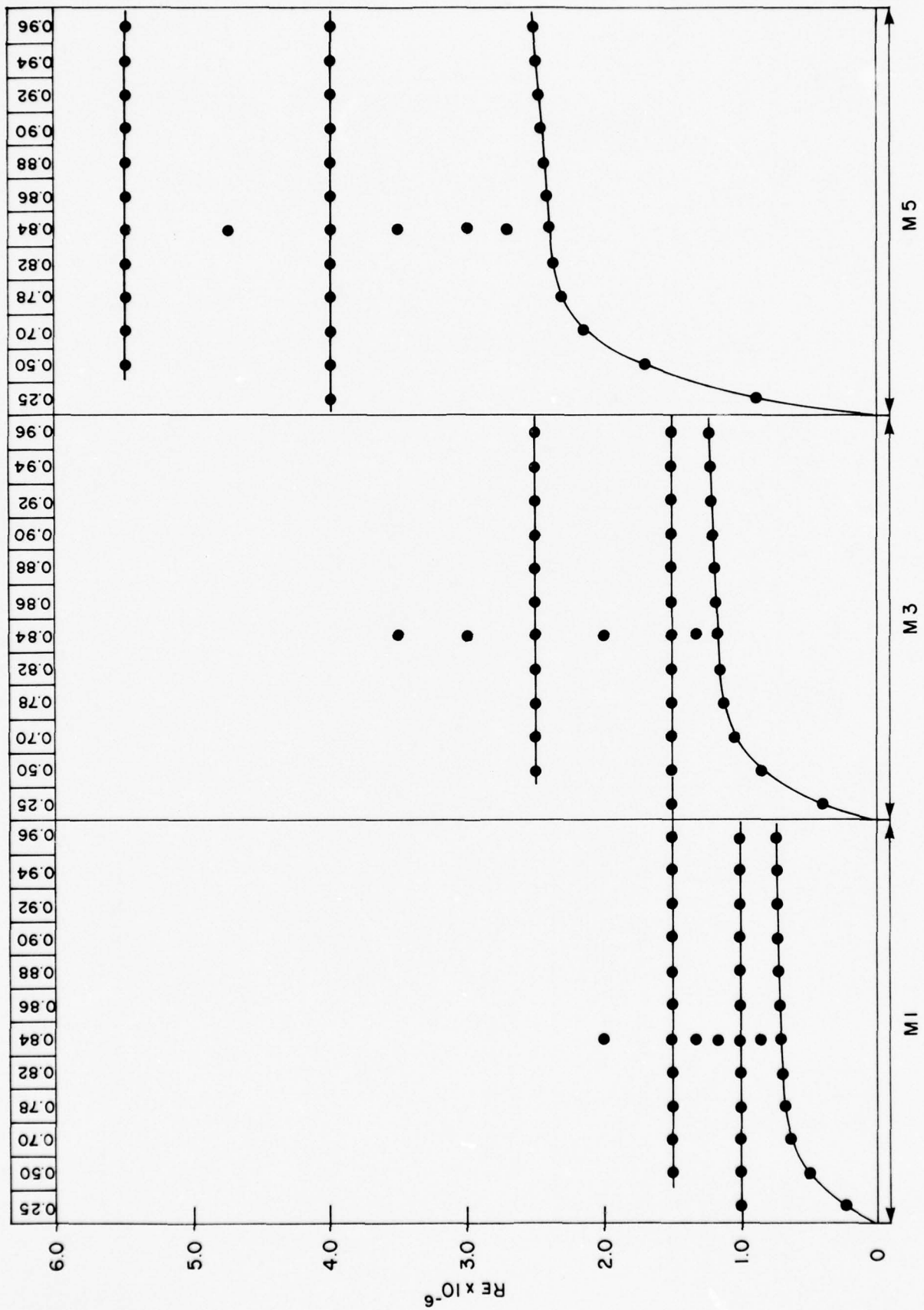
FIG. 6: SUMMARY OF TEST CONDITIONS
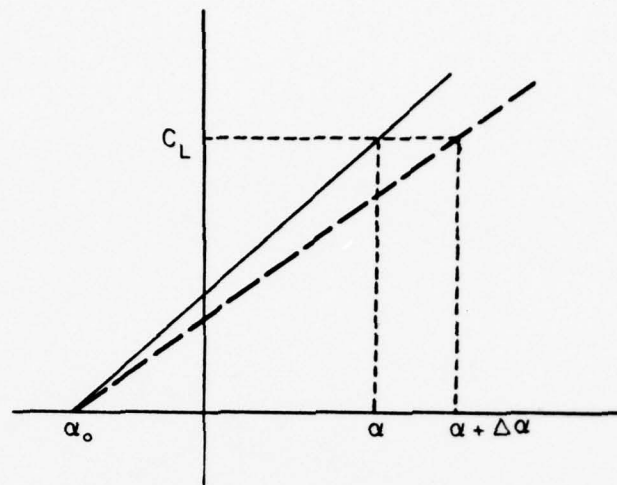
FIG. 7: ILLUSTRATING THE CORRECTION TO THE LIFT CURVE SLOPE
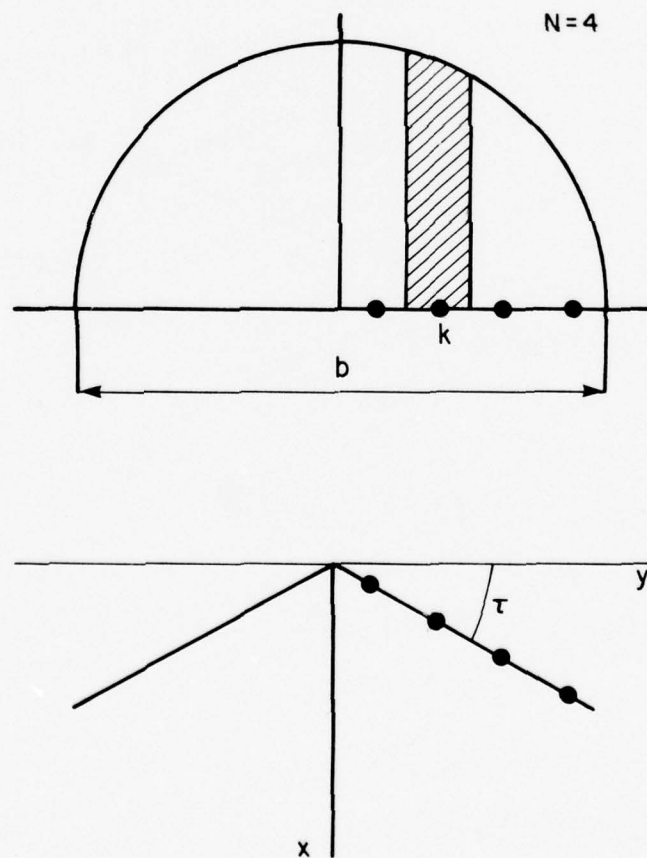
FIG. 8: REPRESENTATION OF A SWEPT WING
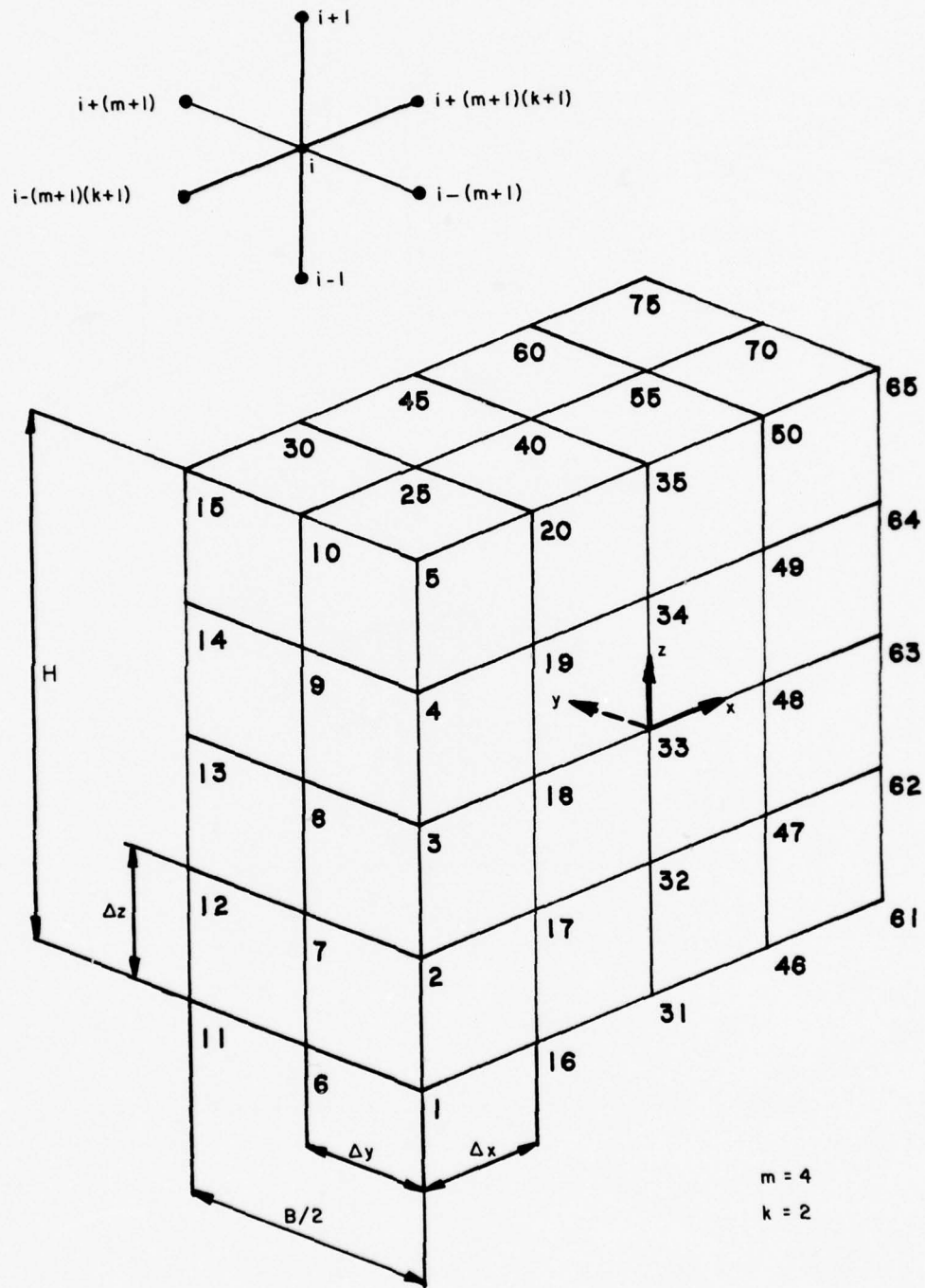
FIG. 9: COMPUTATIONAL GRID
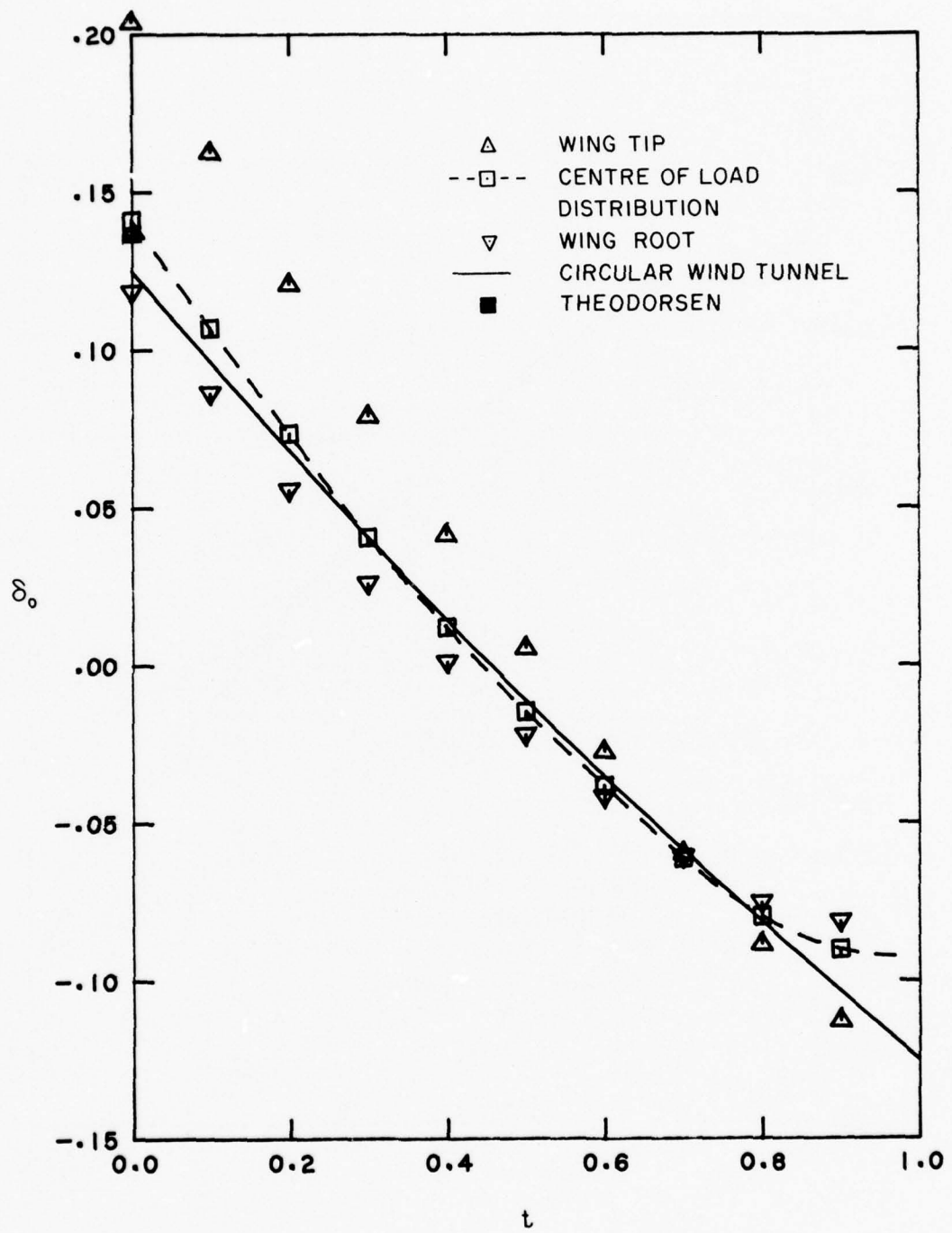
FIG. 10(a): UPWASH FACTOR
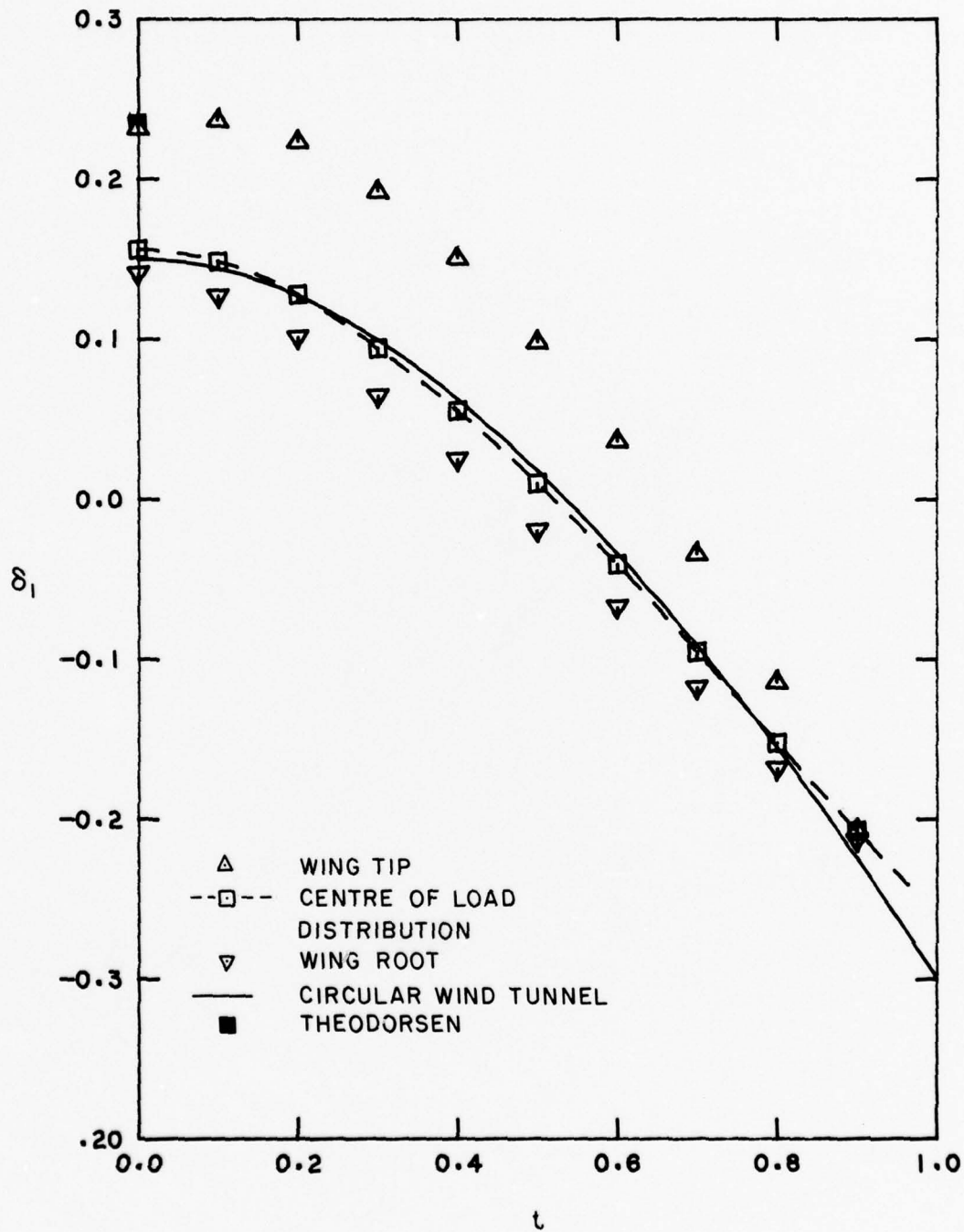
FIG. 10(b): STREAMLINE CURVATURE FACTOR
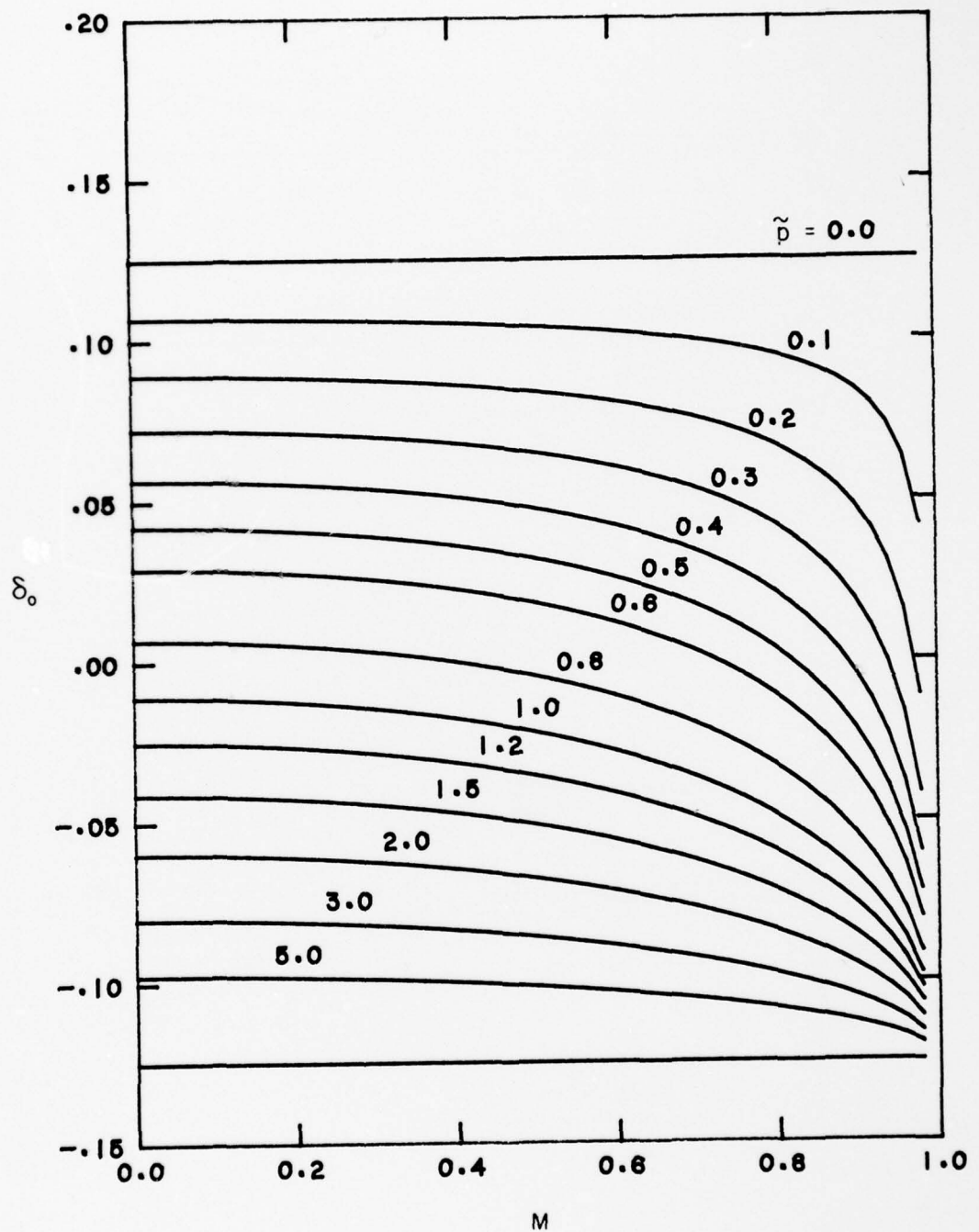
FIG. 11: UPWASH FACTOR FOR A CIRCULAR WIND TUNNEL AS A
FUNCTION OF MACH NUMBER
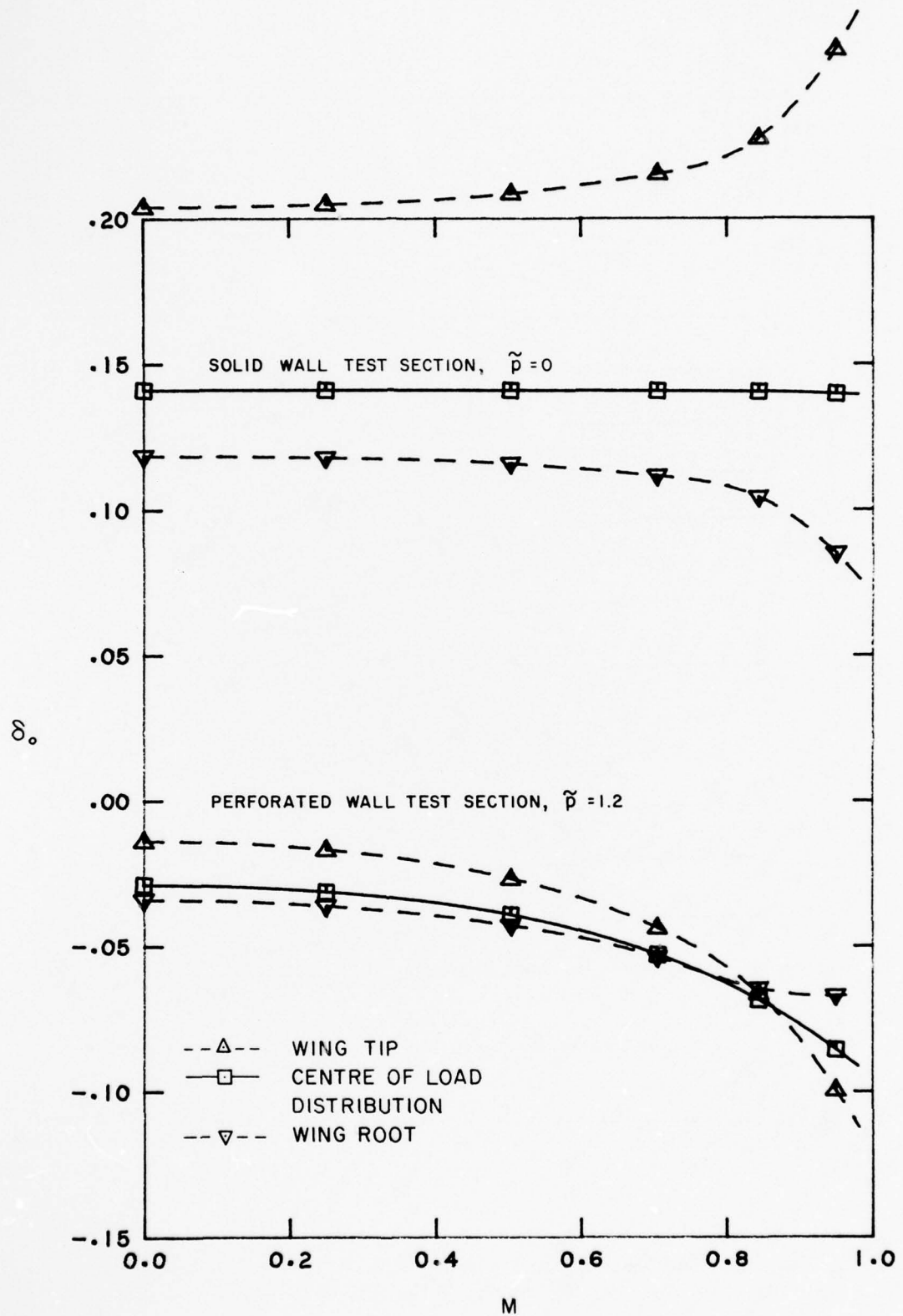
FIG. 12: UPWASH FACTOR AS A FUNCTION OF MACH NUMBER,
NAE 5-FT. × 5-FT. WIND TUNNEL, MODEL M5
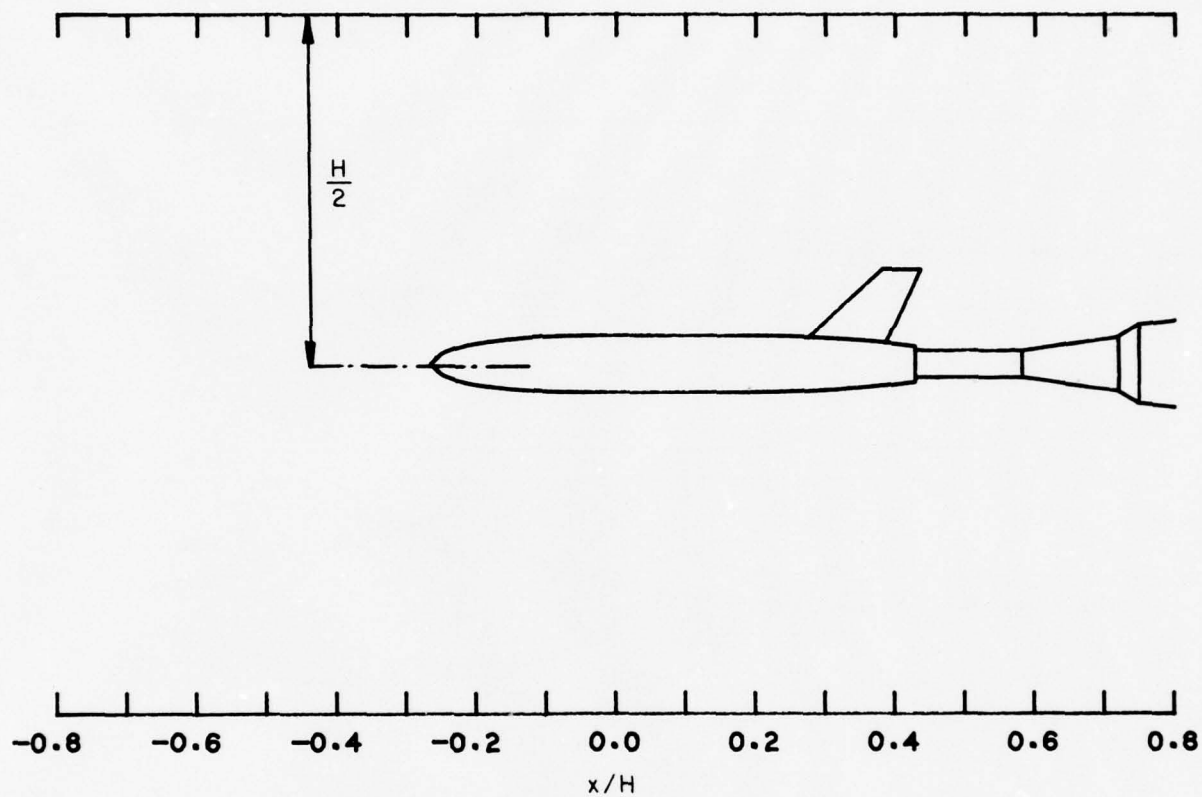
FIG. 13: LOCATION OF THE M5 MODEL WITH RESPECT TO TOP AND BOTTOM WALLS
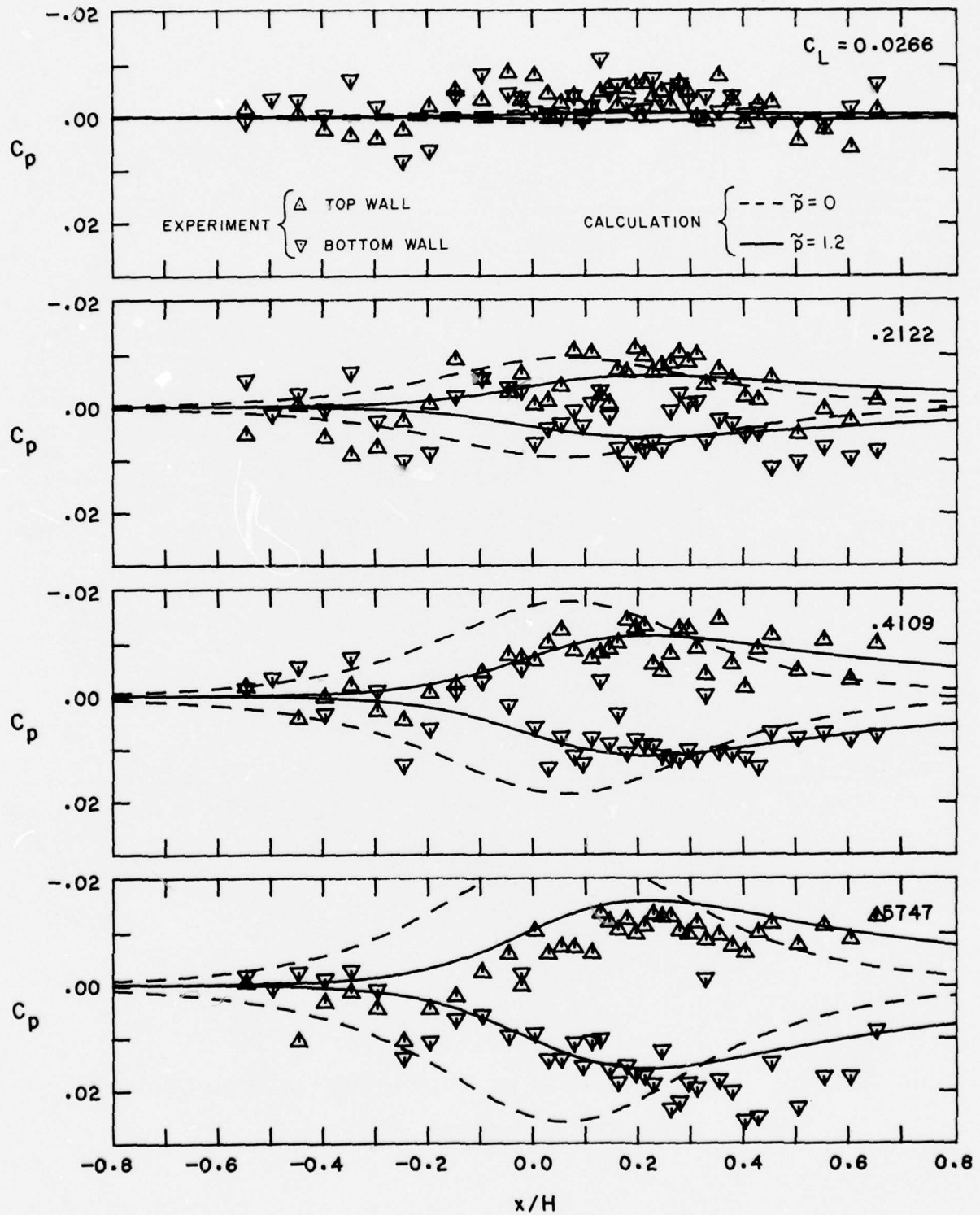
FIG. 14(a): MEASURED AND CALCULATED WALL PRESSURE DISTRIBUTIONS, MODEL M5, Re = 4.1 × 10^6, M = 0.705 ($C_p^* = -0.759$)
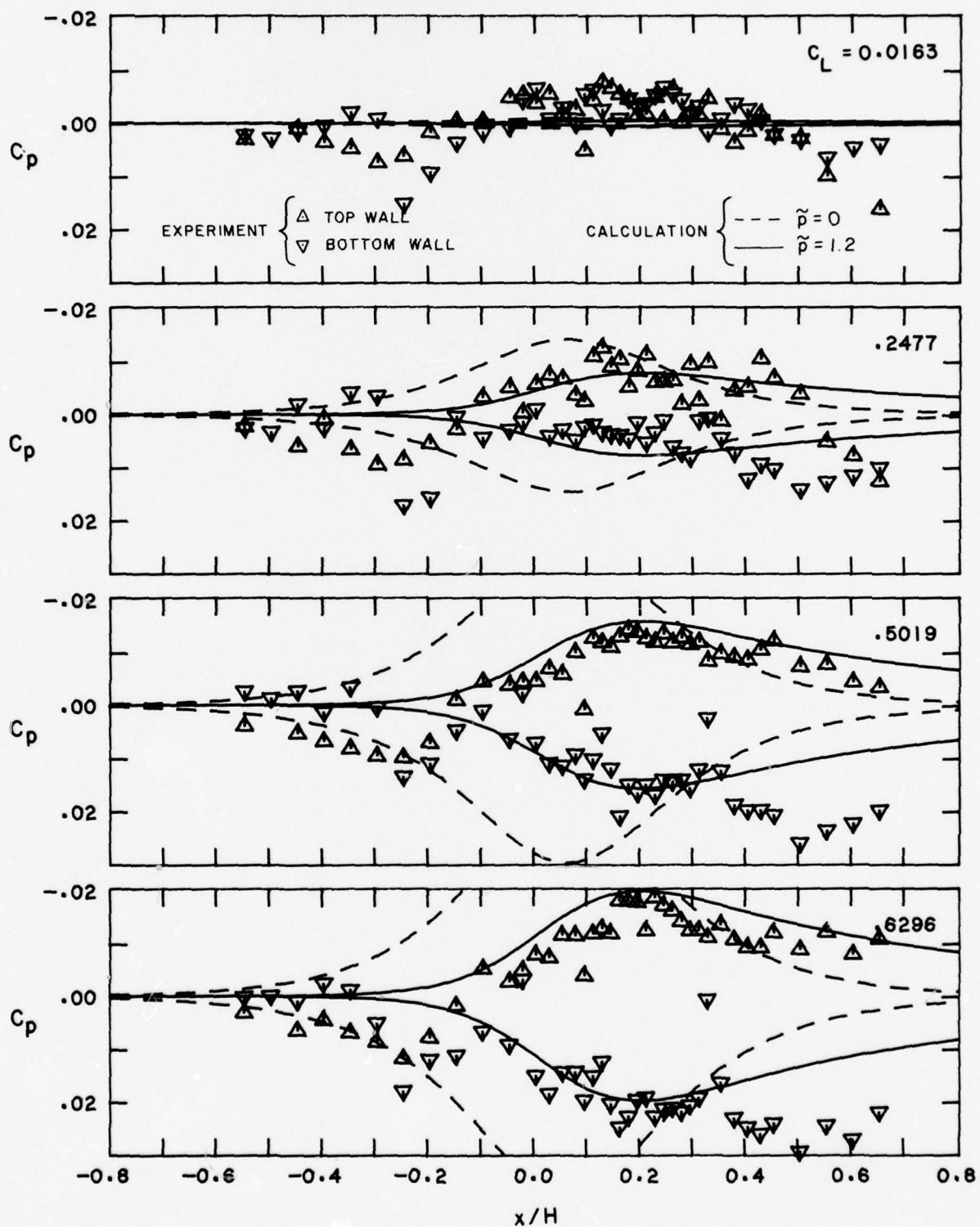
FIG. 14(b): MEASURED AND CALCULATED WALL PRESSURE DISTRIBUTIONS, MODEL M5, Re = 4.1 × 10⁶, M = 0.840 ($C_p^* = -0.327$)
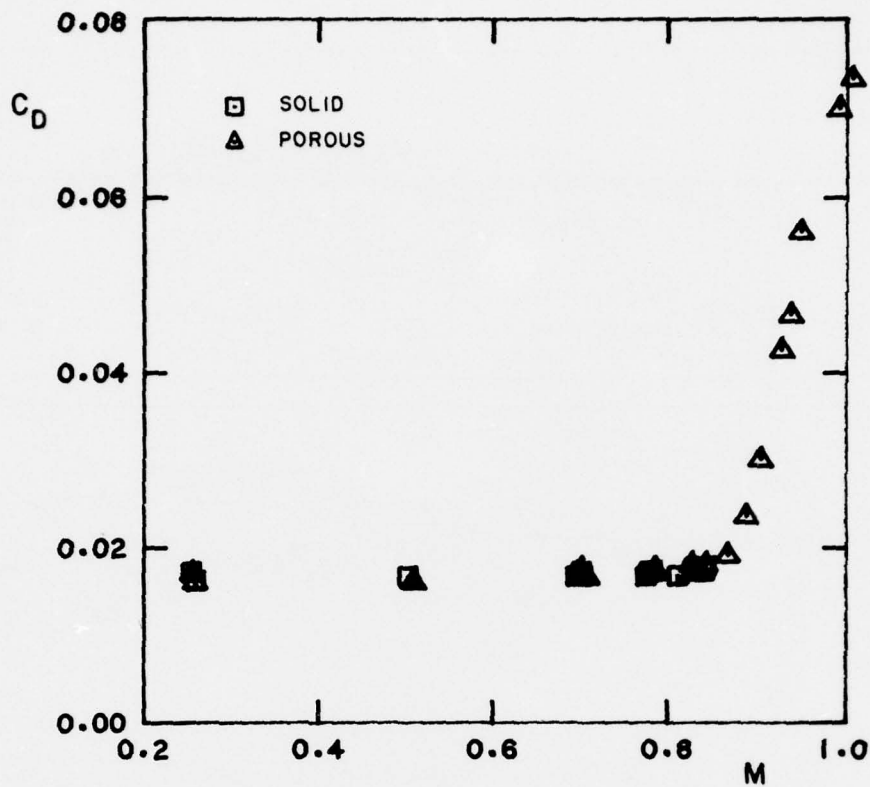
FIG. 15(a): DRAG vs. MACH NUMBER, MODEL M5, Re = 4.1 $\times$ 10^6, C_L = 0
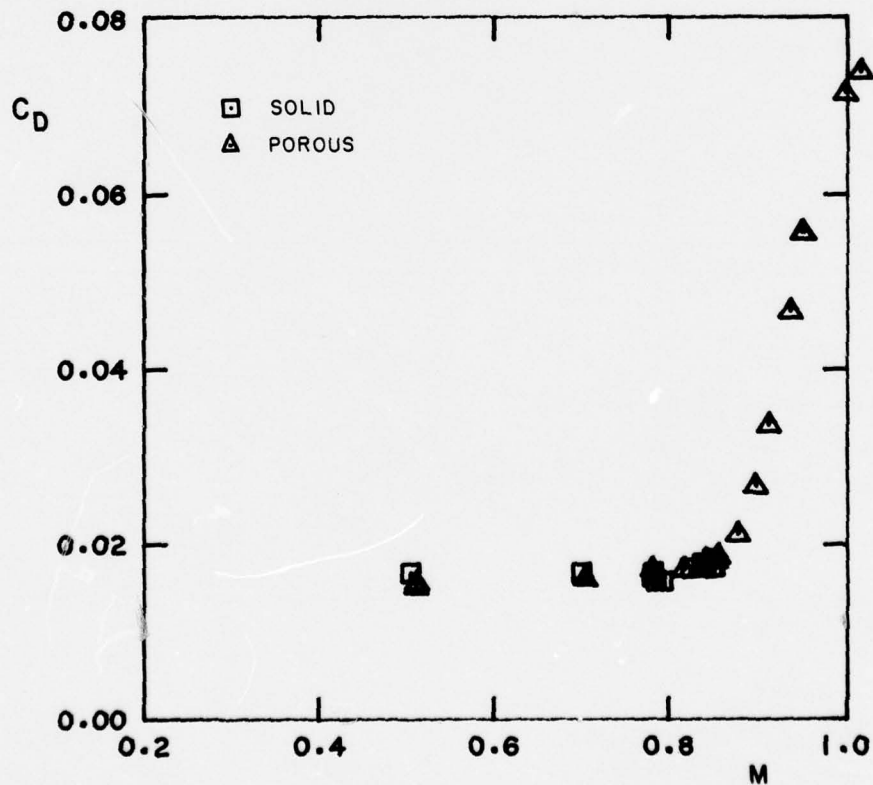
FIG. 15(b): DRAG vs. MACH NUMBER, MODEL M5, Re = 5.6 $\times$ 10^6, C_L = 0
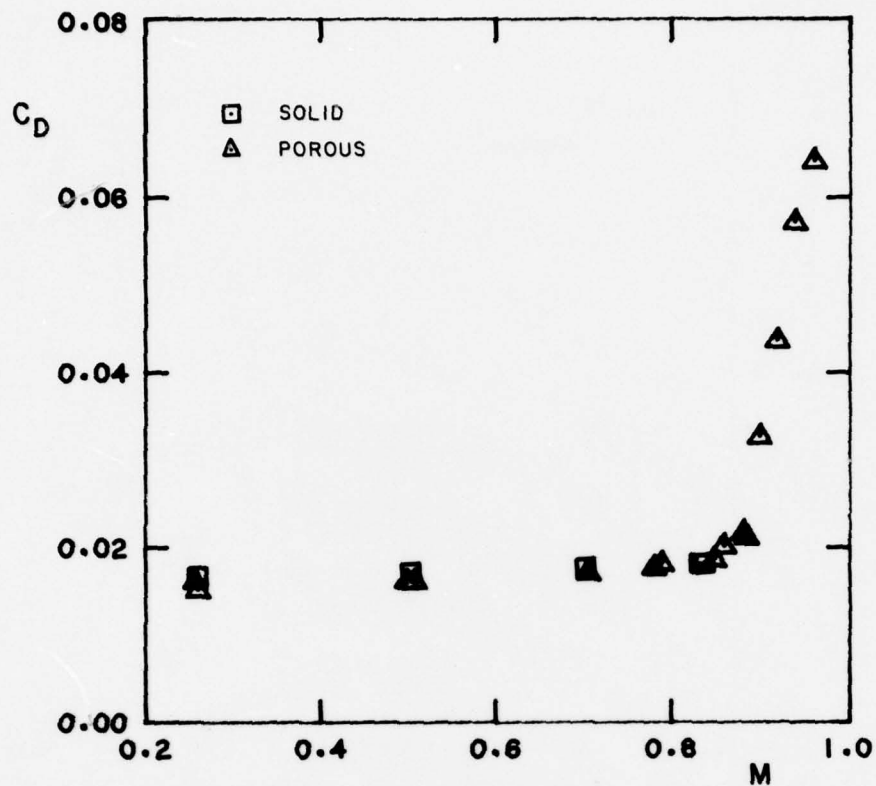
FIG. 15(c): DRAG vs. MACH NUMBER, MODEL M3, Re = 1.5 × 10^6, C$_L$ = 0
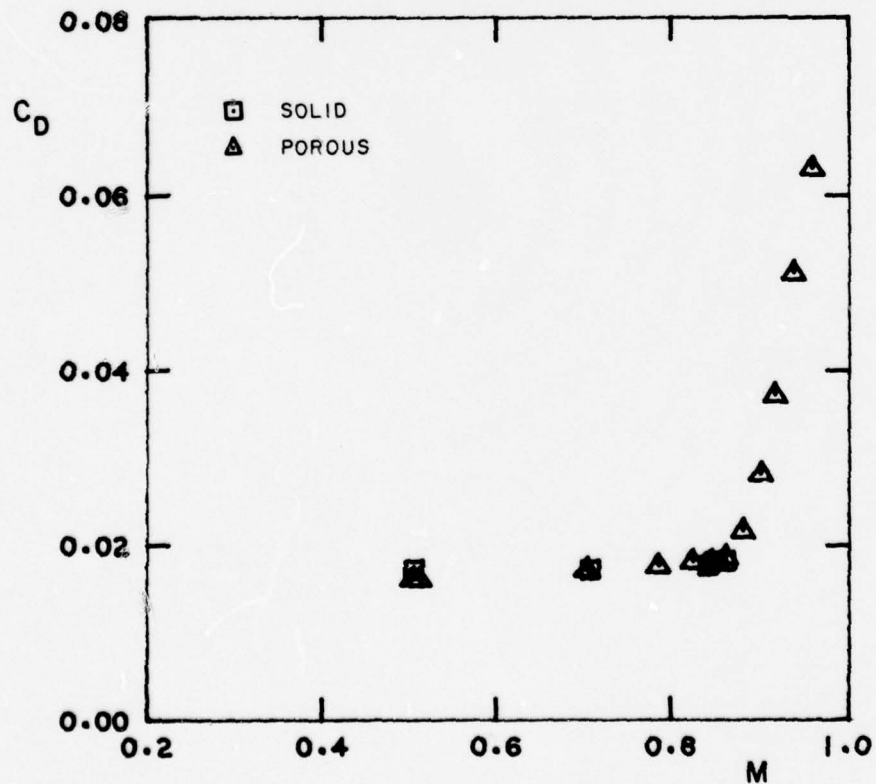
FIG. 15(d): DRAG vs. MACH NUMBER, MODEL M3, Re = 2.5 × 10^6, C$_L$ = 0
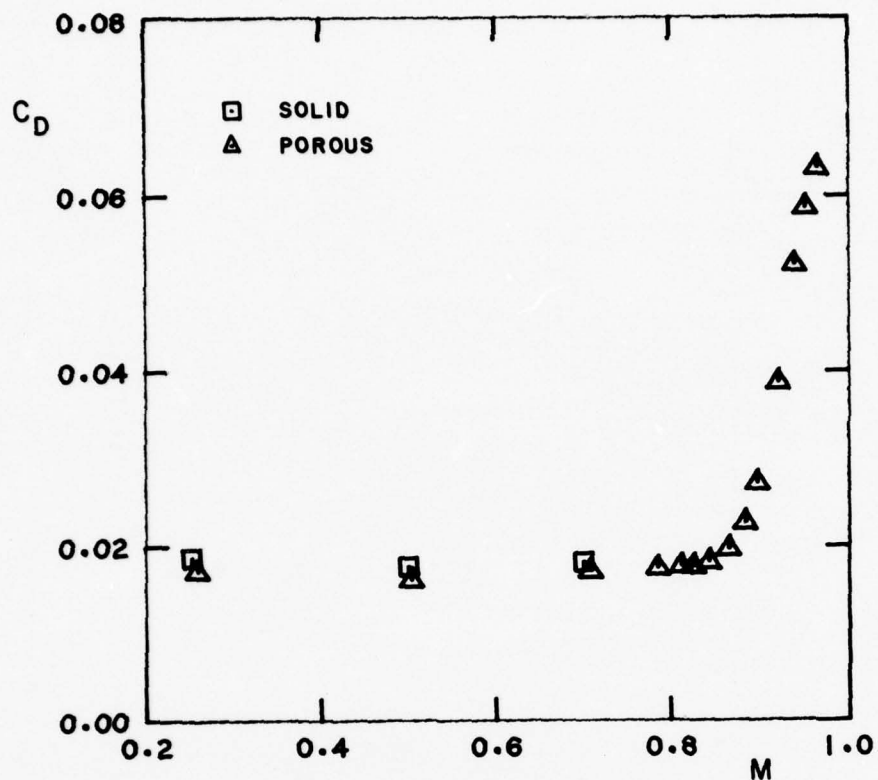
FIG. 15(e): DRAG vs. MACH NUMBER, MODEL M1, Re = 1.0×10^6, $C_L = 0$
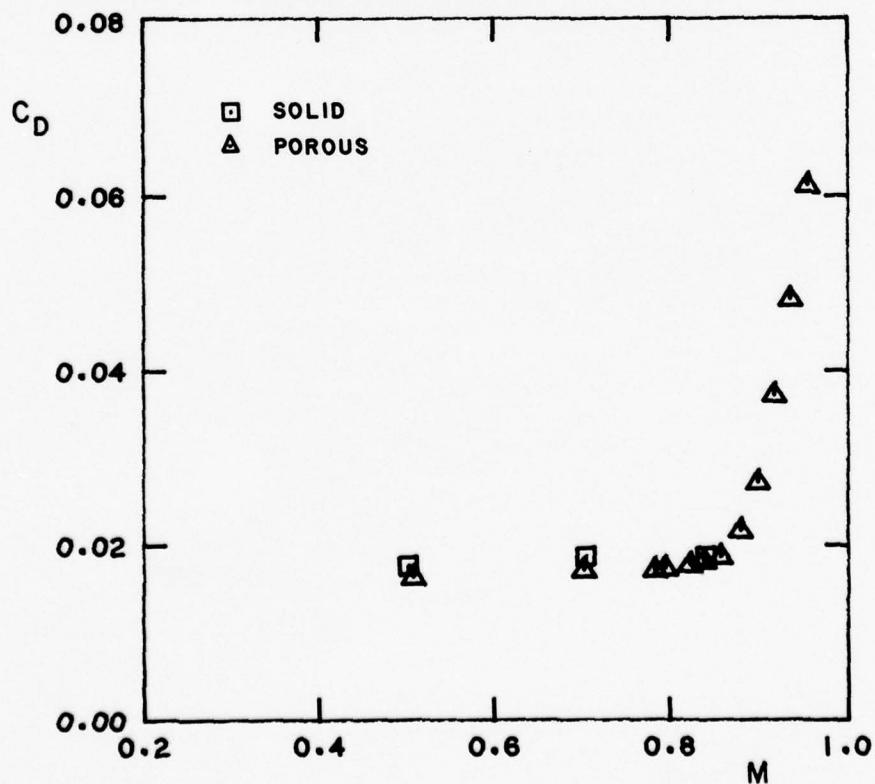
FIG. 15(f): DRAG vs. MACH NUMBER, MODEL M1, Re = 1.5×10^6, $C_L = 0$
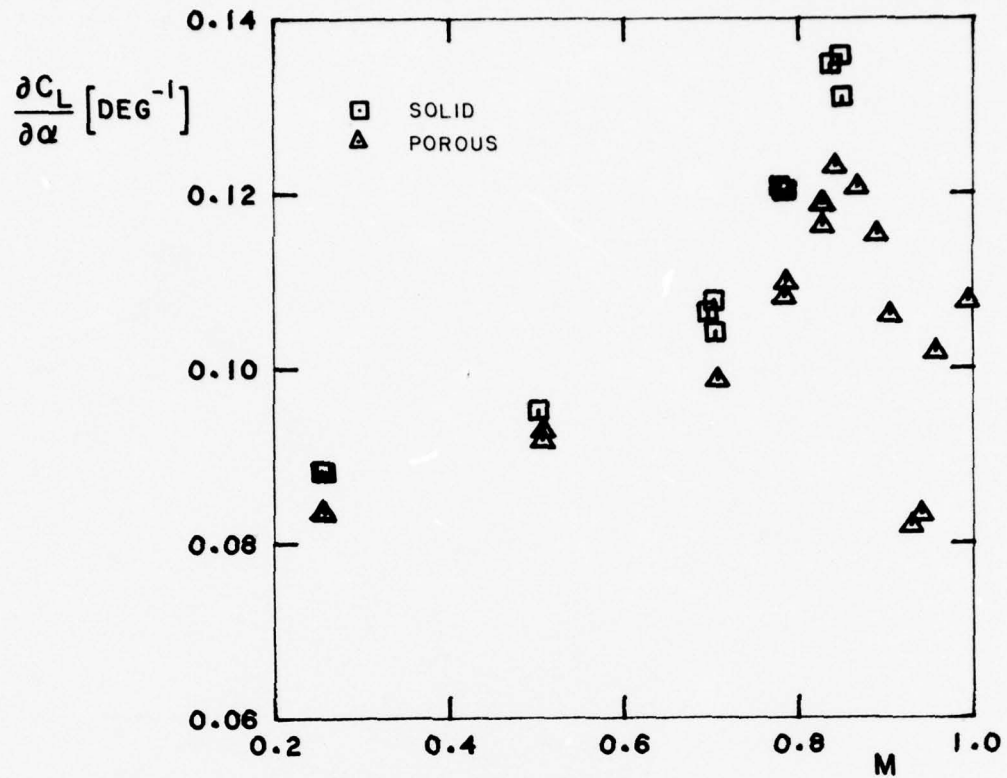
FIG. 16(a): LIFT FORCE SLOPE vs. MACH NUMBER, MODEL M5, Re = 4.1 × 10⁶
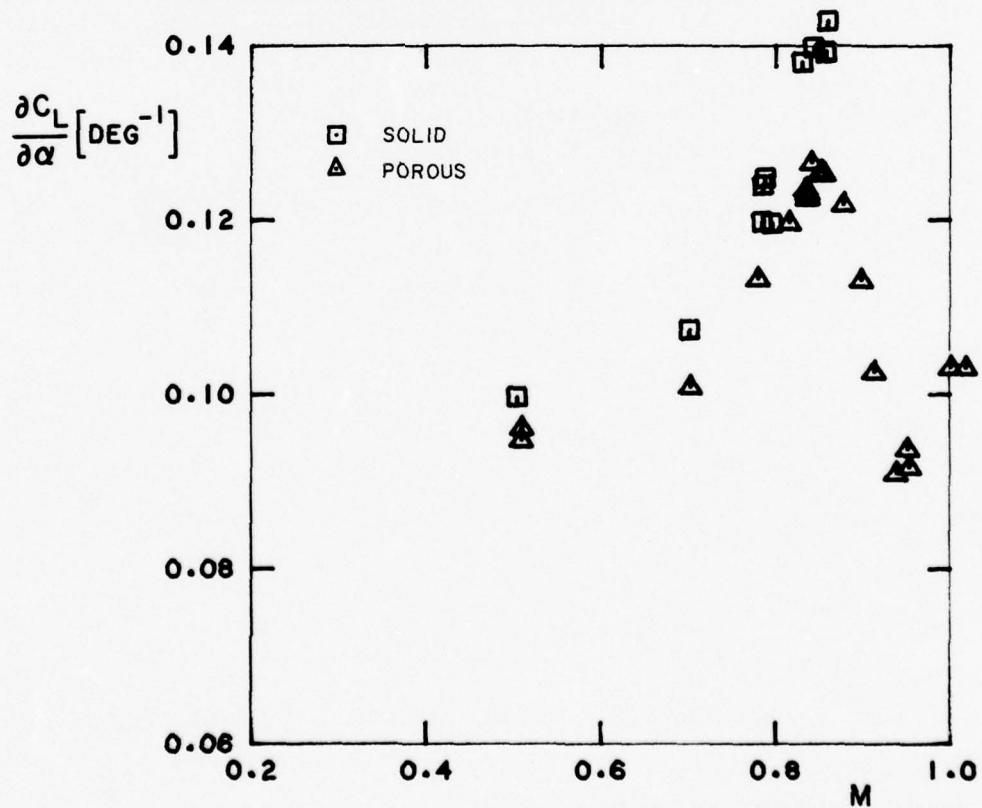
FIG. 16(b): LIFT FORCE SLOPE vs. MACH NUMBER, MODEL M5, Re = 5.6 × 10⁶
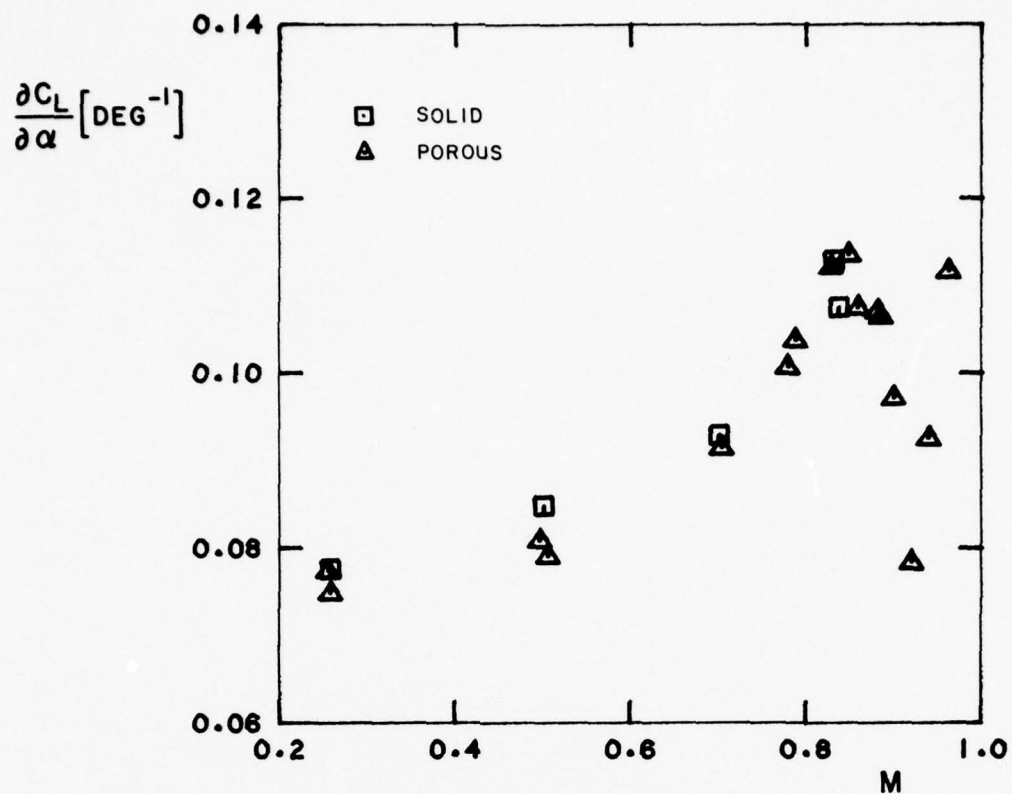
FIG. 16(c): LIFT FORCE SLOPE vs. MACH NUMBER, MODEL M3, Re = 1.5 × 10⁶
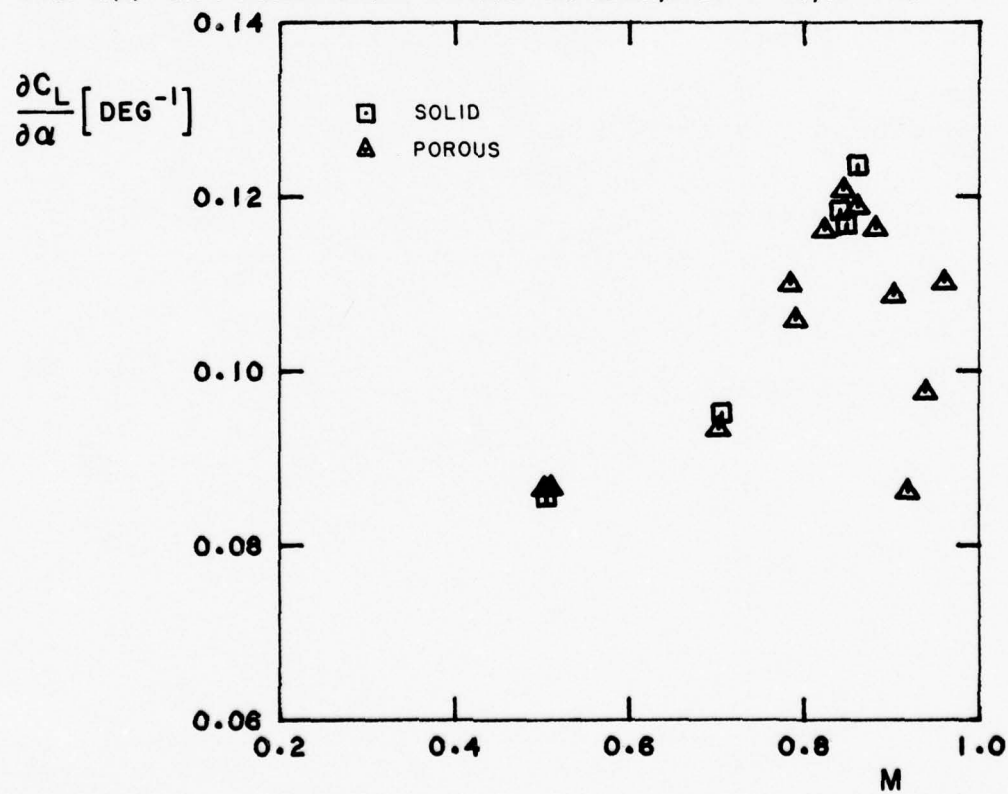
FIG. 16(d): LIFT FORCE SLOPE vs. MACH NUMBER, MODEL M3, Re = 2.5 × 10⁶

- 43 -
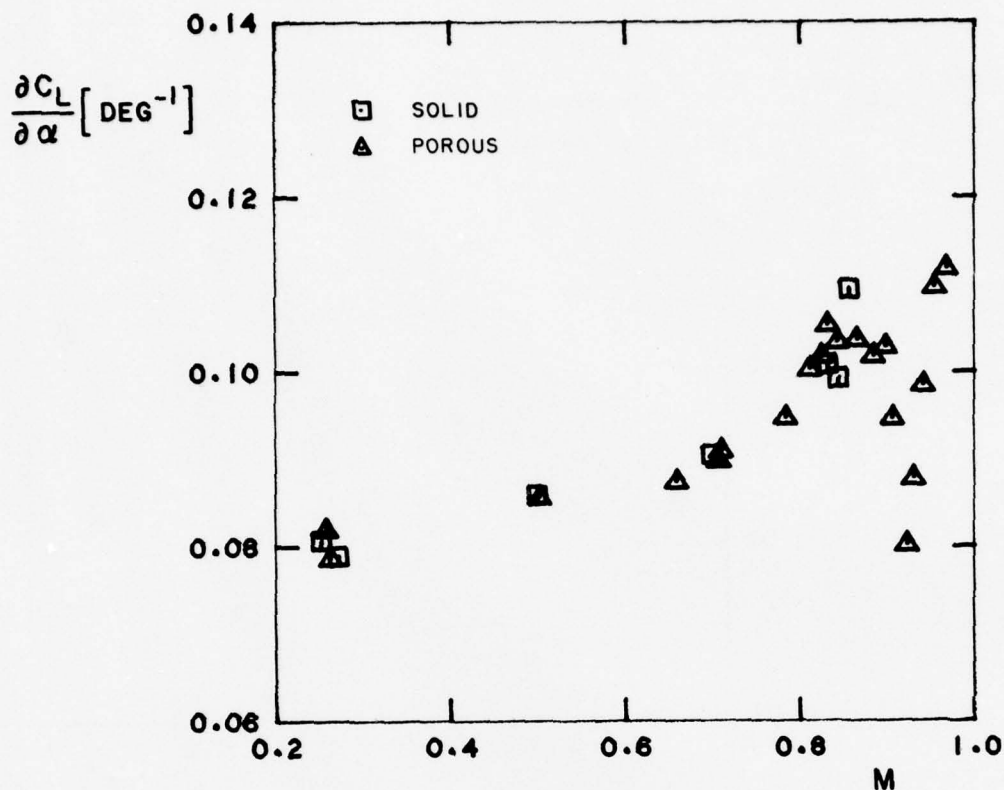
FIG. 16(e): LIFT FORCE SLOPE vs. MACH NUMBER, MODEL M1, Re = 1.0 × 10⁶
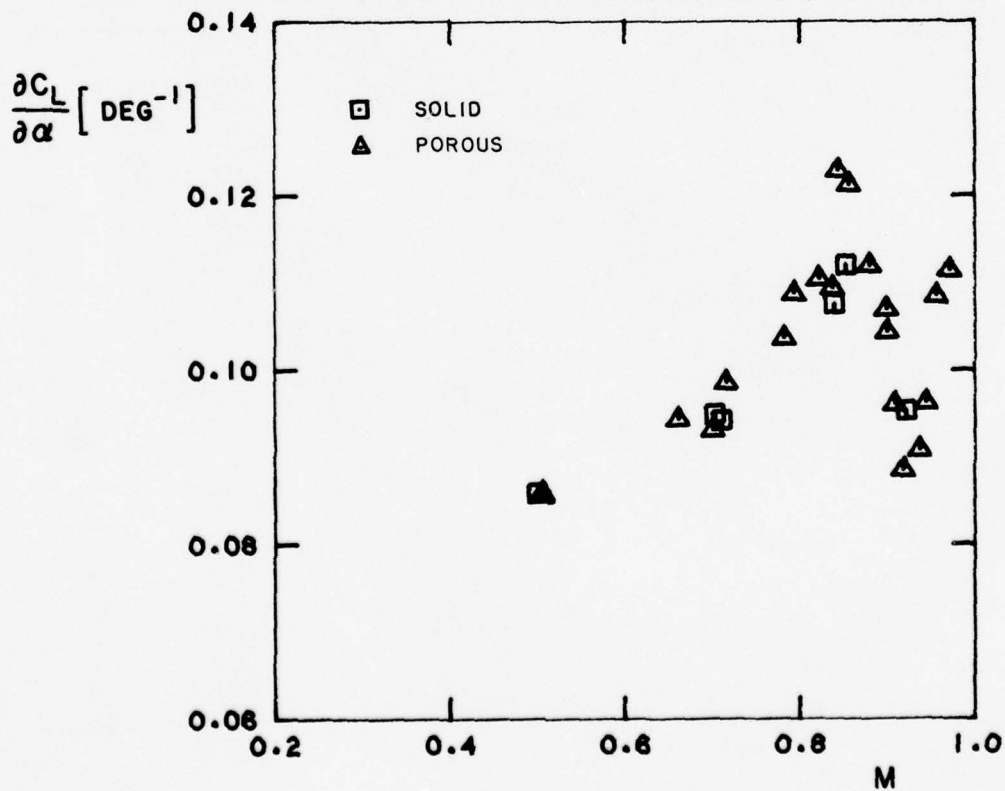
FIG. 16(f): LIFT FORCE SLOPE vs. MACH NUMBER, MODEL M1, Re = 1.5 × 10⁶
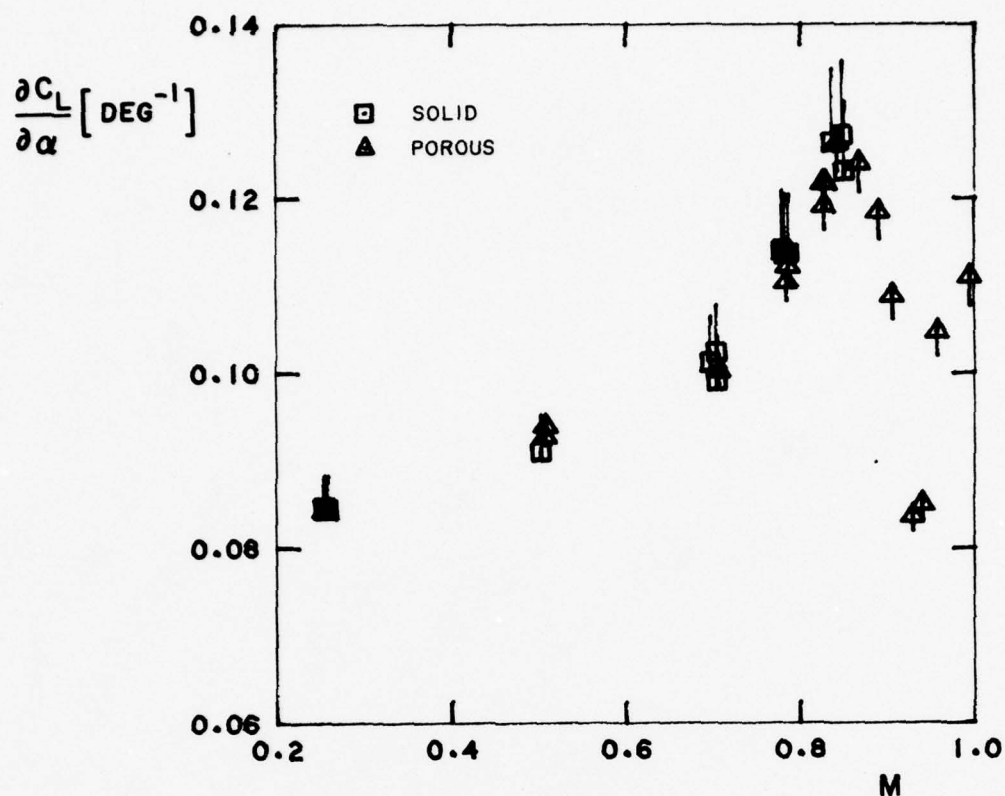
FIG. 17(a): CORRECTED LIFT FORCE SLOPE vs. MACH NUMBER, MODEL M5, Re = 4.1 × 10⁶
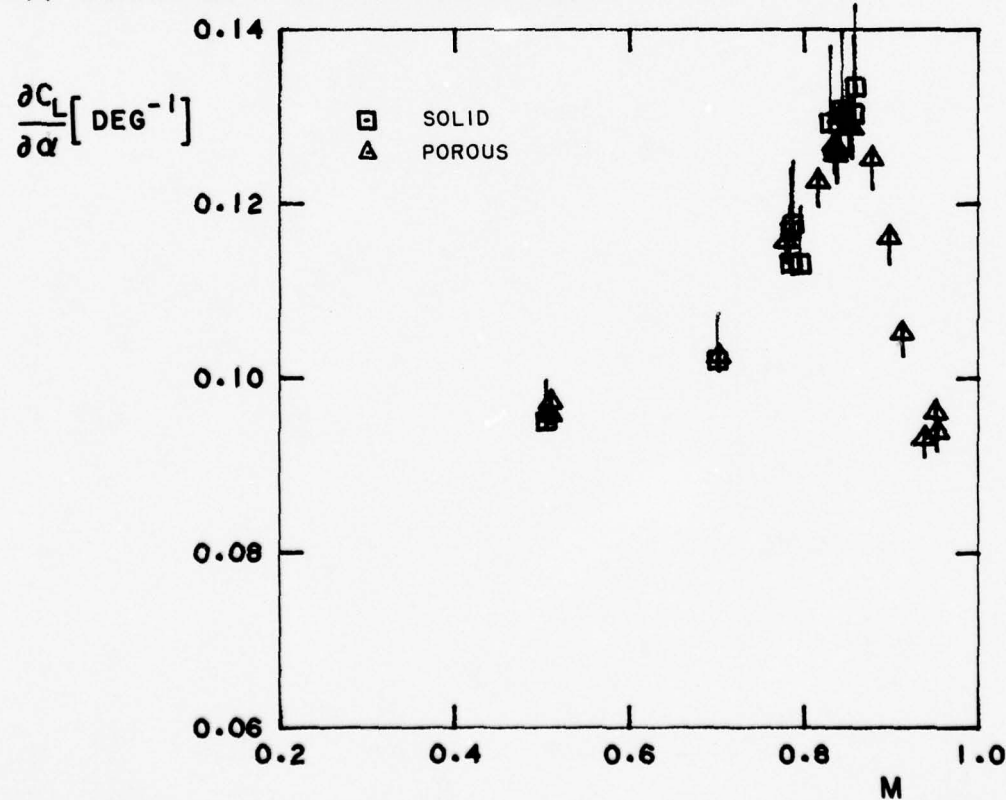
FIG. 17(b): CORRECTED LIFT FORCE SLOPE vs. MACH NUMBER, MODEL M5, Re = 5.6 × 10⁶
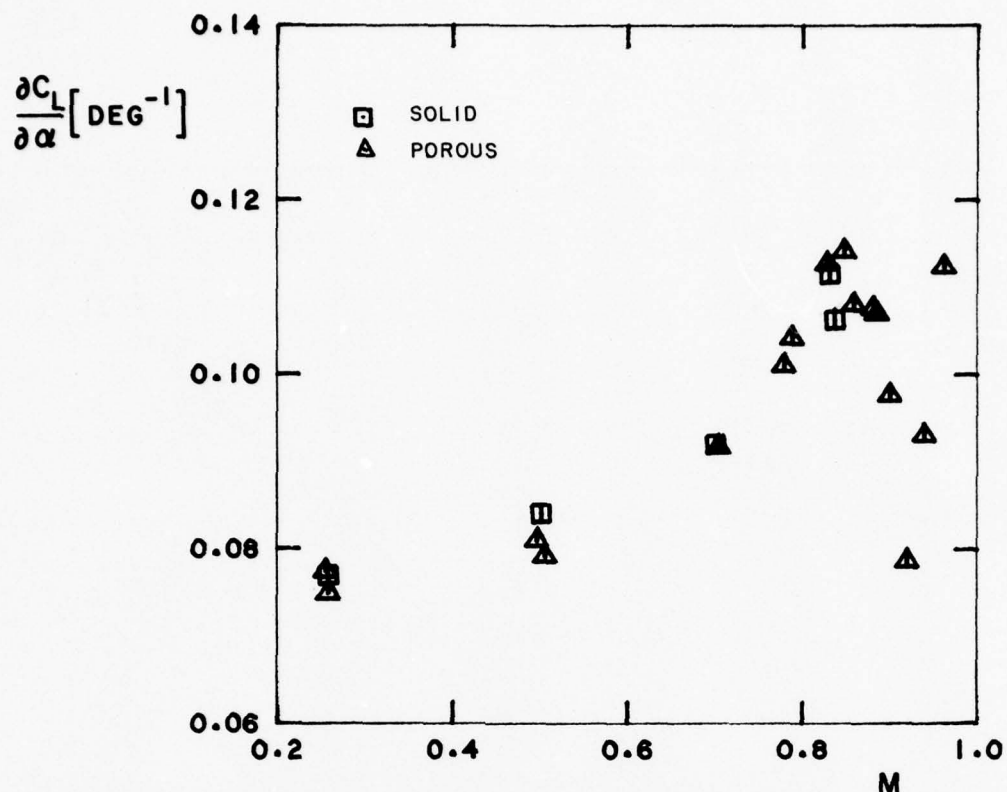
FIG. 17(c): CORRECTED LIFT FORCE SLOPE vs. MACH NUMBER, MODEL M3, Re = 1.5 × 10⁶
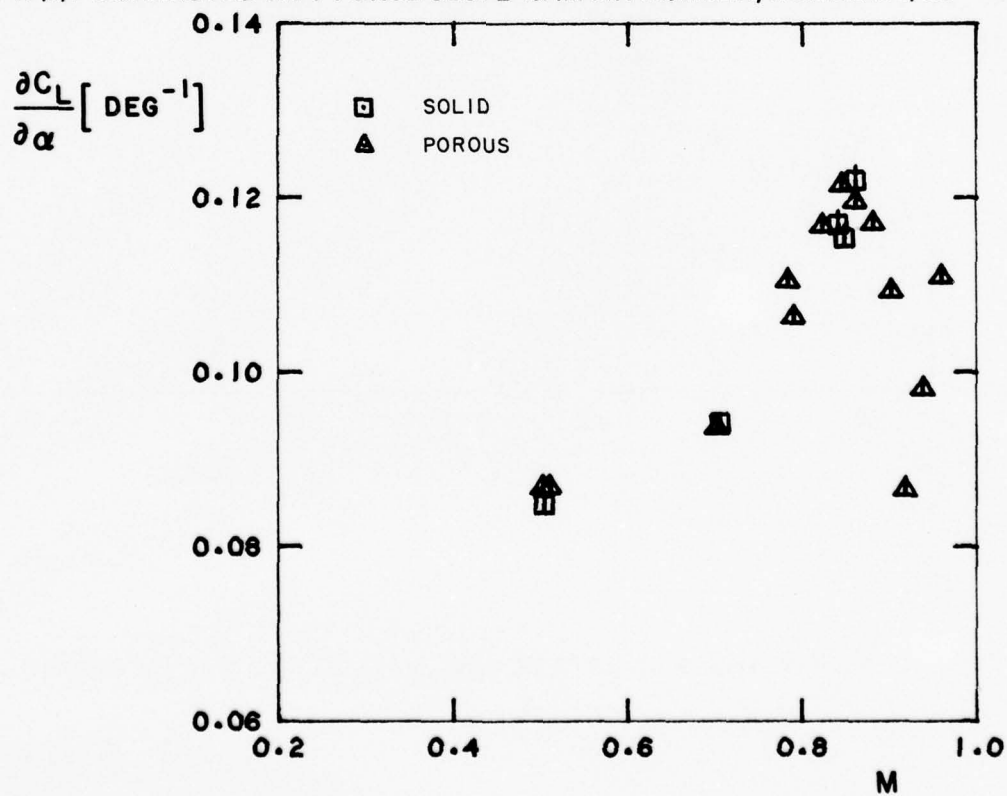
FIG. 17(d): CORRECTED LIFT FORCE SLOPE vs. MACH NUMBER, MODEL M3, Re = 2.5 × 10⁶
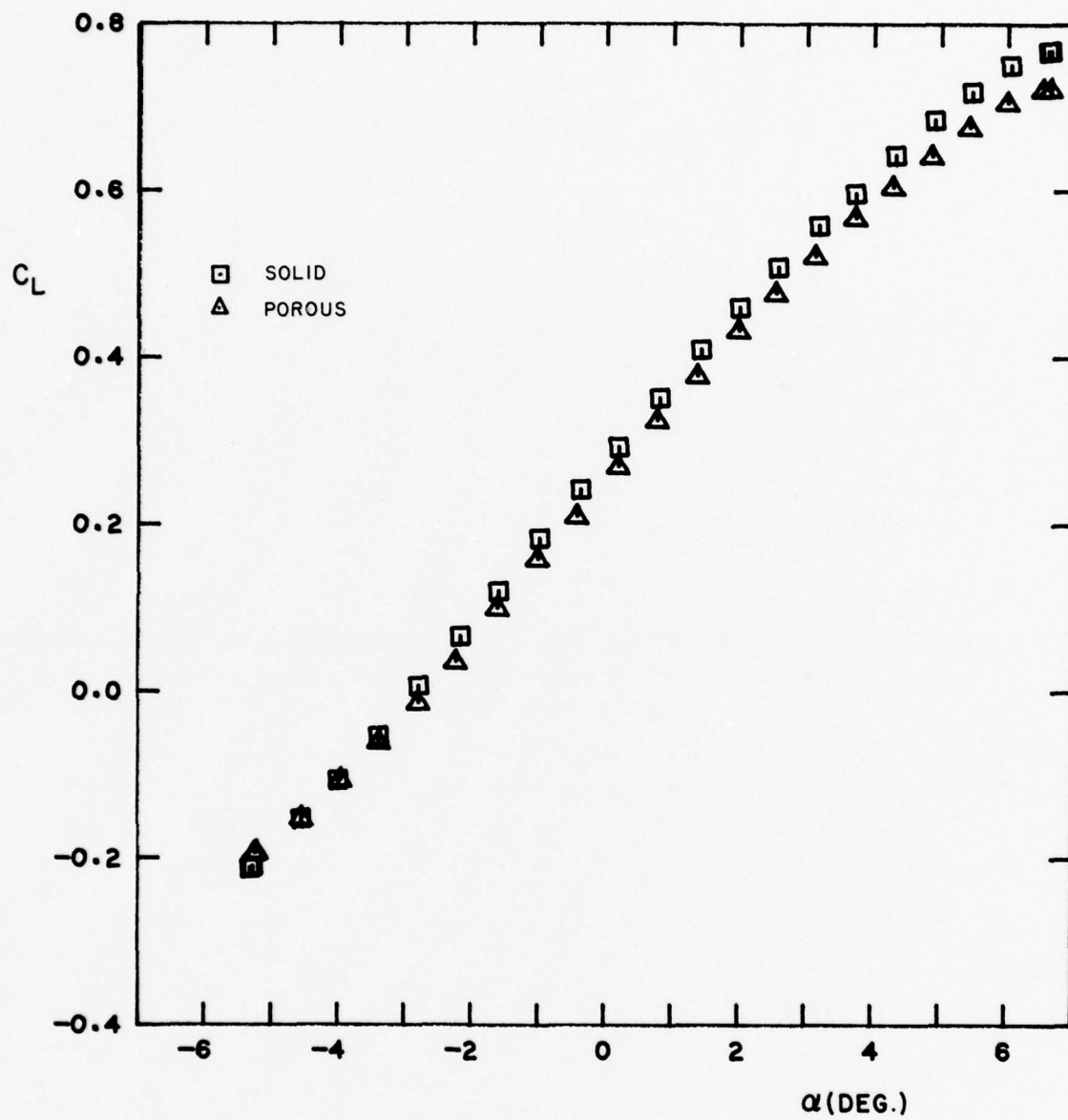
FIG. 18: LIFT vs. ANGLE OF ATTACK, MODEL M5, Re = 4.1 × 10⁶, M = 0.505
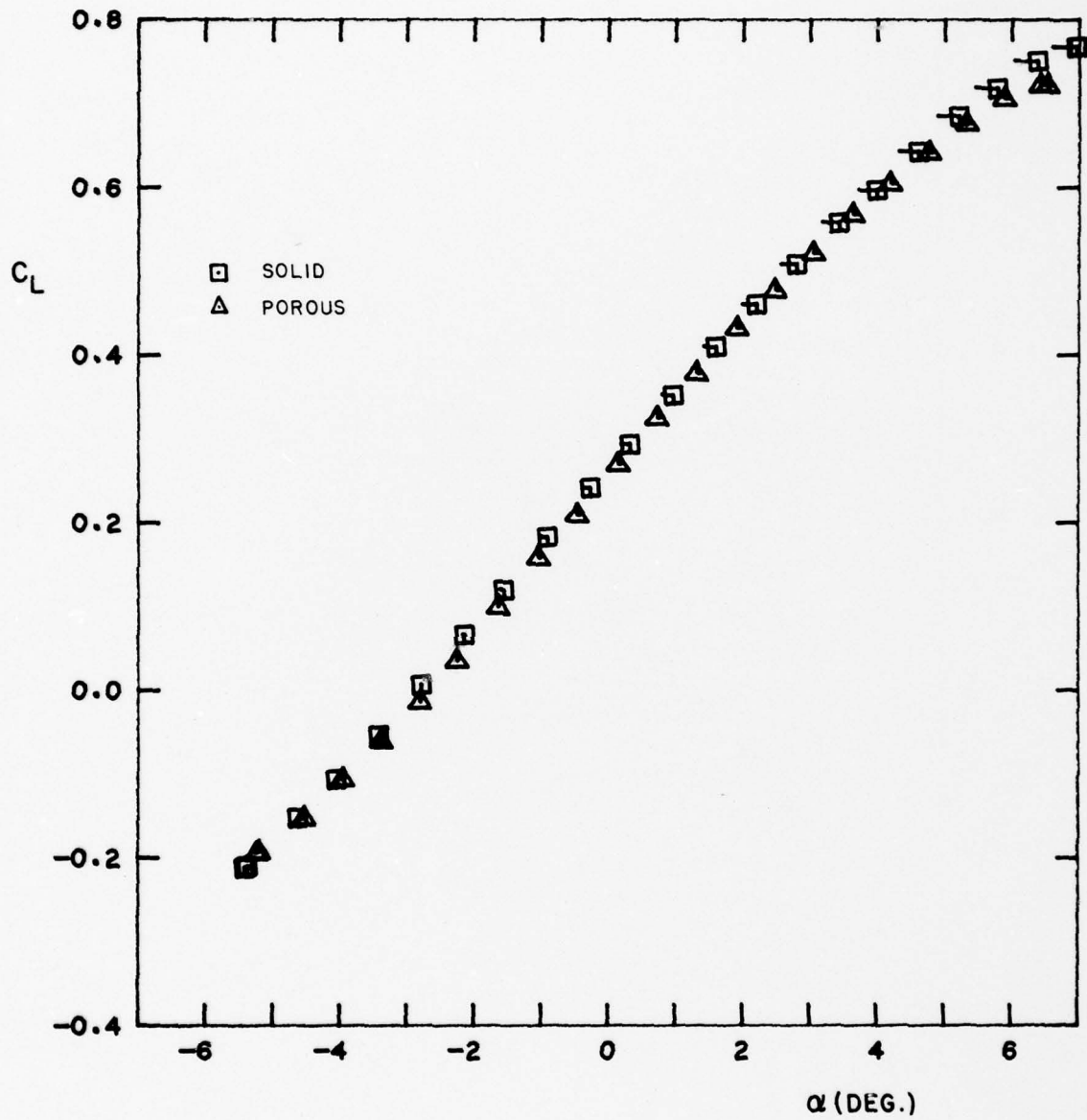
FIG. 19(a): LIFT vs. CORRECTED ANGLE OF ATTACK, MODEL M5, Re = 4.1 × 10^6, M = 0.505
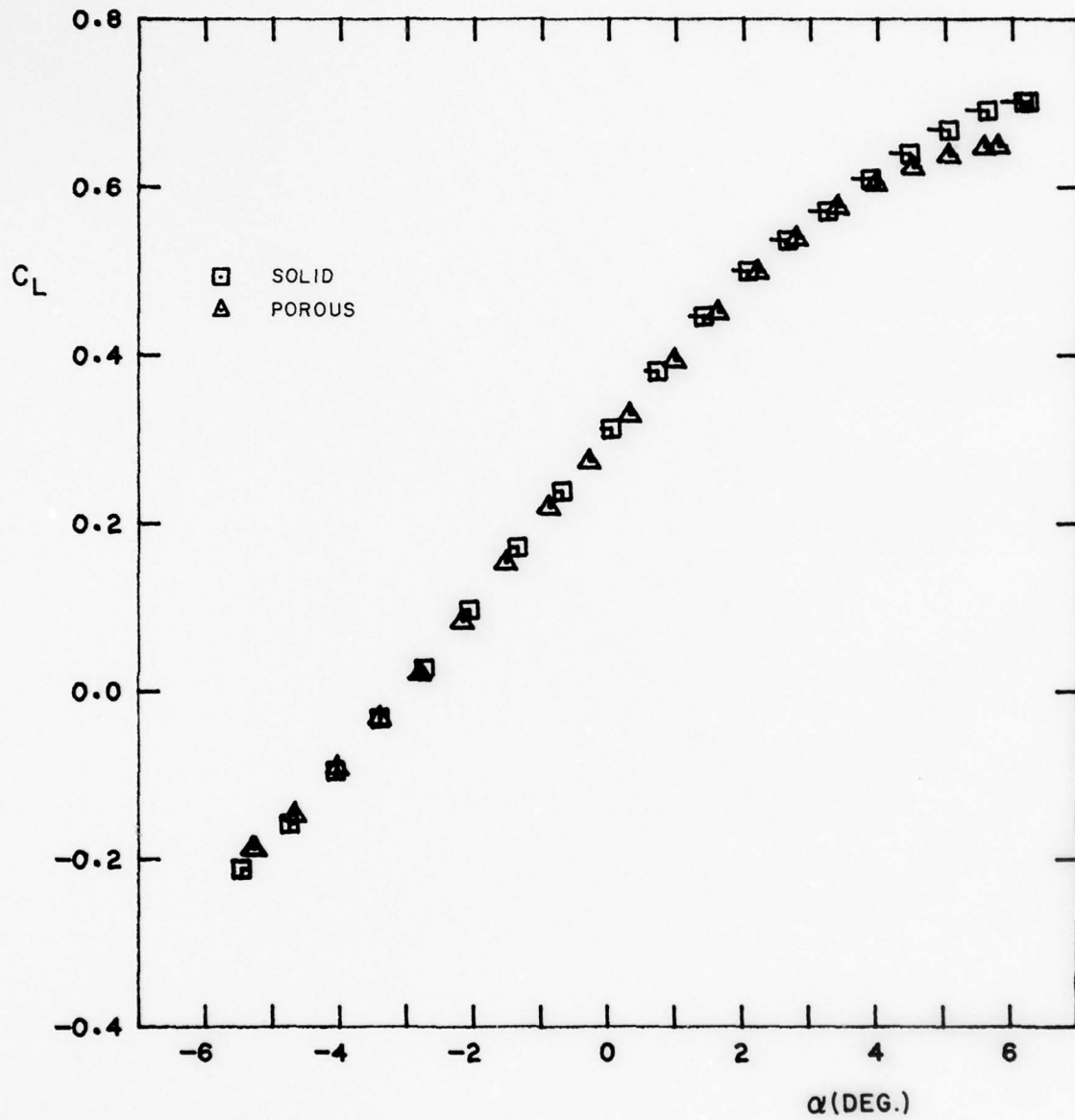
FIG. 19(b): LIFT vs. CORRECTED ANGLE OF ATTACK, MODEL M5, Re = 4.1 × 10⁶, M = 0.705
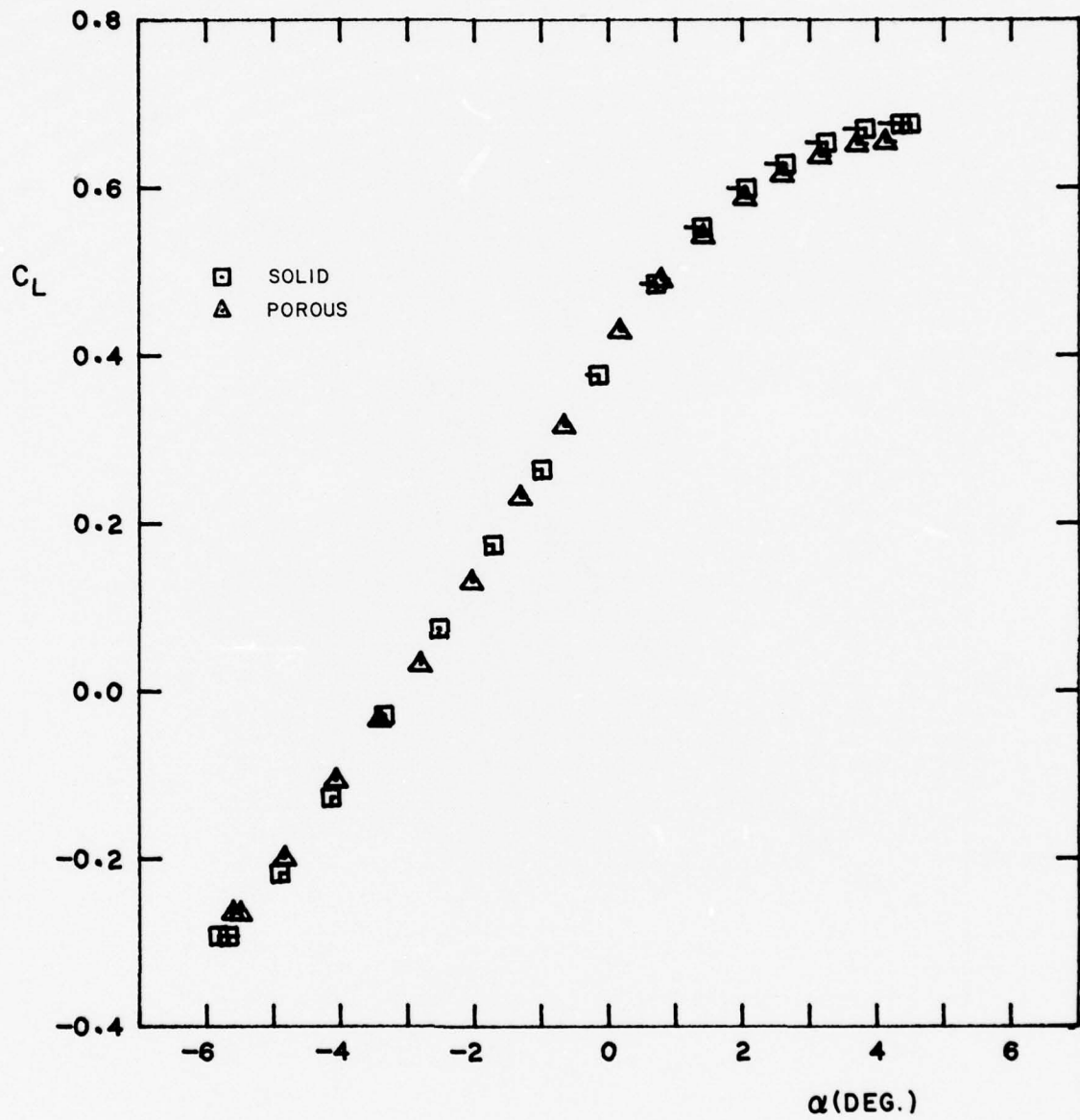
FIG. 19(c): LIFT vs. CORRECTED ANGLE OF ATTACK, MODEL M5, Re = 4.1 $\times$ 10^6, M = 0.840
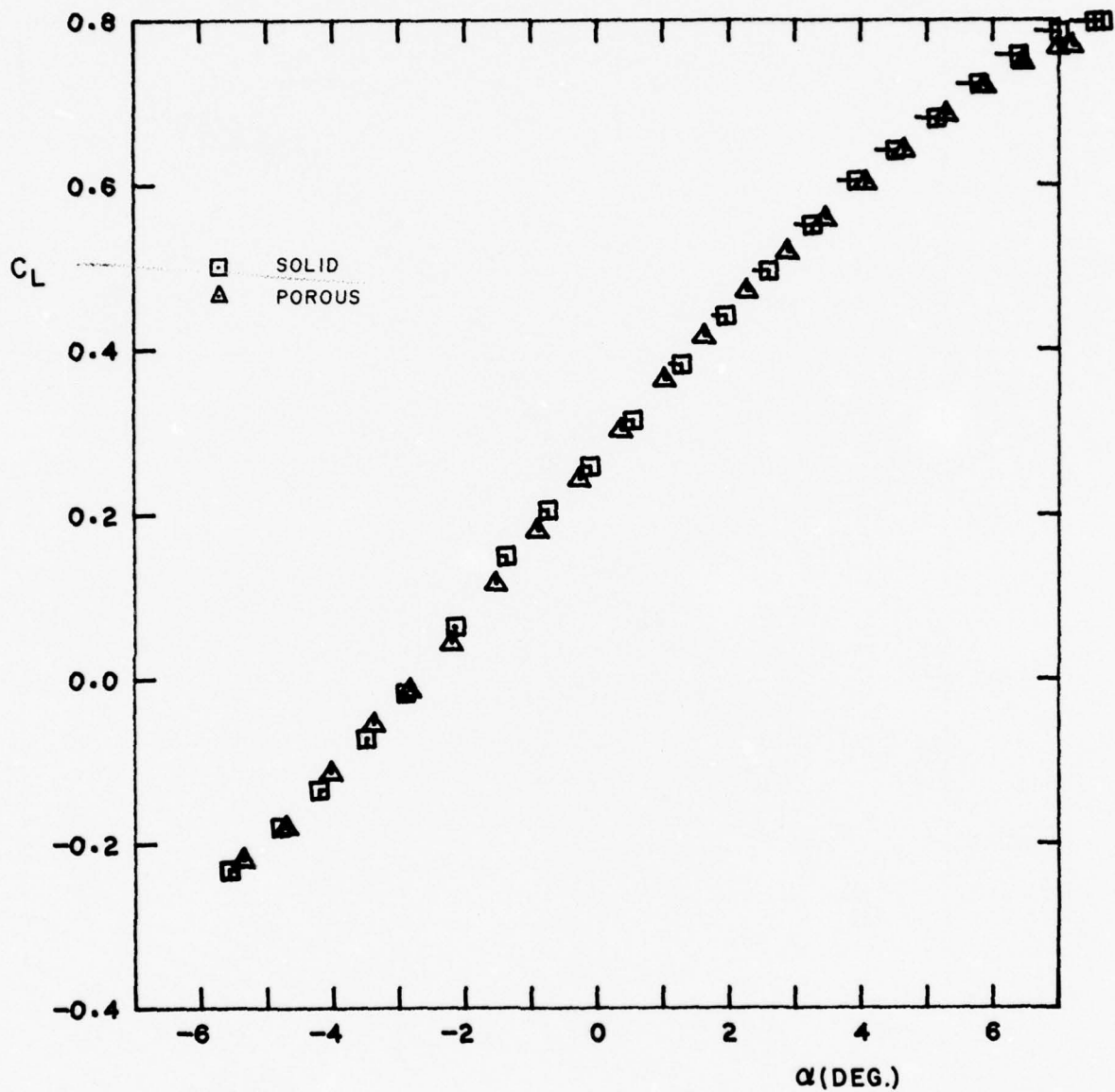
FIG. 19(d): LIFT vs. CORRECTED ANGLE OF ATTACK, MODEL M5, Re = 5.6 $\times$ 10^6, M = 0.505
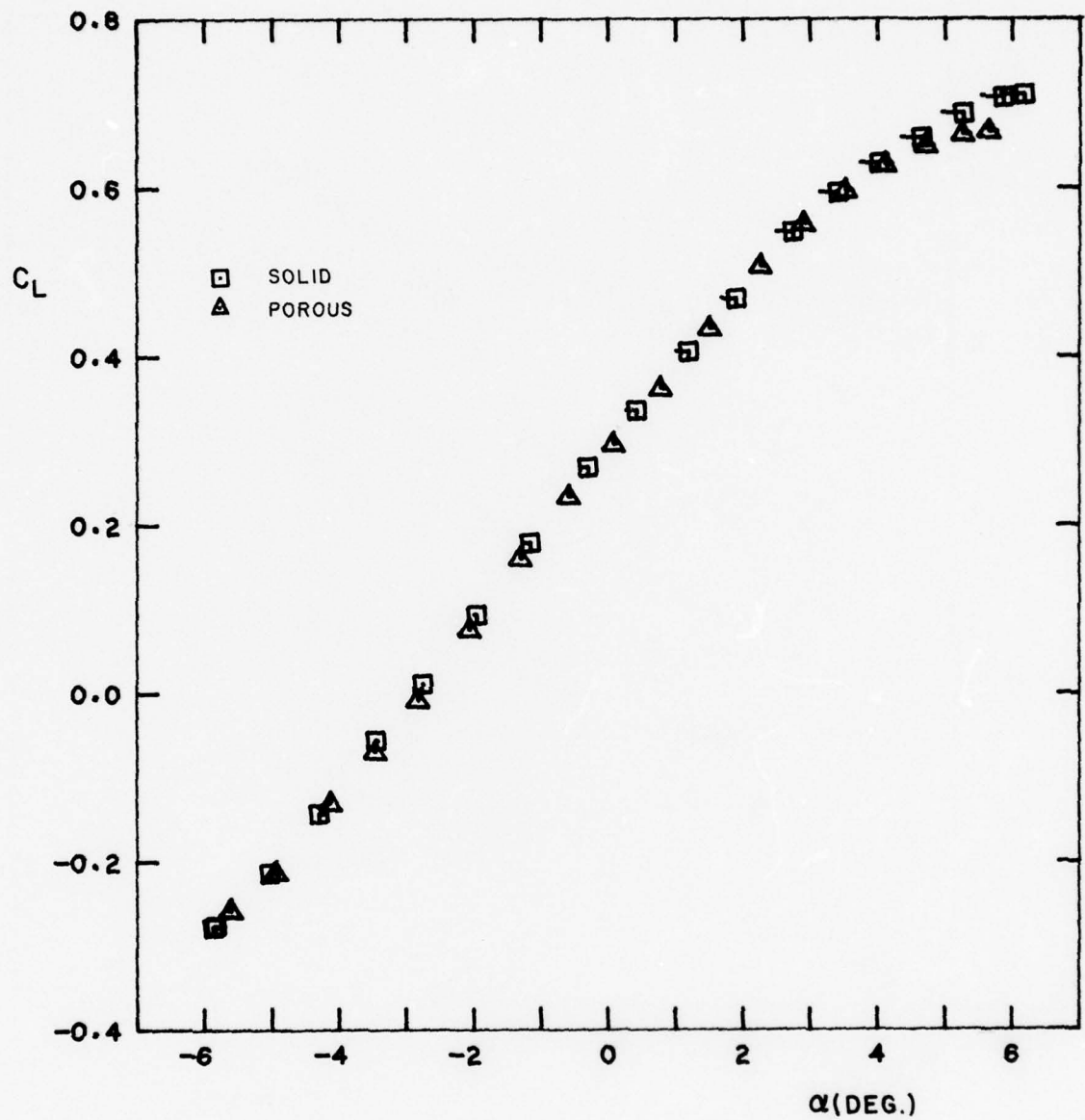
FIG. 19(e): LIFT vs. CORRECTED ANGLE OF ATTACK, MODEL M5, Re = 5.6 $\times$ 10^6, M = 0.702
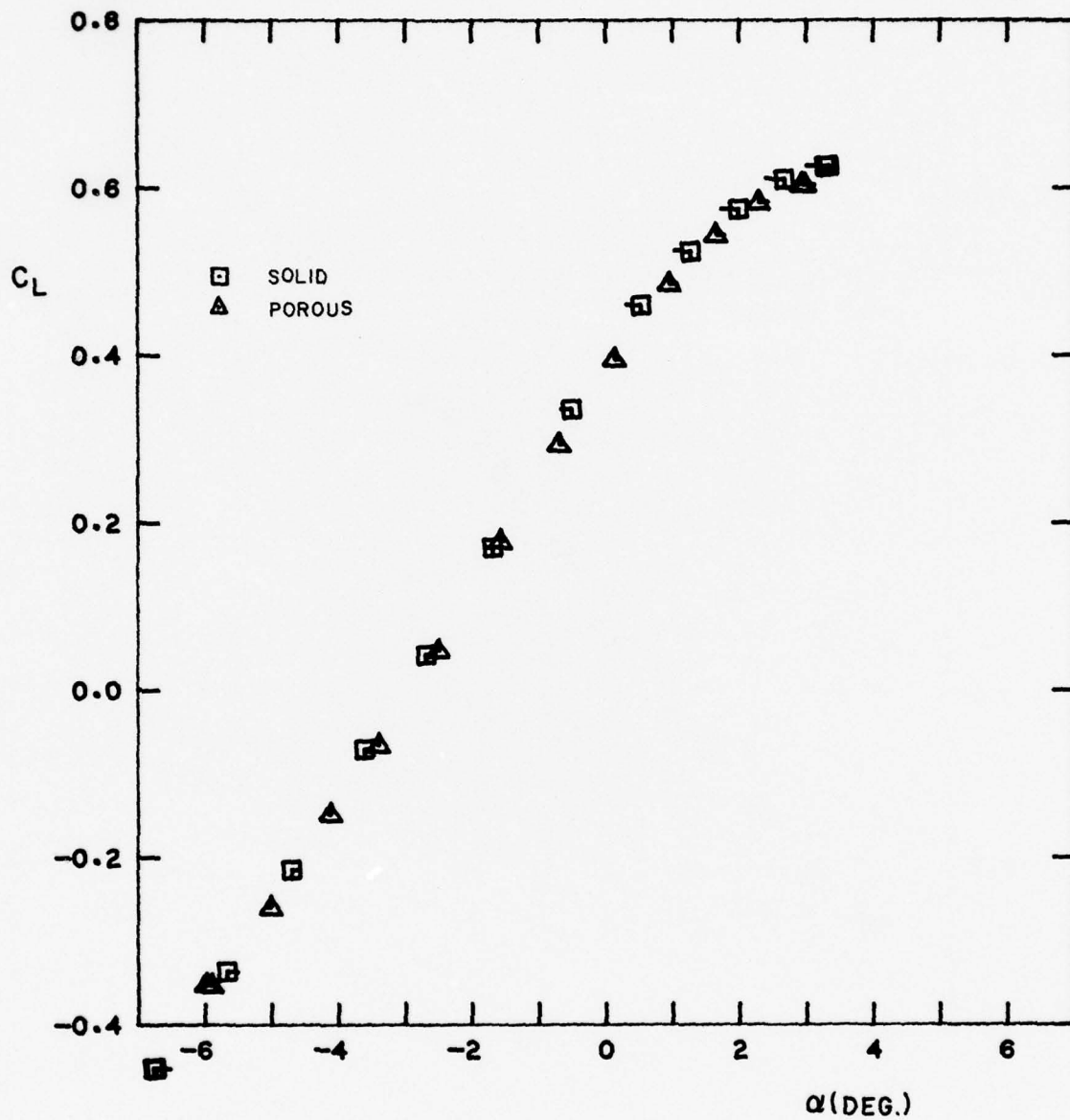
FIG. 19(f): LIFT vs. CORRECTED ANGLE OF ATTACK, MODEL M5, Re = 5.6 $\times$ 10^6, M = 0.842
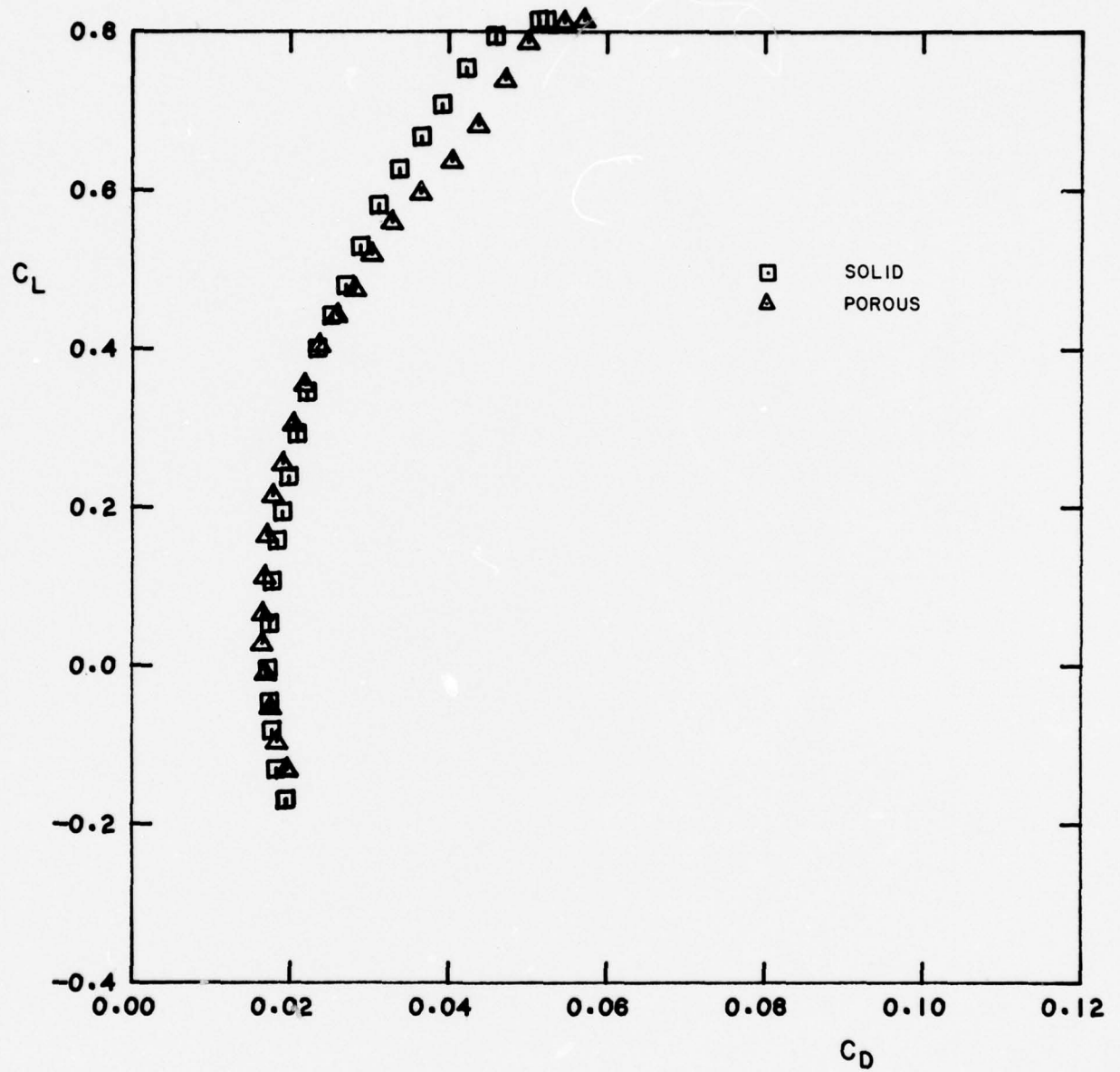
FIG. 20: LIFT vs. DRAG, MODEL M5, Re = 4.1 × 10⁶, M = 0.254
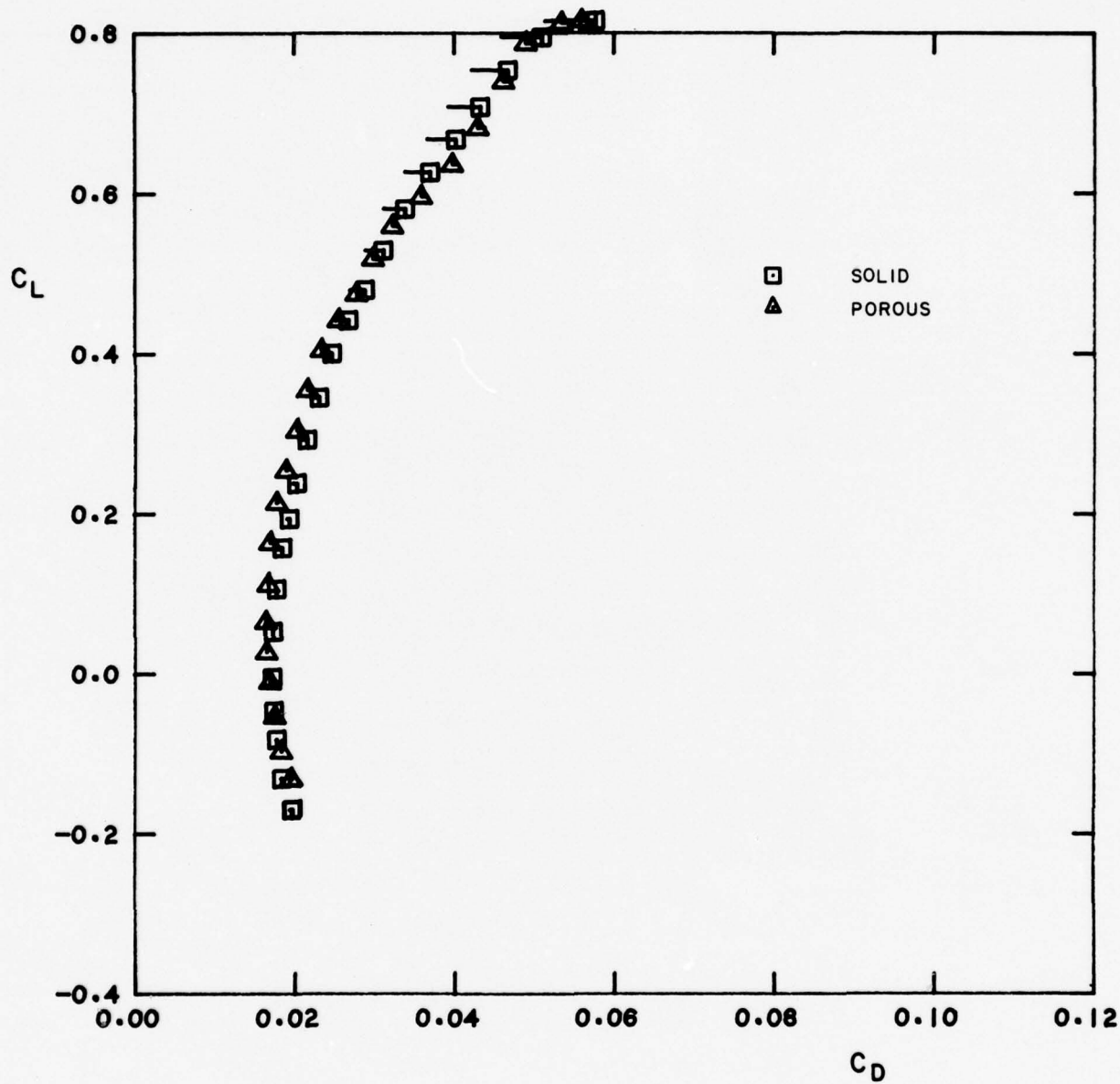
FIG. 21(a): LIFT vs. CORRECTED DRAG, MODEL M5, Re = 4.1 × 10^6, M = 0.254
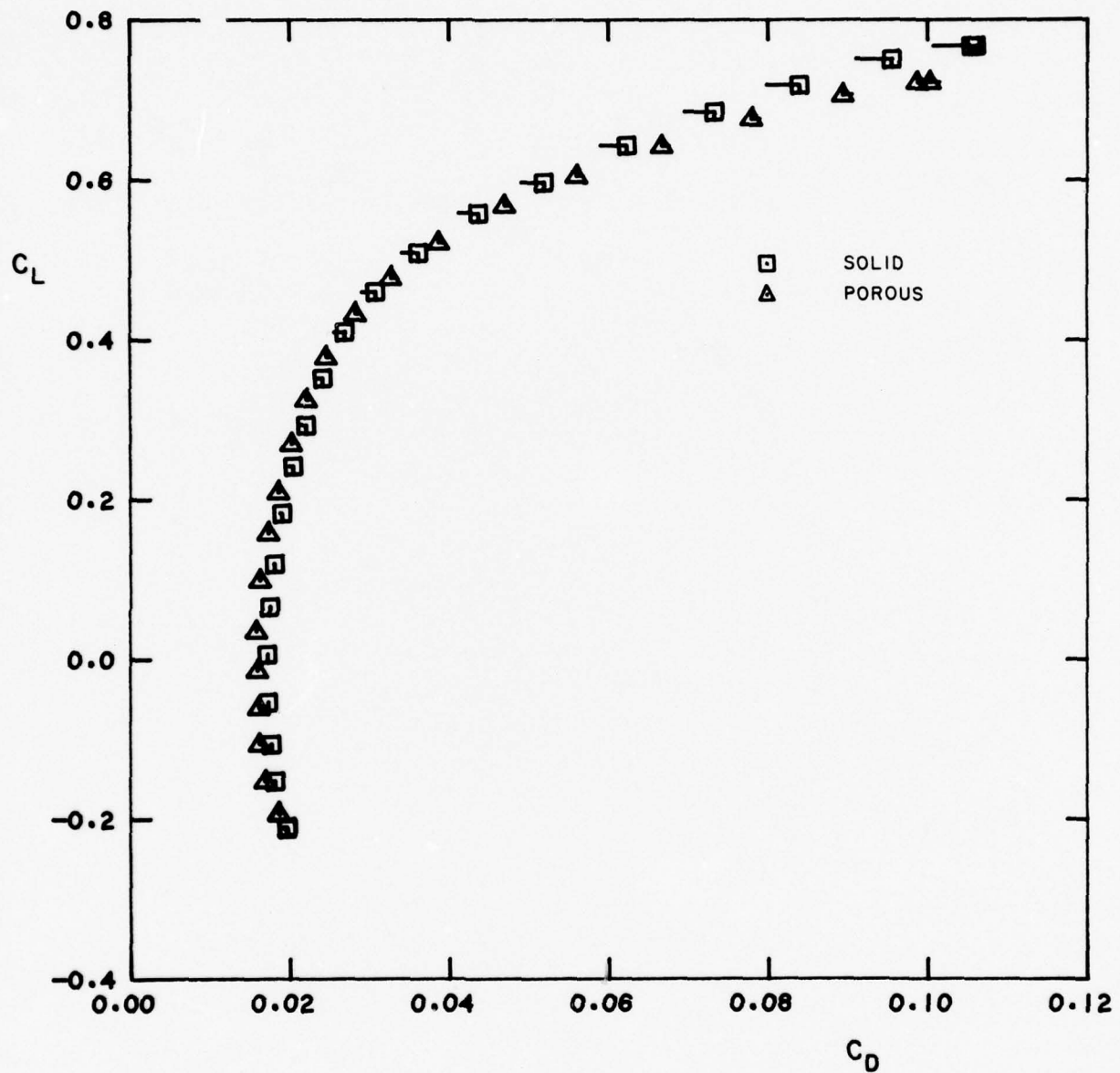
FIG. 21(b): LIFT vs. CORRECTED DRAG, MODEL M5, Re = 4.1 $\times$ 10^6, M = 0.505
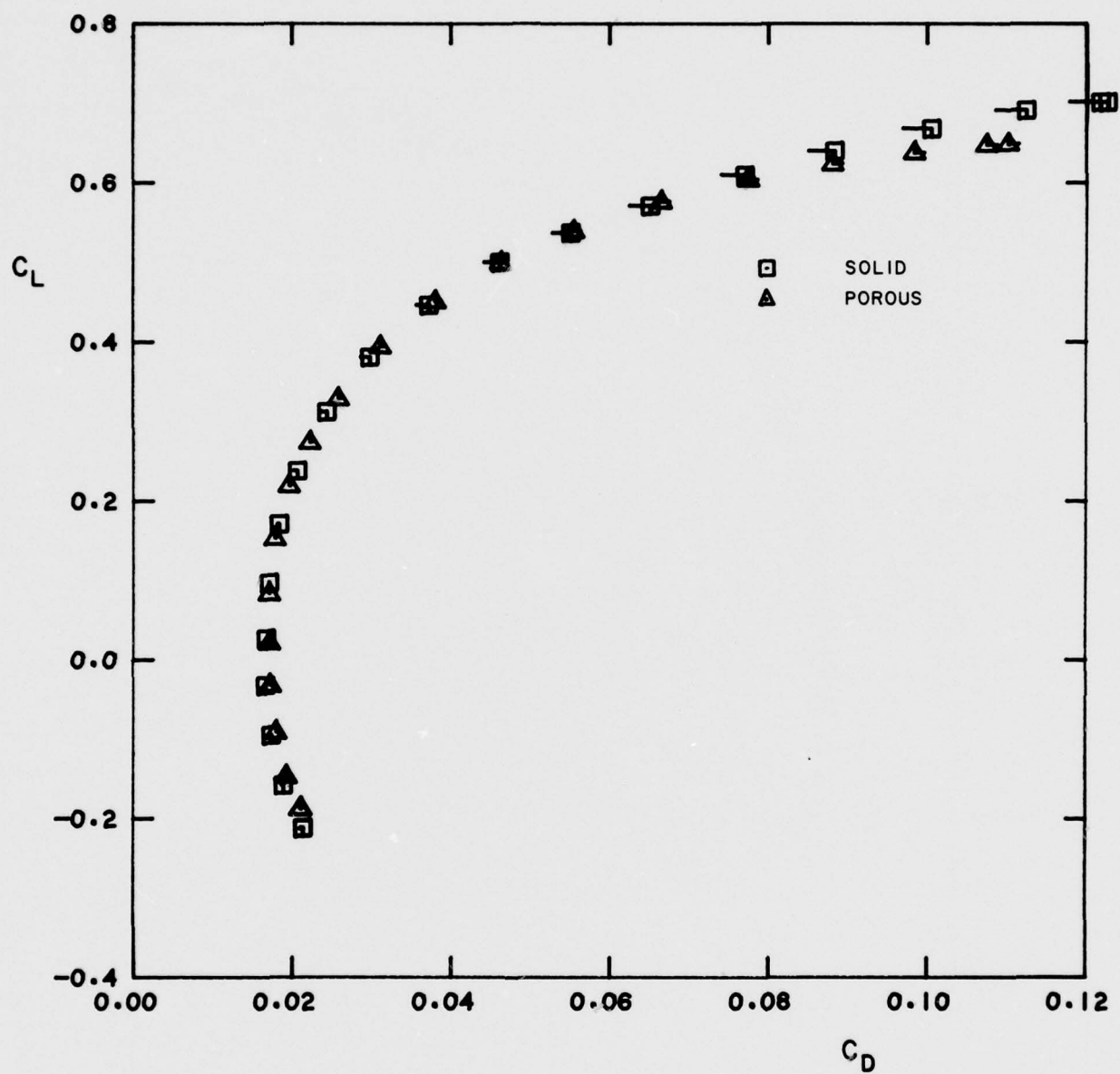
FIG. 21(c): LIFT vs. CORRECTED DRAG, MODEL M5, Re = 4.1 X 10⁶, M = 0.705
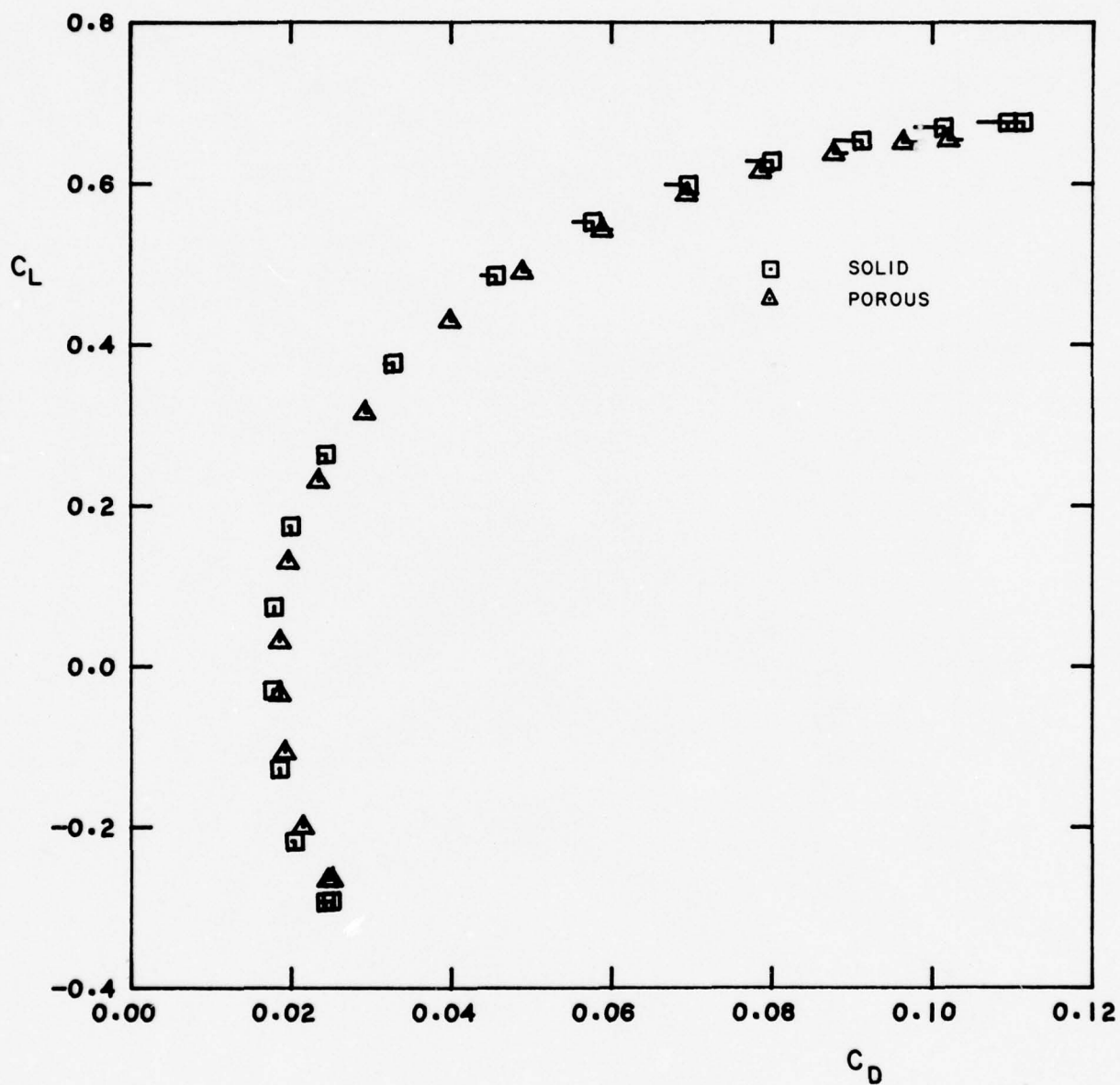
FIG. 21(d): LIFT vs. CORRECTED DRAG, MODEL M5, Re = 4.1 $\times$ 10^6, M = 0.840
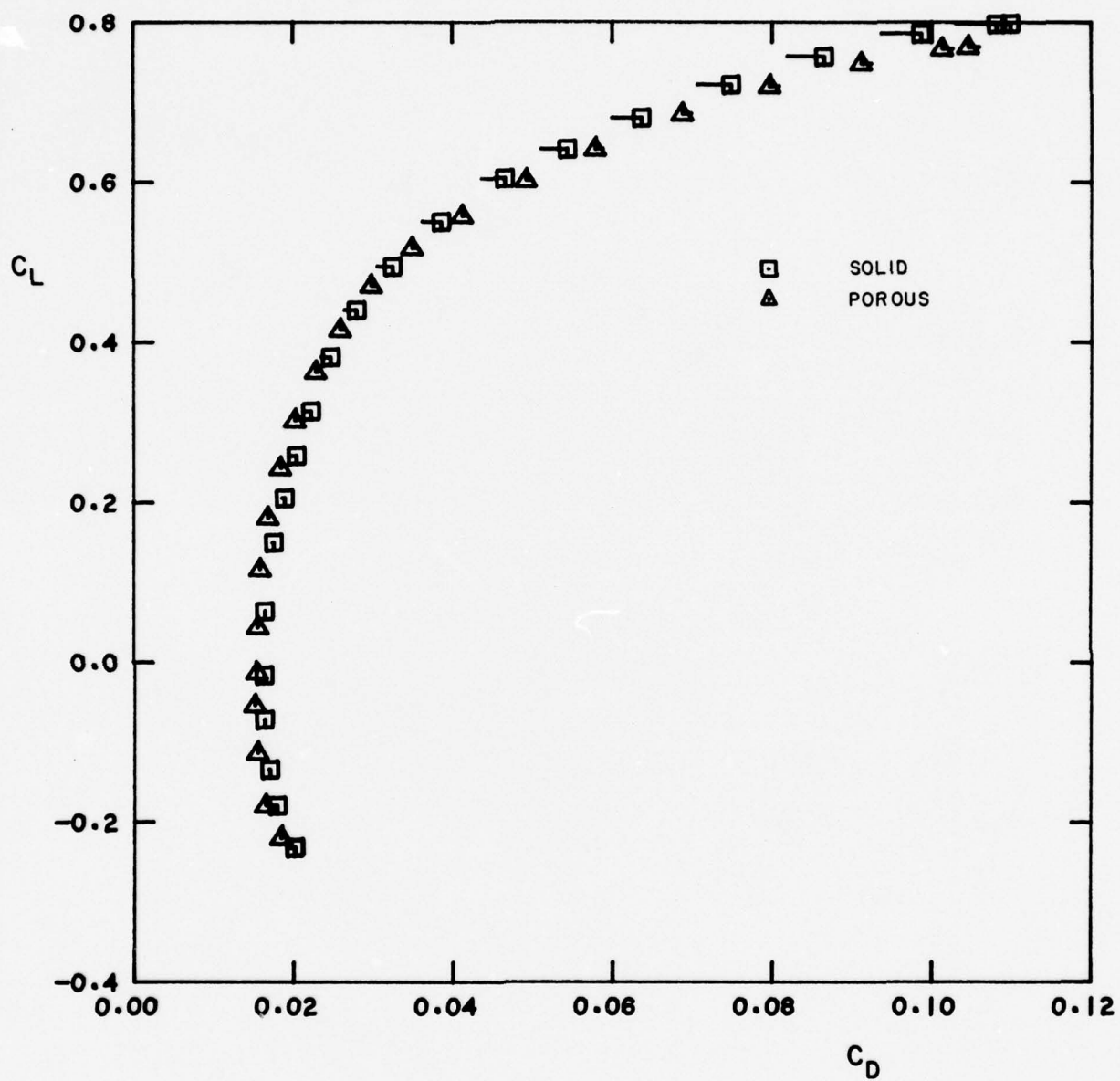
FIG. 21(e): LIFT vs. CORRECTED DRAG, MODEL M5, Re = 5.6 × 10^6, M = 0.505
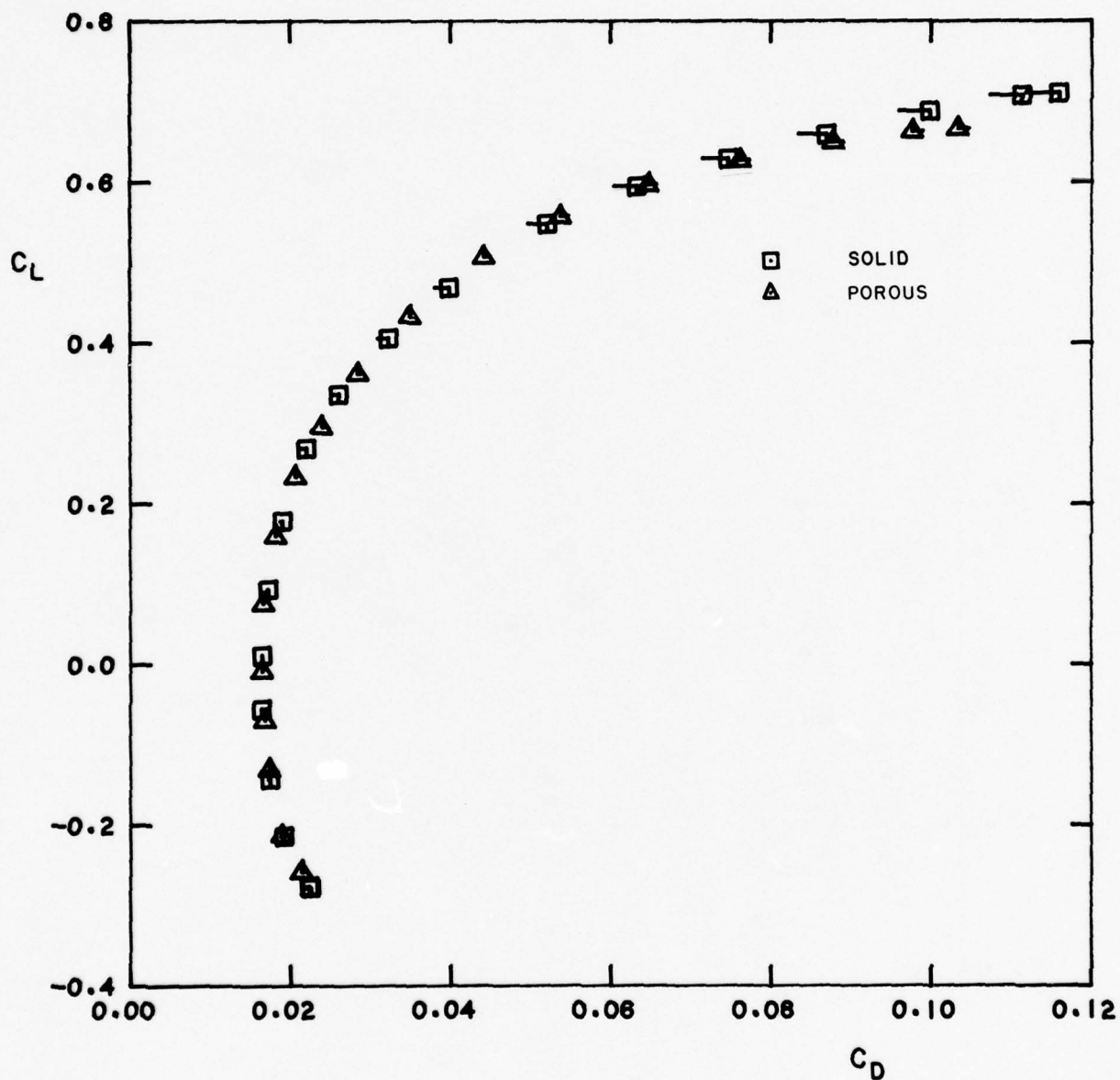
FIG. 21(f): LIFT vs. CORRECTED DRAG, MODEL M5, Re = 5.6 × 10⁶, M = 0.702
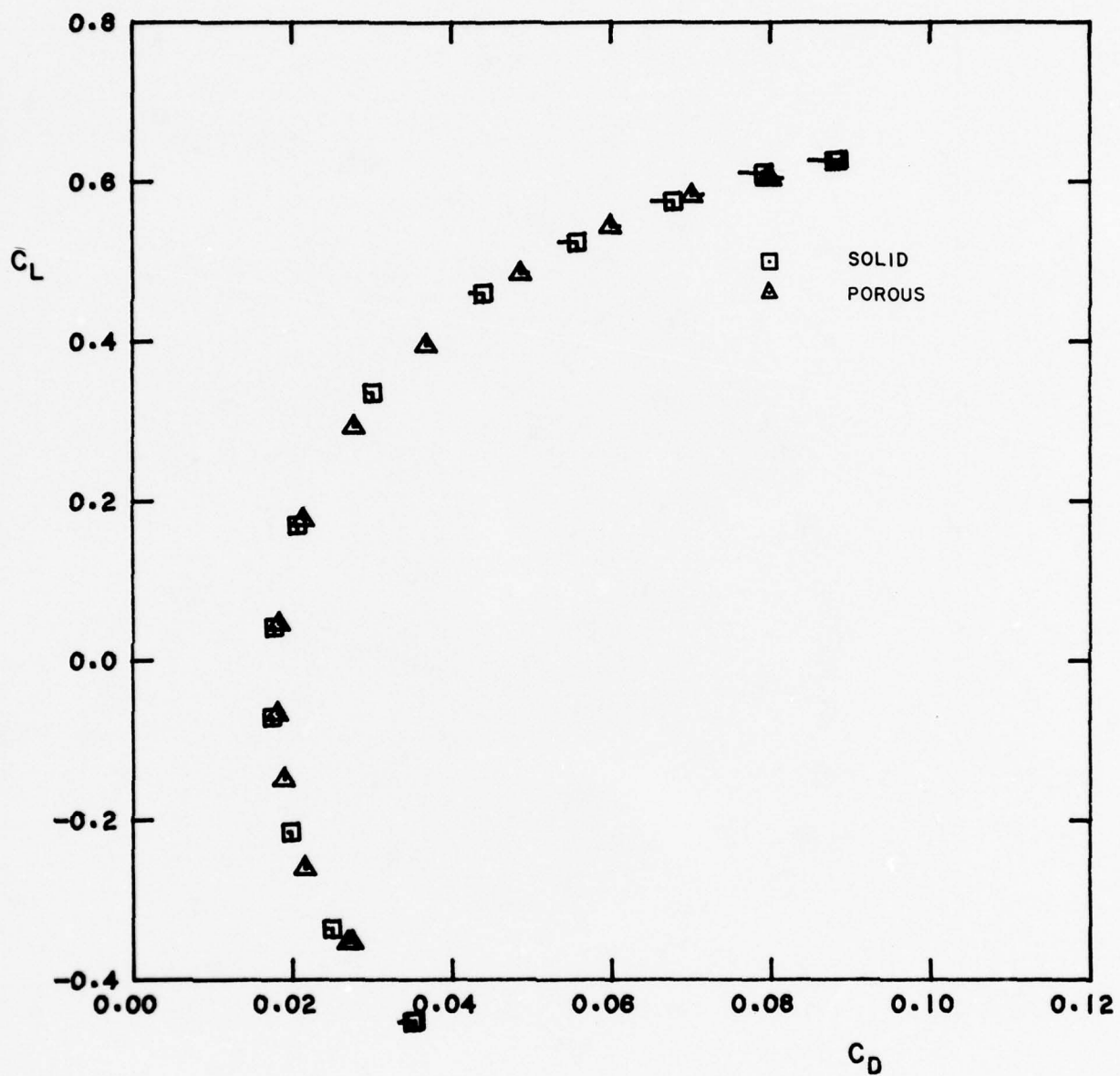
FIG. 21(g): LIFT vs. CORRECTED DRAG, MODEL M5, Re = 5.6 $\times$ 10^6, M = 0.842
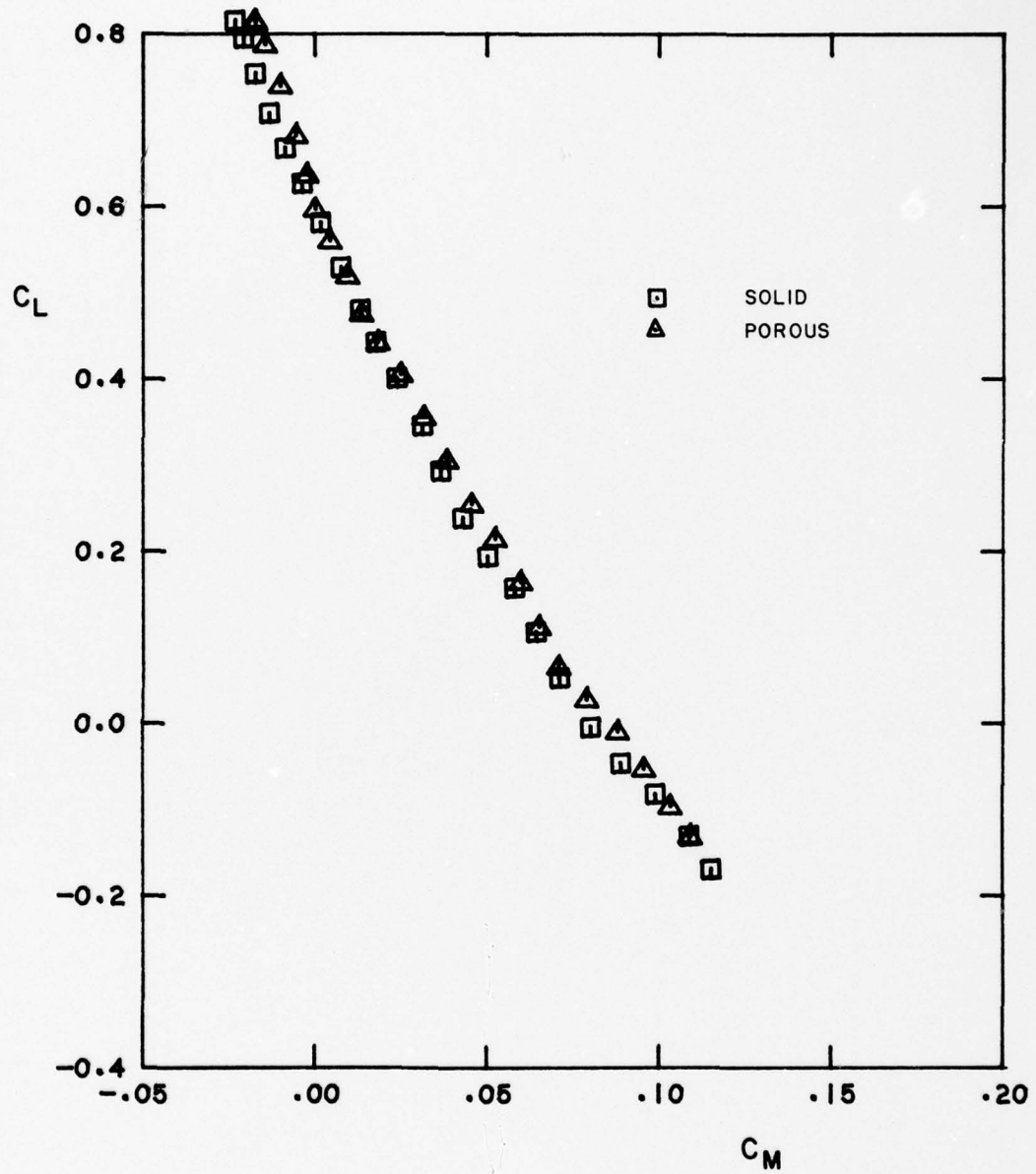
FIG. 22(a): LIFT vs. PITCHING MOMENT, MODEL M5, Re = 4.1 × 10^6, M = 0.254
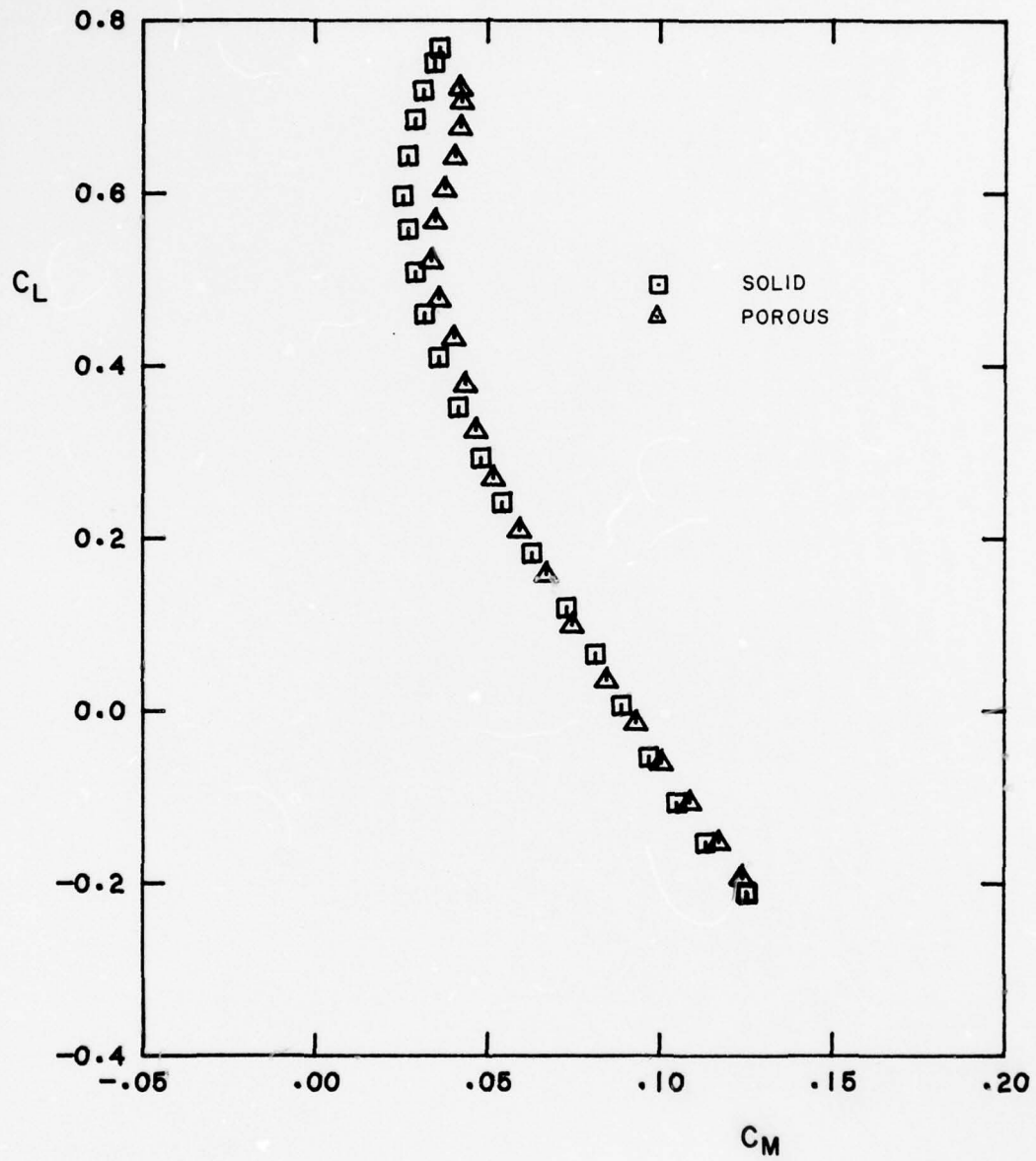
FIG. 22(b): LIFT vs. PITCHING MOMENT, MODEL M5, Re = 4.1 × 10^6, M = 0.505
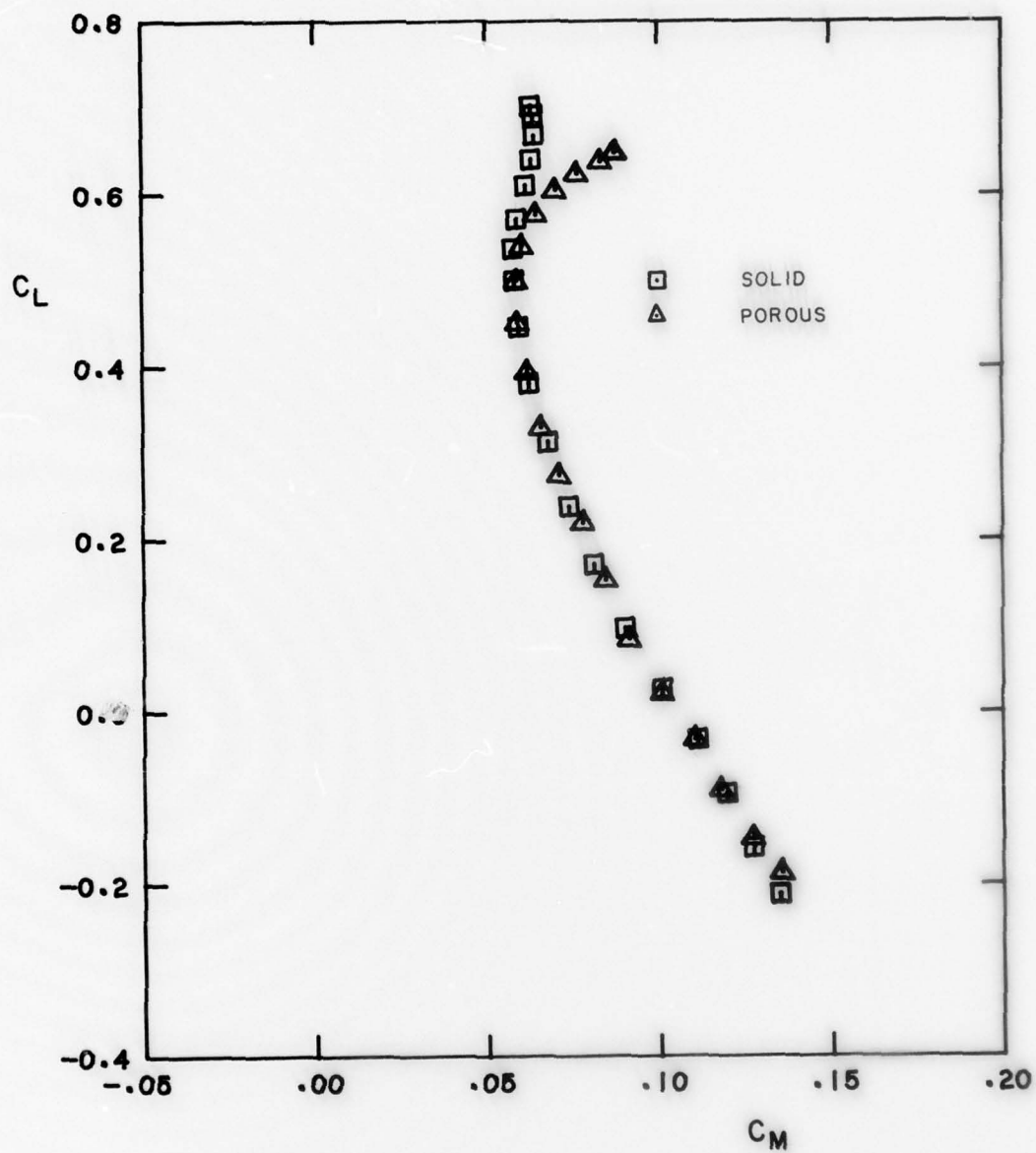
FIG. 22(c): LIFT vs. PITCHING MOMENT, MODEL M5, Re = 4.1 × 10^6, M = 0.705
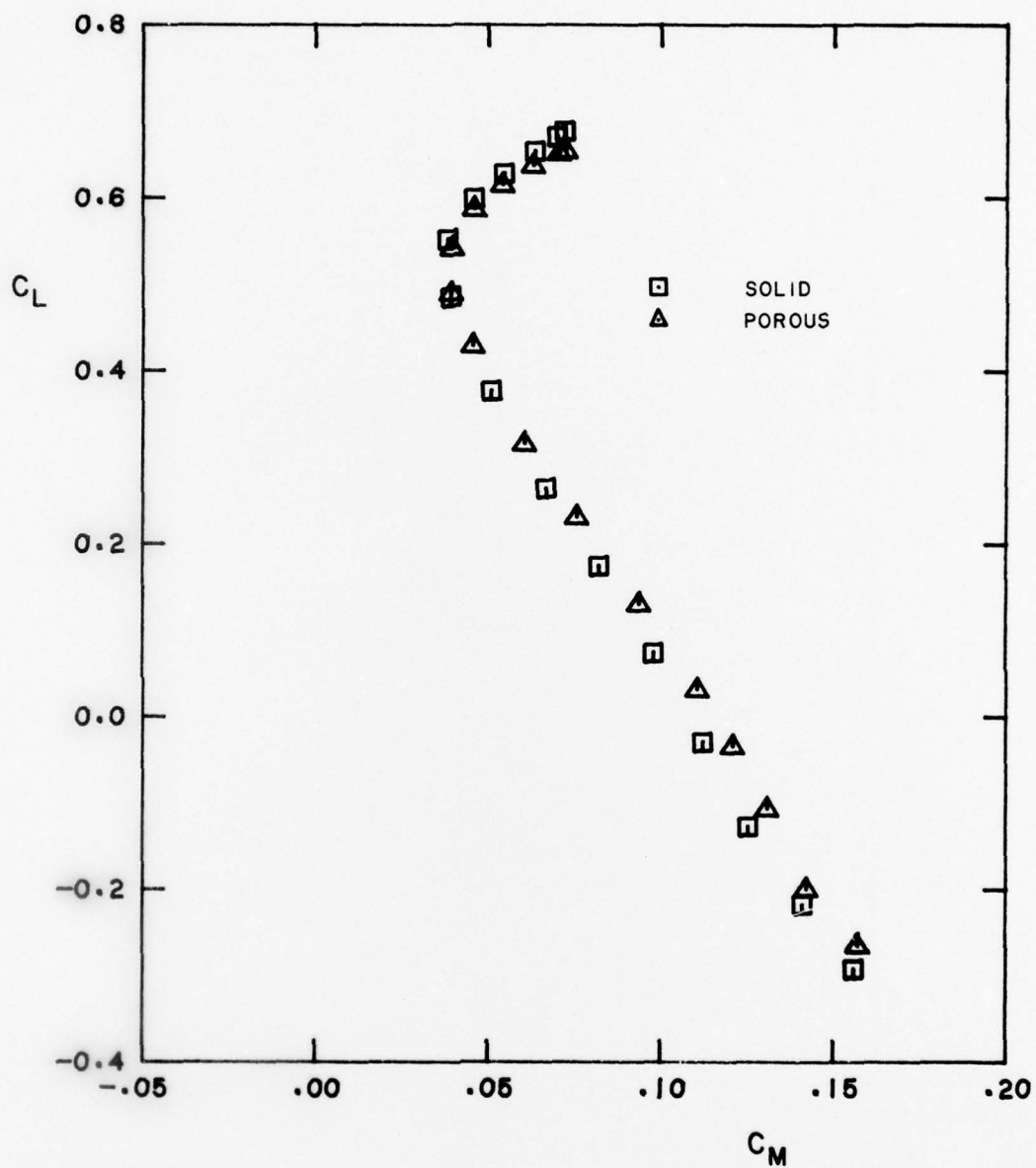
FIG. 22(d): LIFT vs. PITCHING MOMENT, MODEL M5, Re = 4.1 $\times$ 10^6, M = 0.840
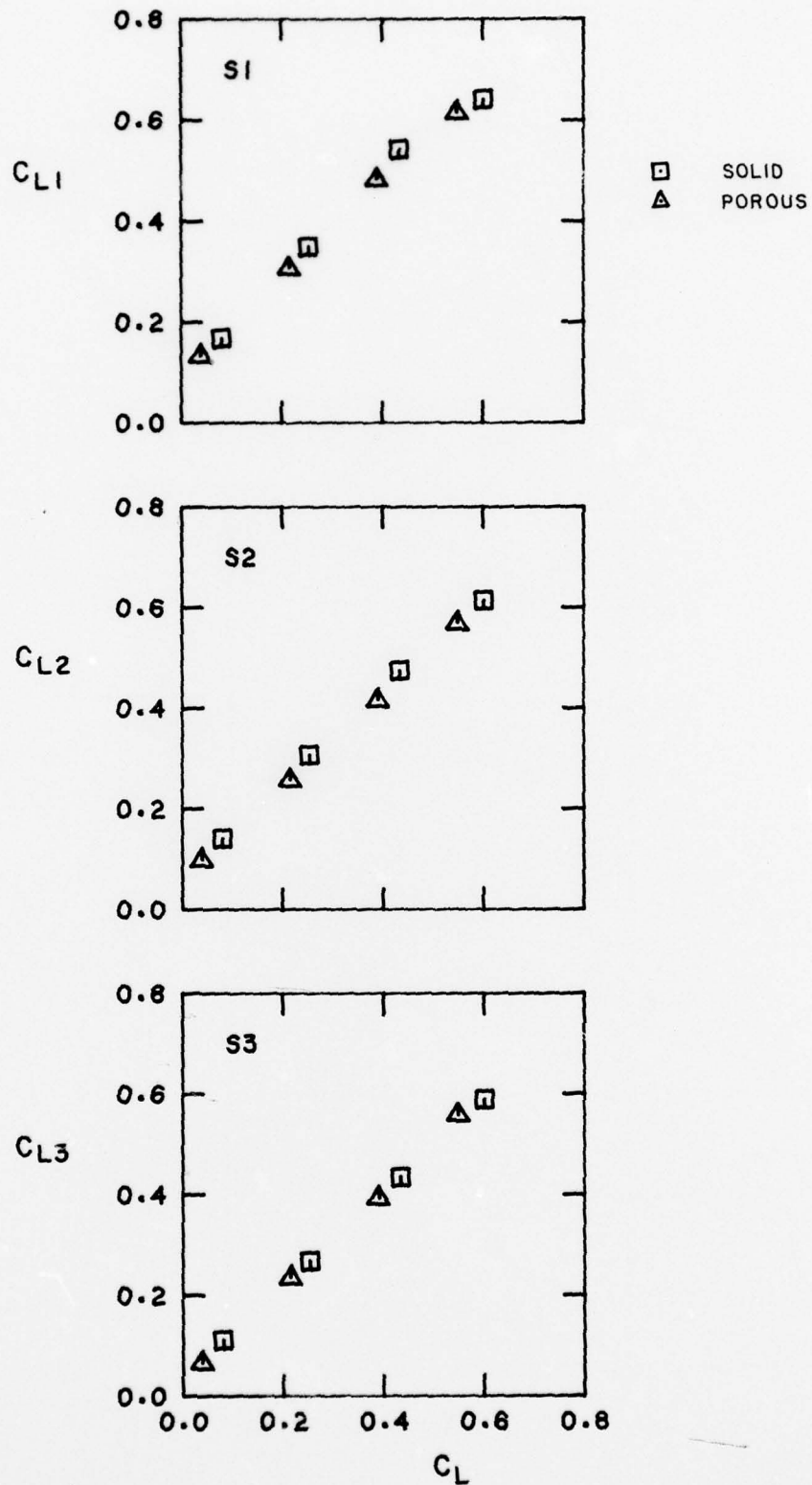
FIG. 23(a): SECTION LIFT COEFFICIENTS vs. MODEL LIFT COEFFICIENT, MODEL M5, Re = 4.1 × 10⁶, M = 0.504
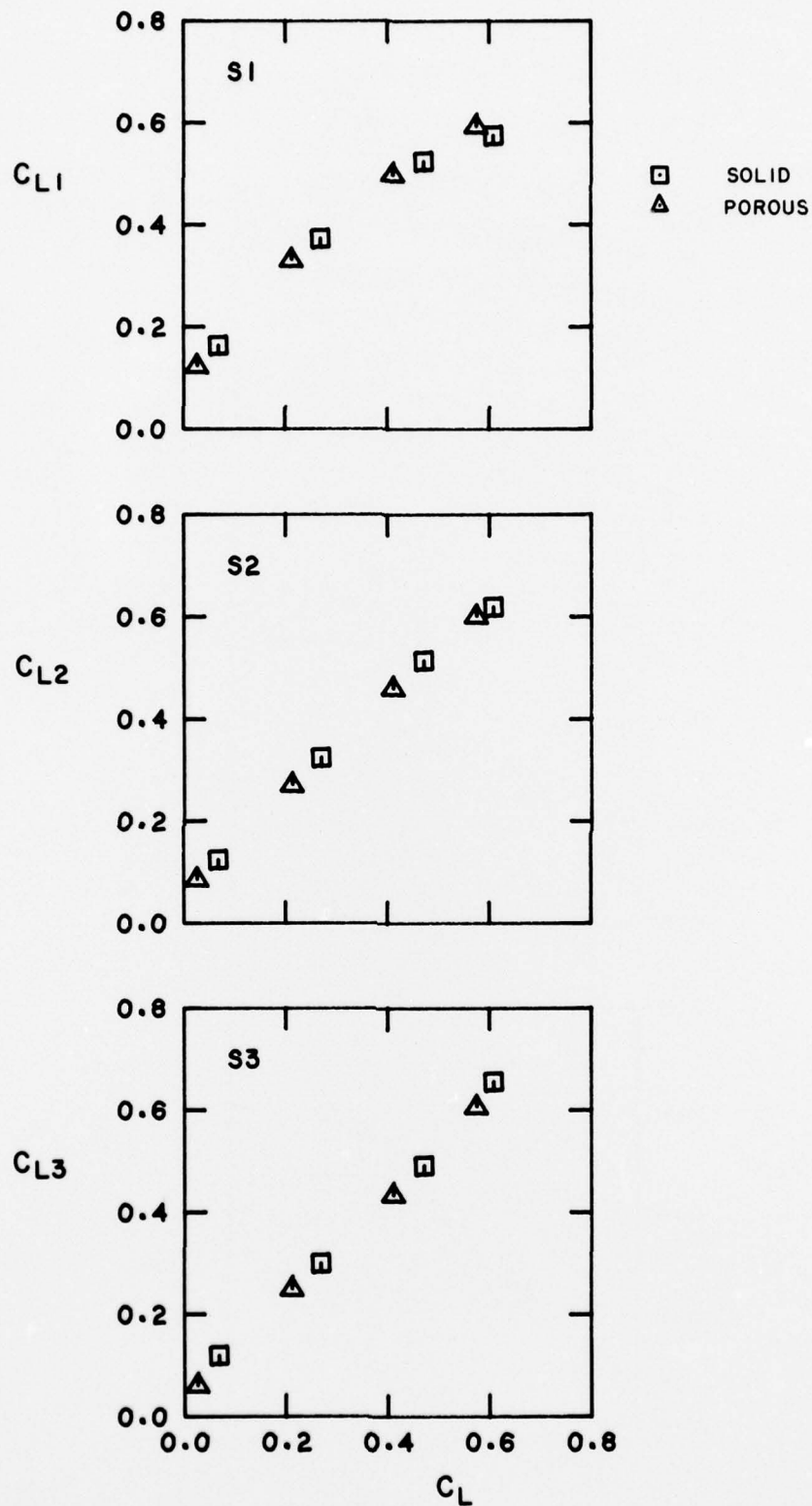
FIG. 23(b): SECTION LIFT COEFFICIENTS vs. MODEL LIFT COEFFICIENT, MODEL M5, Re = 4.1 × 10⁶, M = 0.705
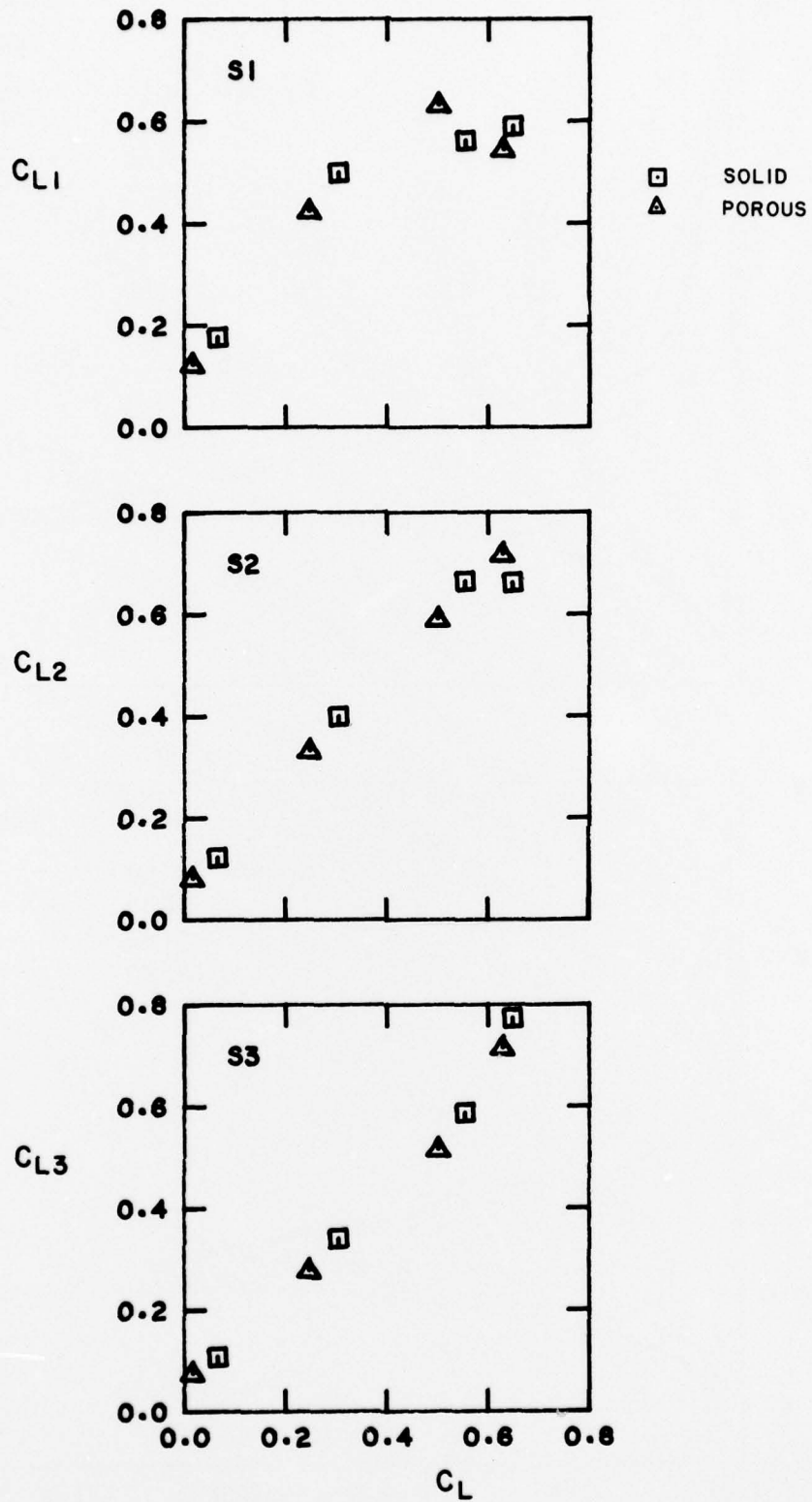
FIG. 23(c): SECTION LIFT COEFFICIENTS vs. MODEL LIFT COEFFICIENT, MODEL M5, Re ≈ 4.1 × 10⁶, M = 0.840
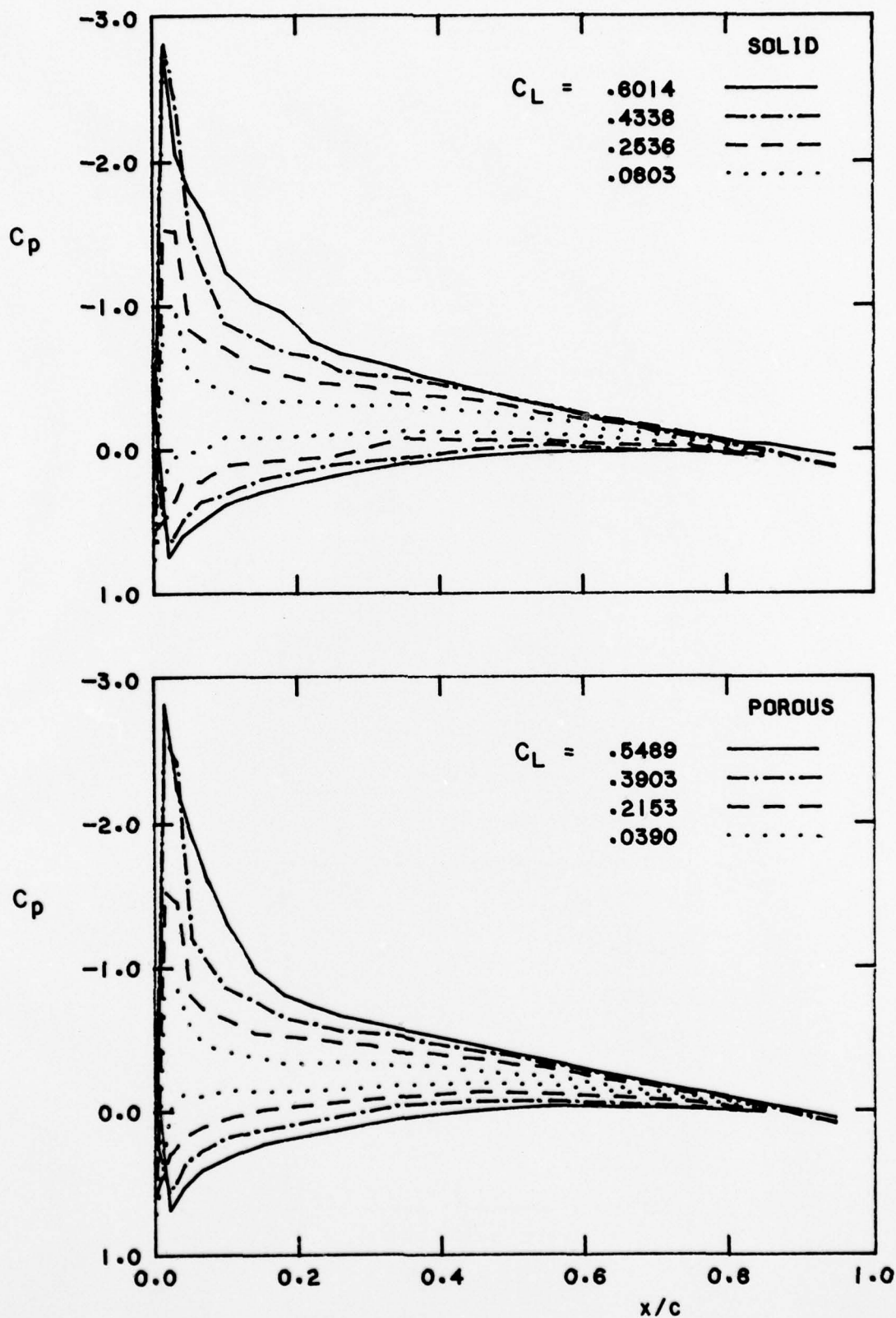
FIG. 24(a): WING SECTION PRESSURE DISTRIBUTIONS, MODEL M5, SECTION S1,
Re = 4.1 × 10⁶, M = 0.504 (C$_p^*$ = – 2.090)
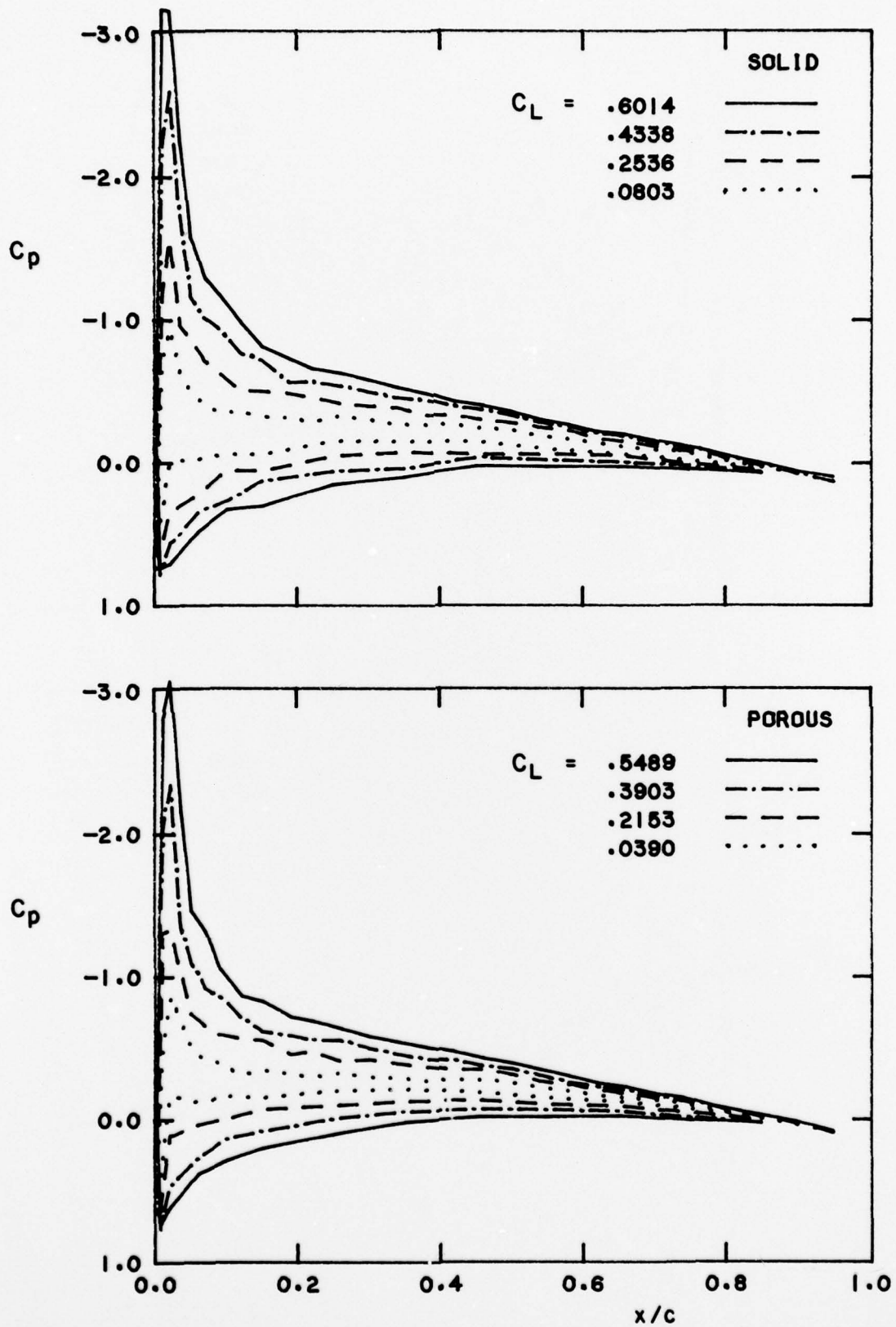
FIG. 24(b): WING SECTION PRESSURE DISTRIBUTIONS, MODEL M5, SECTION S2,
Re = 4.1 × 10⁶, M = 0.504 (C*ₚ = – 2.090)
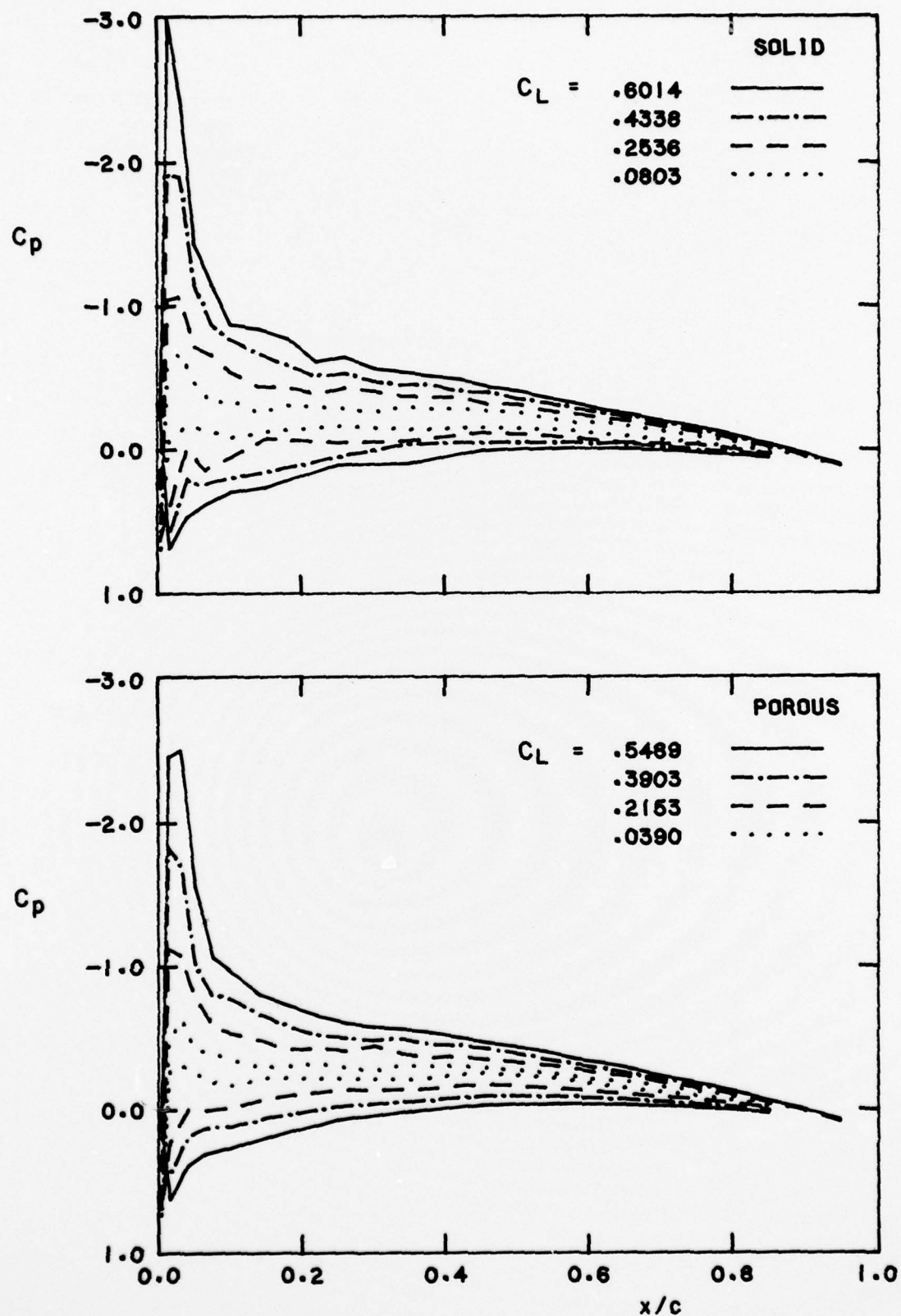
FIG. 24(c): WING SECTION PRESSURE DISTRIBUTIONS, MODEL M5, SECTION S3,
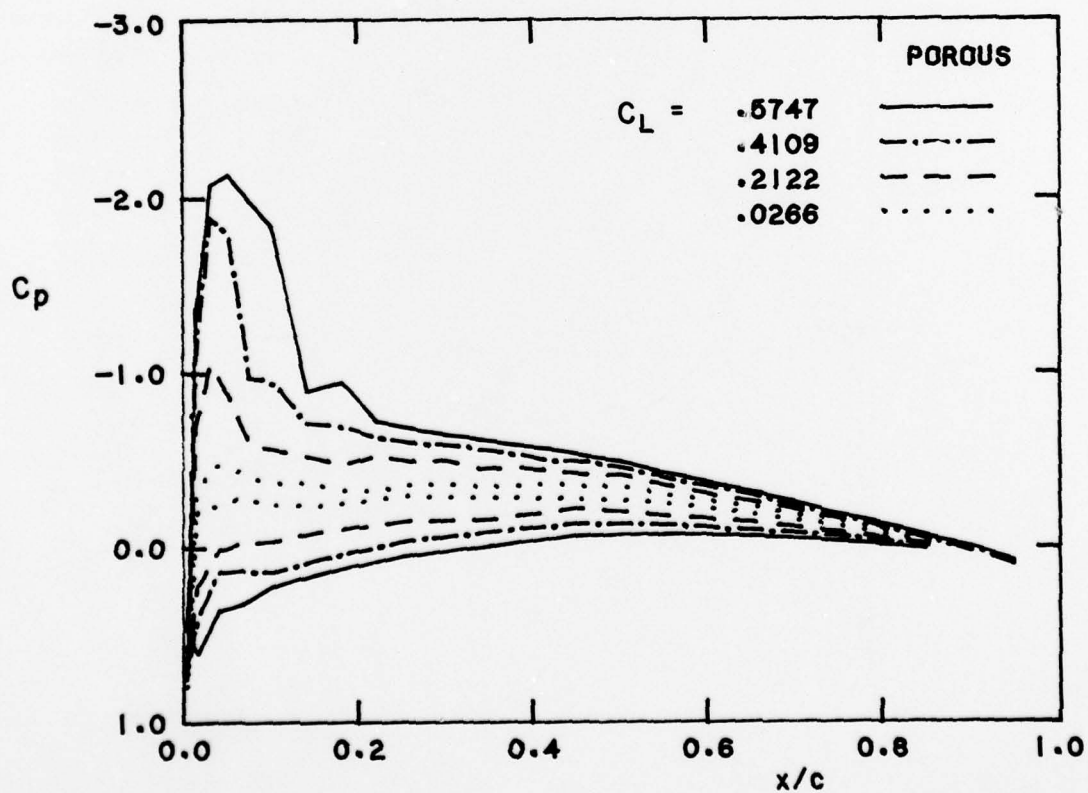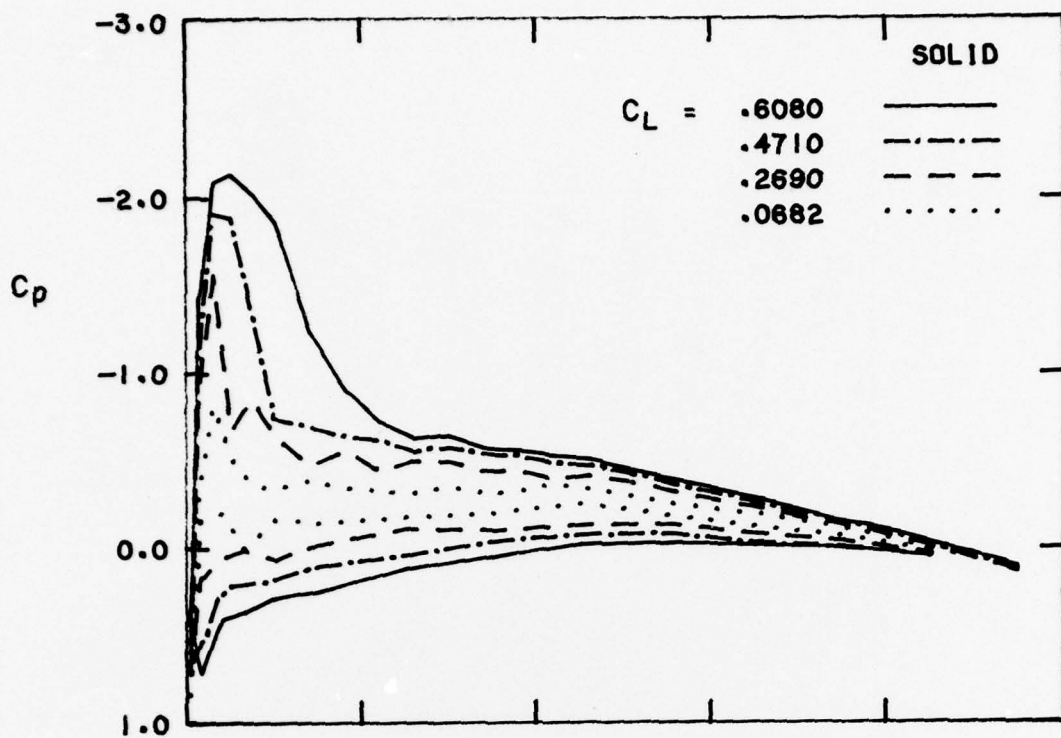$Re = 4.1 \times 10^6$, M = 0.504 ($C_p^* = -2.090$)
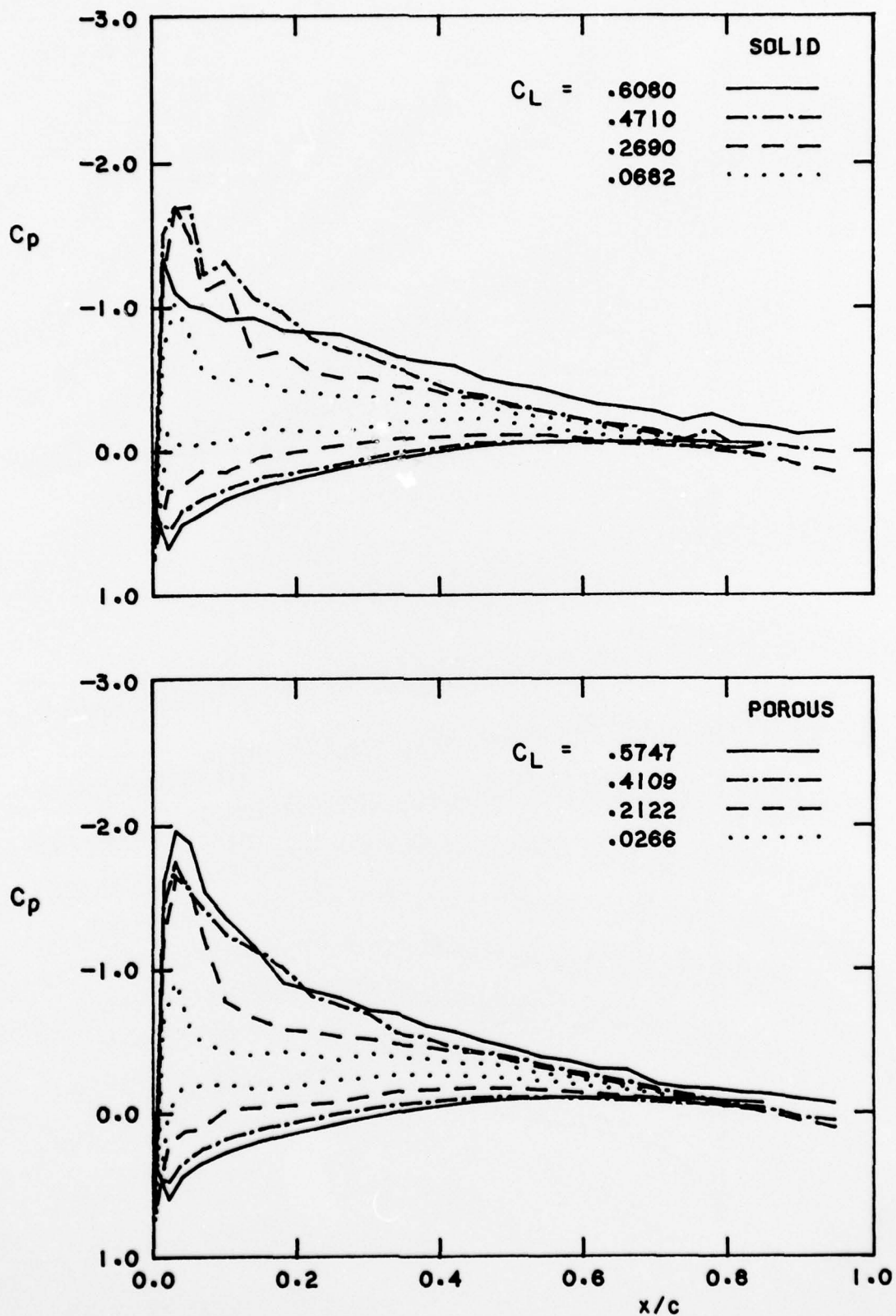
FIG. 25(a): WING SECTION PRESSURE DISTRIBUTIONS, MODEL M5, SECTION S1,
Re = 4.1 × 10⁶, M = 0.705 (C$_p^*$ = – 0.759)
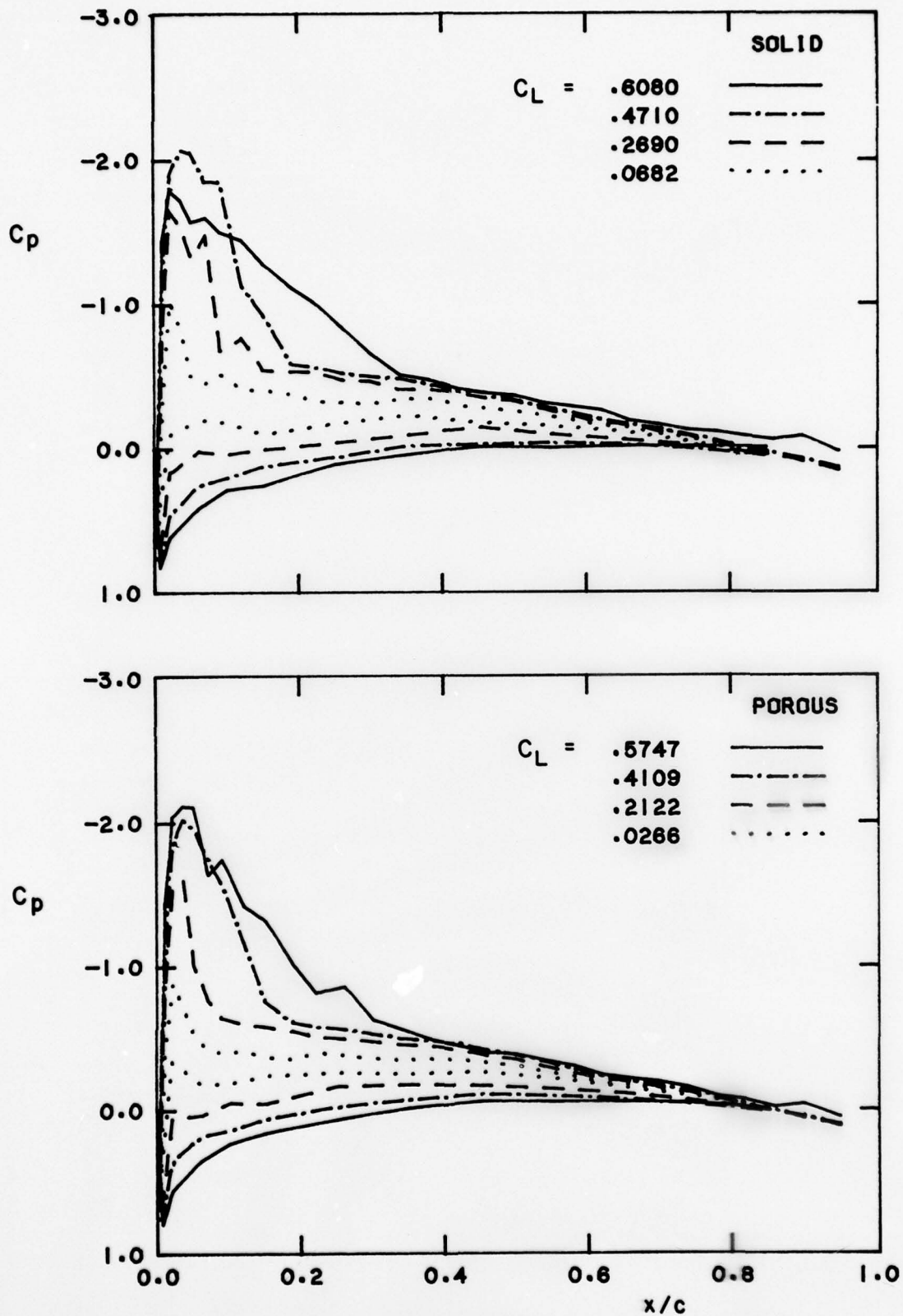
FIG. 25(b): WING SECTION PRESSURE DISTRIBUTIONS, MODEL M5, SECTION S2,
Re = 4.1 × 10^6, M = 0.705 (C$_p^*$ = −0.759)

FIG. 25(c): WING SECTION PRESSURE DISTRIBUTIONS, MODEL M5, SECTION S3, Re = 4.1 $\times$ 10^6, M = 0.705 (C$_p^*$ = $-$0.759)
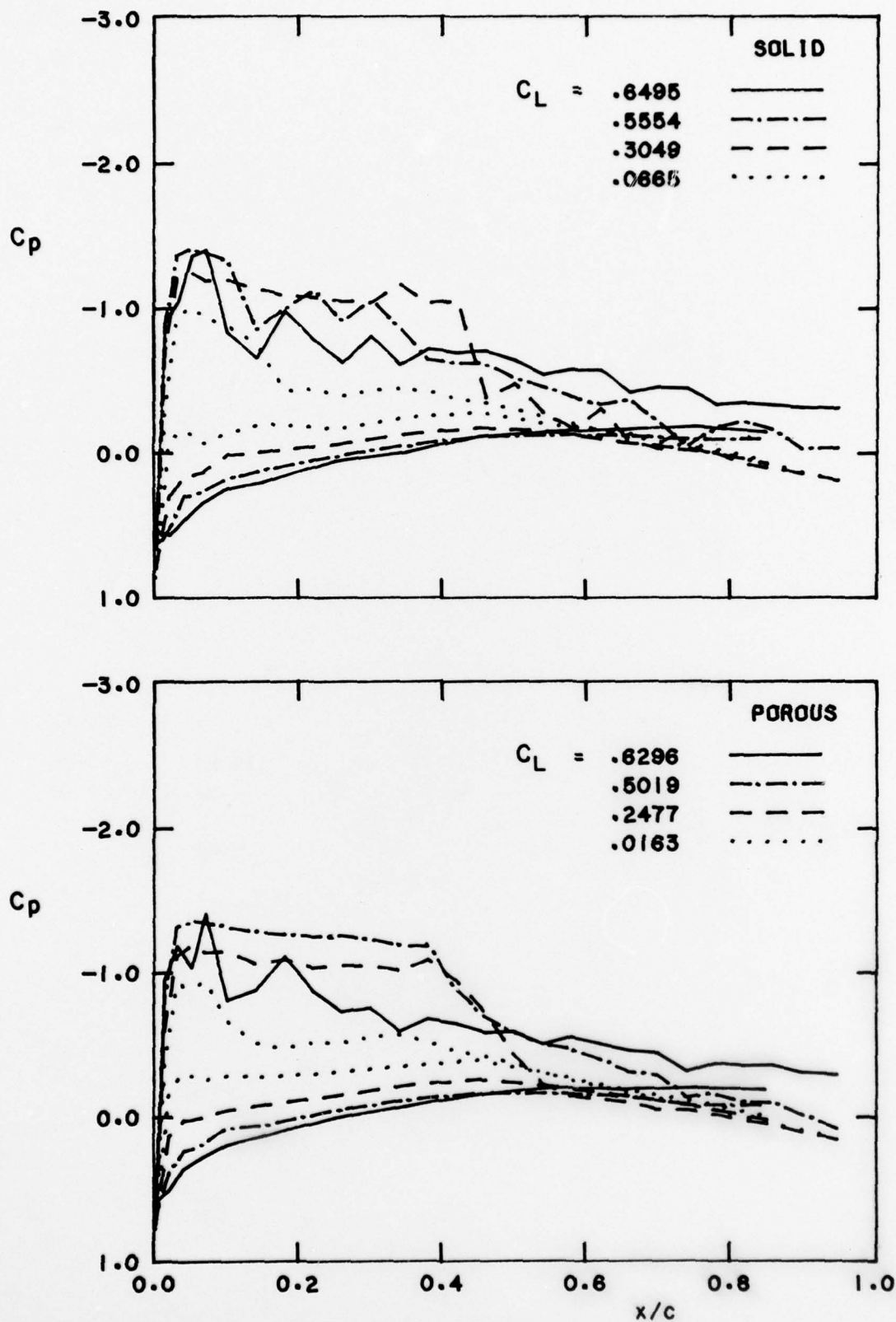
FIG. 26(a): WING SECTION PRESSURE DISTRIBUTIONS, MODEL M5, SECTION S1,
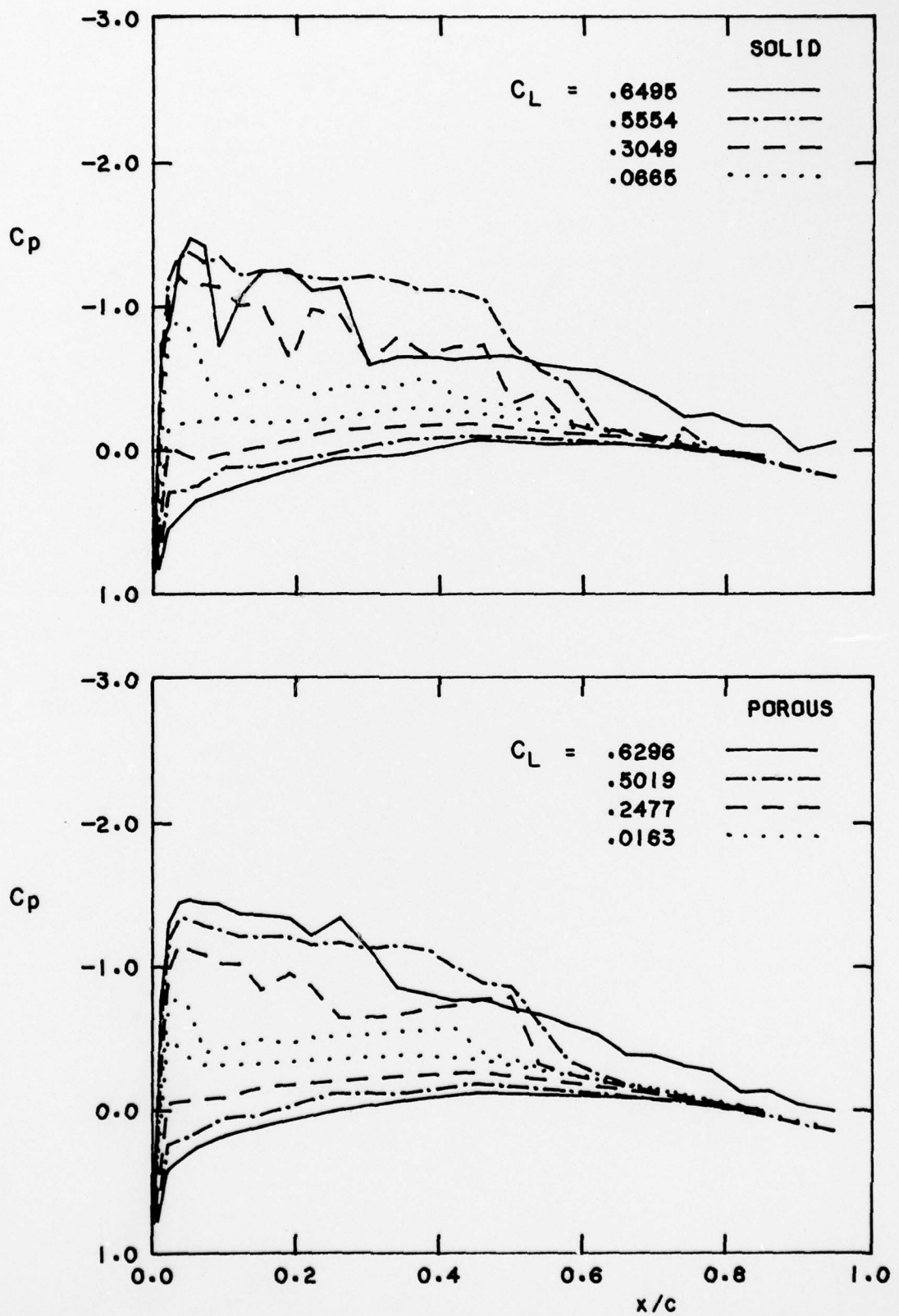Re = 4.1 × 10^6, M = 0.840 (C$_p^*$ = − 0.327)

FIG. 26(b): WING SECTION PRESSURE DISTRIBUTIONS, MODEL M5, SECTION S2,
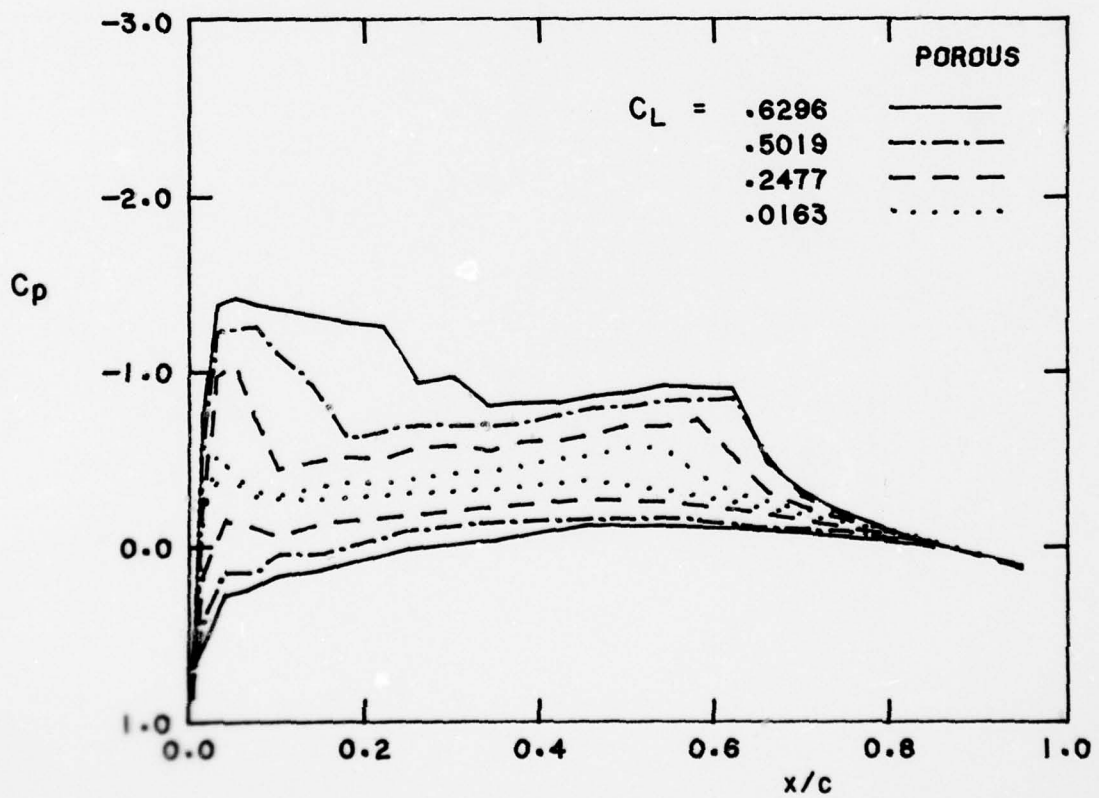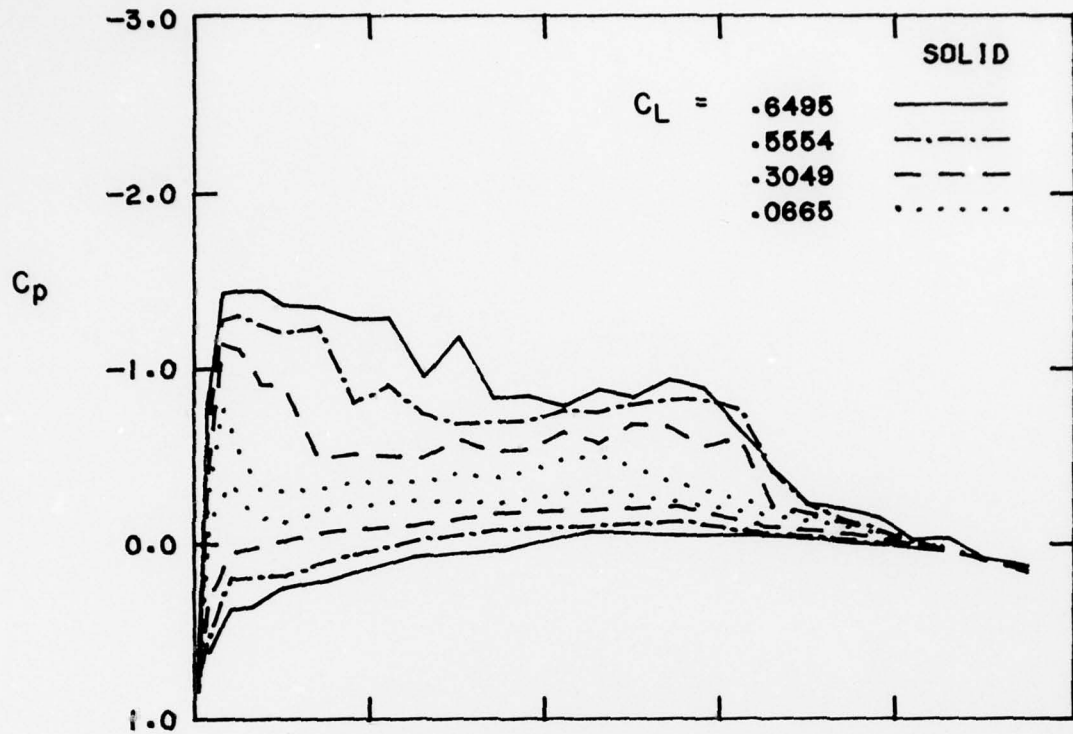Re = 4.1 × 10⁶, M = 0.840 ($C_p^* = -0.327$)

FIG. 26(c): WING SECTION PRESSURE DISTRIBUTIONS, MODEL M5, SECTION S3, $Re = 4.1 \times 10^6$, $M = 0.840$ ($C_p^* = -0.327$)